Ice-Ocean Interactions in North West Greenland

Thomas Millgate

Thesis submitted to the University of Oxford

for the degree of Doctor of Philosophy

Department of Earth Sciences

and

University of Oxford

Trinity, 2014

Supervised by

Helen L. Johnson

Paul R. Holland

Adrian Jenkins

Declaration of Authorship

I, *Thomas Millgate*, declare that this thesis titled 'Ice-Ocean Interactions in North West Greenland' and the work presented in it are my own and have been generated by me as the result of my own original research.

I confirm that:

1. This work was done wholly while in candidature for a research degree at this University;
2. No part of this thesis has previously been submitted for a degree or any other qualification at this University or any other institution;
3. Where I have consulted the published work of others, this is always clearly attributed;
4. I have acknowledged all main sources of help;
5. Parts of this work have been published as:
    - *Millgate et al.* (2013)

Signed:
Date:

Abstract

Ice shelves play an important role in the mass balance of an ice sheet, by providing a link between the ocean and ice. Melting at the base of an ice shelf can play a vital role in its mass balance and stability. Topographic channel features have been found on the base of ice shelves, and have been found to alter melting, however the mechanism behind this alteration is unknown. Petermann Glacier is a major outlet glacier in North West Greenland, draining approximately 6% of Greenland Ice Sheet. It terminates in a long, thin ice shelf, constrained within a high-walled fjord. The ice shelf has pronounced longitudinal channel features on its base, which limited observations suggest direct ocean currents in a mixed layer of ocean and melt waters, focusing melt in these regions. Petermann Glacier underwent two large calving events in 2010 and 2012, and the impact of these events, or possible further calving events, on basal melting is unknown.

Using the MITgcm to model the ocean cavity beneath an idealised ice shelf, this thesis discusses the impact of basal channels on interactions at the ice base and circulation within the cavity. This is supplemented with a modelling investigation into the interactions beneath Petermann Glacier, and the impact of recent calving events. The inclusion of channels was found to have a stabilising effect on the ice shelf by decreasing the mean basal melt rate, caused by the refocusing, and decrease in intensity of, the meltwater layer flow beneath the ice shelf. This stabilisation and resulting 'survivor bias' explains why channels are commonly found on the base of warm water ice shelves. The model of Petermann Glacier found similar melt patterns to observational studies, however with a lesser magnitude. The calving events of 2010 and 2012 removed areas of ice shelf with low melt rates, resulting in little impact on the overall volume of ice removed through ocean melting, though further calving would vastly reduce the volume of ice melted. One consequence of calving is the increase in melting-induced undercutting at the ice front, leading to the potential for enhanced secondary calving.

Part of the results contained within this thesis are published as: Millgate, T., P.R. Holland, A. Jenkins and H.L. Johnson (2013), The effect of basal channels on oceanic ice-shelf melting, *Journal of Geophysical Research Oceans, 118,* doi:10.1002/2013JC009402.

Extended Abstract

The marine-terminating outlet glaciers of the Greenland Ice Sheet can be split into two classifications; tidewater glaciers, where the glacier reaches the coastline and doesn't start to float; and glaciers ending in floating ice shelves. The vast majority of these glaciers are tidewater glaciers with only a handful of ice shelves, constrained within glacial fjords, surviving around the north of the ice sheet (*Moon et al.*, 2012).

The existence of ice shelves in this region has been attributed to the ocean waters in this region being cooler than around more southerly regions of Greenland, which are fed with water from the warm Irminger Current (*Straneo et al.*, 2012). The ocean water temperature is an important factor for the continued existence of these ice shelves as warm ocean waters have been attributed to ice shelf disintegration and glacier acceleration (*Holland et al.*, 2008a; *Rignot et al.*, 2012; *Straneo et al.*, 2010). Low surface slope of the glaciers (*Koch*, 1928) and high levels of sea ice cover in the fjords, slowing down and preventing large iceberg calving events (*Higgins*, 1991) have also been attributed as reasons for ice shelves remaining in this region.

Petermann Glacier in north-western Greenland is one such outlet glacier which terminates in a long thin floating ice shelf. It is one of the most influential glaciers in northern Greenland in terms of both the drainage area of the Greenland Ice Sheet (*Rignot et al.*, 2001) and ice discharge into the ocean (*Rignot et al.*, 1997).

In August 2010 a large calving event occurred, removing about 270-290 km^2 (*Box and Decker*, 2011), retreating the ice front closer to the grounding line than previously recorded (*Falkner et al.*). Although larger than any previously known calving event, it tied in with the ice shelf's near decadal time scale of calving (*Johannessen et al.*, 2011). In 2012 another large calving event occurred, removing a further 120 km^2 from the ice shelf (*Münchow et al.*, 2014). Whether the short time span between these two large calving events is the beginning of a change in the stability of the ice shelf, or it is unrecorded natural variability, is unknown. What we do know is that these two large calving events have occurred over a much shorter time interval, and have resulted in the ice shelf terminus retreating further than previously recorded.

The base of Petermann Glacier's ice shelf was found to have several prominent basal channels, aligned with the direction of ice flow (*Rignot and Steffen*, 2008). Such channels have been found underneath several ice shelves both in Greenland and Antarctica (*Rignot and Steffen*, 2008; *Motyka et al.*, 2011; *Vaughan et al.*, 2012; *Dutrieux et al.*, 2013). These ice shelves have typically experienced strong oceanic thermal driving.

The presence of these channels has been found to have an impact on the oceanog-

raphy within the sub-ice-shelf cavity, directing the meltwater along the channels from the inner cavity towards the ice front (*Payne et al.*, 2007; *Mankoff et al.*, 2012). It has been suggested that this would lead to enhanced melting within the channels and channel deepening (*Payne et al.*, 2007). The importance of basal channels on the stability of ice shelves has been debated. Some studies suggest they decrease the mechanical strength of the ice shelf through crevasse formation as the ice settles into hydrostatic equilibrium (*Rignot and Steffen*, 2008; *Vaughan et al.*, 2012). A model study has shown the channelized redirection of flow beneath the ice shelf prevents the formation of focused high melt rate areas, leading to a reduction in mean basal melt rate (*Gladish et al.*, 2012) and therefore stabilising the ice. The reduced ocean physics of this model study, however, precluded an investigation of the physical mechanism behind this sensitivity.

Using the MITgcm ocean model, this thesis investigates the impact of basal channels on idealised and realistic representations of Petermann Glacier ice shelf, and the underlying physical mechanism present.

The idealised domain was chosen to represent Petermann Glacier, but be adaptable so that the number of channels could be easily altered. The ice shelf thins with a tangential shape, from a draft off 600 m at the grounding line to 60 m at the ice front. Channels with a similar along-shelf profile to the realistic domain are added with a sinusoidal across-shelf profile.

The realistic representation was created using a digital elevation map, created from satellite imagery, corrected using airbourne radar data. Due to the floating nature of an ice shelf, the elevation was subsequently converted to ice draft by applying the assumption of hydrostatic equilibrium. Due to the inherent difficulties with accessing the cavity of an ice shelf, the bathymetry beneath Petermann Glacier is unknown, however both the grounding line (*Rignot*, 1998), and bathymetry for the open ocean section of the fjord (*Johnson et al.*, 2011) are known. Three different bathymetry scenarios were created for the realistic domain to assess the impact of bathymetry on ice-ocean interactions beneath Petermann Glacier.

The idealised model showed that when no basal channels were present, a strong, geostrophically-balanced boundary current was formed in the sub-ice layer directly beneath the ice shelf, rising along the eastern boundary and leaning on the right-hand wall of the fjord. Due to the velocity-dependence of melting, the strongest basal melting was focused underneath the strongest part of the boundary current.

As a small number of wide channels were introduced, the formation of this boundary current was modified, with a circulation within each channel induced instead. This circulation consisted of a southward flow on the western slope of the channel and a northward flow on the eastern slope, with little flow in the channel crests. There was some transfer over the keels between the channels in an eastward direction, leading to slightly faster flows and stronger melting in the more easterly channels. Within each channel, melting was strongest in the steepest part of the ice shelf near the grounding line, where the channels begin, and on the eastern slope of the channels.

The mean melt rate for the whole ice shelf was roughly the same for the 0- and 1-channel cases, but as more channels were introduced, the mean melt rate decreased

monotonically. There was a reduction of approximately 40% in melting between the 1- and 4- channel cases. The introduction of further, narrower channels caused the sensitivity of the mean melt rate to the number of channels to decline, with only a further 8% reduction between the 4- and 8- channel cases.

The change in sensitivity is explained through consideration of the flow beneath the ice shelf. For a smaller number of wide channels, a geostrophic flow circulated around the channels. As more channels were initially added, more keels and crests were introduced to the base of the ice shelf. There was little or no flow beneath these areas, where the isopycnals were flat. This led to a decrease in sub-ice layer flow and hence basal melting.

The introduction of further channels resulted in the channels becoming too narrow for the horizontally sheared circulation to be viable, causing a change to an overturning circulation within each channel. This was much less sensitive to the channel width due to the increase in "no flow" area being smaller, reducing the mean basal melt rate sensitivity.

These results suggest that, although basal channels decrease the mechanical stability of an ice shelf, they also decrease an ice shelf's susceptibility to basal melting. This stabilising effect is a possible explanation as to why basal channels are observed in warm-water ice shelves in Greenland and Antarctica. If the channels stabilise ice shelves, ice shelves with channels are more likely to persist, and a 'survivor bias' makes them more likely to be observed.

The idealised model was also used to assess the impact of changing oceanic conditions within the fjord on the ice-ocean interactions beneath the ice shelf. The changes in conditions included a deepening of the surface stratified layer, the introduction of a seasonal restoring cycle, warming of the subsurface waters and ice shelf calving events.

With the Arctic experiencing lower levels of sea ice cover (*Serreze et al.*, 2007), it is possible that Petermann Fjord could spend longer periods of the year ice-free, allowing the wind within the fjord to have a larger mixing effect on the ocean surface layer leading to a deeper, yet more weakly stratified, surface layer. The model showed that, where the surface stratified layer protrudes underneath the ice shelf, it acted as an insulating layer, protecting the ice base from the meltwater layer and preventing basal melting. The deepening of the surface stratified layer resulted in greater portions of the ice shelf being protected from basal melting, hence leading to a reduction in mean basal melt rate.

The depth of the surface stratified layer plays an important role in controlling melting for the areas of the ice shelf with a shallow ice draft. There are several factors which affect the depth and strength of stratification including freshwater run-off from land melt, sea-ice cover and wind conditions, meaning that the surface stratified layer will vary on a seasonal cycle. During the winter, brine rejection from sea-ice formation results in a more saline surface mixed layer, which can intrude underneath the ice shelf and into channel crests. This surface mixed layer is eroded away in the summer due to a number of factors including freshwater land run-off, sea ice melt and rain. Inclusion of such seasonal forcing in the model showed that the mean basal melt rate closely followed the pattern of mixed layer depth, with greater

levels of basal melting during the summer and weaker levels during the winter. A slight lag was found due to the time it takes for water to fully penetrate the ice shelf cavity from the open ocean.

Ocean warming has been hypothesized as a cause of glacial destabilisation (*Holland et al.*, 2008a; *Christoffersen et al.*, 2011), and model studies have shown ocean warming to enhance melting (*Holland et al.*, 2008b; *Xu et al.*, 2012). The disintegration of Jakobshavn Isbræ's ice shelf has been attributed to the arrival of relatively warm water originating in the Irminger Sea (*Holland et al.*, 2008a), whilst a similar source of warm water has been suggested as the cause of glacial acceleration on Greenlands eastern coast (*Howat et al.*, 2008; *Straneo et al.*, 2010). Both model studies and observations suggest that the subsurface waters of Petermann Fjord have warmed (*Rignot et al.*, 2012; *Johnson et al.*, 2011) and if Petermann Glacier were to follow the trend seen in southern and eastern Greenland, this increase in ocean temperature may lead to an increase in basal melting, glacier acceleration and ice shelf instability.

Increasing the temperature of the subsurface waters in the idealised domain led to a quadratic increase in basal melting. *Johnson et al.* (2011) concluded that there was already more than the required heat being supplied to the ice shelf cavity for the current levels of basal melting, suggesting that an increase in heat content, be it interannual variability or a continuous trend, would not increase this further. Therefore the increased melting found here must depend upon the actual ice-ocean interactions themselves rather than just the further input of heat to the cavity.

In all cases the meltwater layer detached from the base of the ice shelf at the pycnocline depth. This constant detachment indicated that, even though there was an increase in mean melt rate, as long as the pycnocline remained at this depth, the ice shelf would not experience an increase in basal melting above the pycnocline depth as the ocean warms. However greater melt rates near to the grounding line, caused by an increase in thermal forcing, indicate that the ice shelf would thin closer to the grounding line. This thinning near to the grounding line could lead to a decrease in ice shelf stability and increase the probability of large calving events similar to those seen in 2010 and 2012.

The impact of large calving events was assessed in the idealised model and it was found that as the ice shelf retreated, the in-situ melt rates were unchanged, implying that the mean basal melt rate increased. This was caused by the removal of areas of the ice shelf which have a shallower draft and therefore lower melt rates. However the ice shelf decreased at a larger rate than the mean basal melt rate increased, leading to a reduction in ice volume lost by basal melting.

One consequence of ice shelf retreat was a deepening of the draft at the ice front. This resulted in the ice front coming into contact with the deeper warmer waters, leading to large melt rates on the ice front and melting induced undercutting. The increased volume of ice melted from the ice front was smaller than the decrease in volume melted by basal melting, leading to an overall reduction in ice volume melted as the ice shelf retreats. The melting induced undercutting can cause an increase in surface stress near to the ice front, with the potential to cause further calving events, some distance up the ice shelf (*O'Leary and Christoffersen*, 2013).

Modelling of the realistic Petermann Glacier domain was found to provide a qualitative agreement between observations and both the modelled circulation within the fjord and ice-ocean interactions beneath the ice shelf. Smaller melt rates were found than those observed, caused by errors in the observed melt rates and potential discrepancies in model ice shelf geometry.

Comparison of the several different possibilities for the unknown fjord bathymetry showed consistent basal melting, yet varying cavity circulation, suggesting sufficient heat is entering the ice-shelf cavity, irrespective of the chosen bathymetry. However it is worth noting that unknown features not included in the modelled bathymetries, such as seabed ridges, could affect both circulation and ice-ocean interactions.

An investigation into ice shelf calving events showed similar results to those found for the idealised domain, with an increase in mean melt rate, but decrease in total ice volume melted, as the ice shelf retreated. The results indicated that the calving events of 2010 and 2012 had little effect on the basal melt rates and pattern under the remaining ice shelf. Further to the idealised study, it was found that the change in mean basal melt rate was caused by the mean oceanic thermal forcing felt by the ice shelf base increasing as shallow sections of the ice shelf were removed through calving.

It was also found that the melting induced undercutting was more pronounced in a stratified water column, compared to a well mixed water column. This suggests that calving of ice shelves floating in a water column with a large stratification are at greater risk of further calving, compared to those floating in a warmer, less stratified, water column.

Part of the results contained within this thesis are published as: Millgate, T., P.R. Holland, A. Jenkins and H.L. Johnson (2013), The effect of basal channels on oceanic ice-shelf melting, *Journal of Geophysical Research Oceans, 118,* doi:10.1002/2013JC009402.

Acknowledgements

I would firstly like to thank my supervisors, Paul Holland, Helen Johnson and Adrian Jenkins, for their support, encouragement, occasional concern and useful suggestions during the undertaking of this thesis. I have enjoyed working along side them and have gained a lot, both academically and personally, from doing so.

My thanks is also given to my examiners Ros Rickaby and Mark Inall for both the enjoyable conversations and helpful suggestions, which have helped improved my thesis to its current form.

I would like to thank Dr. Humfrey Melling (Institute of Ocean Sciences, BC, Canada) and the captain and crews of the USCGC Healey and the CCGS Henry Larson for the bathymetry and hydrographic data collected in Nares Strait and Petermann Fjord. I would also like to thank Dr Eric Rignot for providing his grounding line data for Petermann Glacier and I would like to acknowledge the use of radar data of Petermann Glacier collected by CReSIS, generated with support from NSF grant ANT-0424589 and NASA Operation IceBridge grant NNX13AD53A.

There are many people at BAS to whom I am indebted for their advice and support, along with general encouragement and interest in the work I have undertaken. I am also thankful to Andrew Meijers and the captain and crew of the RRS James Clark Ross for providing me with the opportunity to experience polar science first hand. I would especially like to thank Cat Horswill, a fellow PhD student, who has helped with the lows and celebrated the highs, making the experience a lot less painful and a lot more enjoyable.

Finally, and by no means least, I would like to thank my new wife Carly, her unwavering support during the process, understanding of my disappearing to conferences around the world and pride in what I have achieved, all mixed with a healthy amount of nagging, has helped me get this thesis to where it is today and without whom this would have been a struggle. I am also indebted to her for organising our wedding whilst I was writing up this thesis, allowing me to concentrate without the added stress that organising a wedding can bring.

Contents

List of Figures

Chapter 1

Introduction

1.1 Aim of Thesis

When glaciers come into contact with the ocean, they either terminate as a tidewater glacier (no floatation occurs) or in an ice shelf, the floating section of a glacier. Ice shelves are in contact with both the atmosphere and the ocean, making them highly sensitive to changes in climatic forcing.

The ocean cavity beneath an ice shelf is inherently difficult to observe, yet the interactions that take place between the ocean and the base of an ice shelf can play an important role in the mass balance of both the ice shelf and the ice sheet. The topography of the base of an ice shelf can also have an important role in modifying these interactions.

It is with this in mind that this study uses a regional, high resolution, general circulation model to study the ice-ocean interactions in the sub-ice cavity of a Greenland ice shelf to address the following questions:

- *How do basal features, such as channels, affect the melting at the base of an ice shelf, and the circulation within the cavity?*
- *What is the impact of potential changes in future oceanic forcing on ice-ocean*

interactions?

- *How do large calving events influence ice-ocean interactions?*

- *How well does the model predict basal melting and oceanic circulation beneath Petermann Glacier, when compared to available estimates and observations?*

1.2 Greenland Ice Sheet

The Greenland Ice Sheet (Fig. 1.1) is one of the planet's two ice sheets. Located in the northern hemisphere, with an area of 1.801×10^4 km^2 (*Kargel et al.*, 2012), and at up to 3 km thick (*Michelsen*, 2013), it contains enough ice to raise global sea levels by 7.36 m (*Bamber et al.*, 2013).

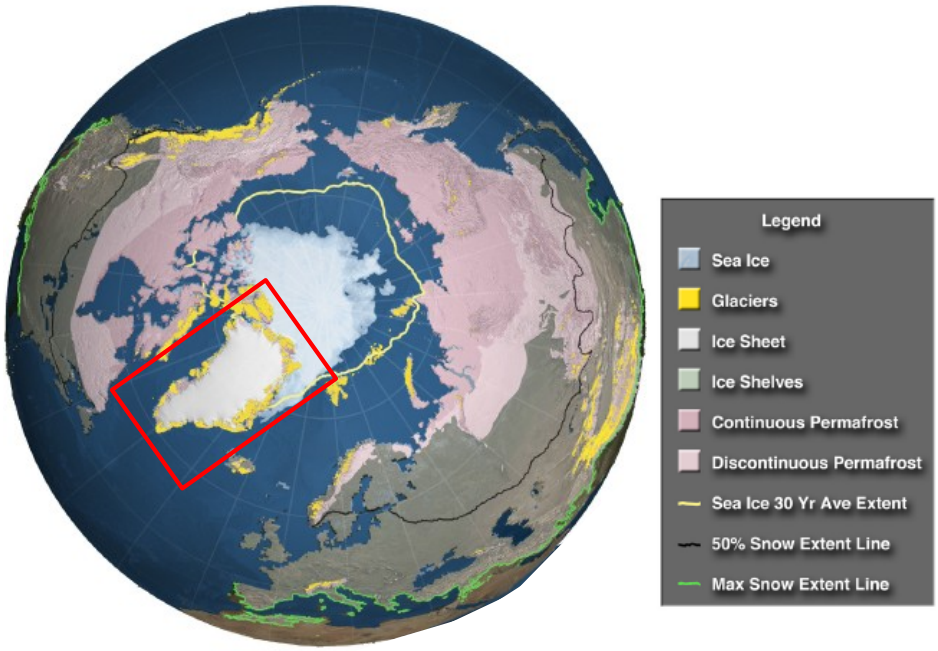

Figure 1.1: Map showing Greenland Ice Sheet (red box) in it's geographical context.The ice sheet's outlet glaciers are highlighted in yellow. (Source: *Vaughan et al.* (2013)).

1.2.1 Ice shelves of Greenland's outlet glaciers

Figure 1.1 shows the location of Greenland's numerous outlet glaciers in yellow. There are three types of outlet glaciers: land-terminating; tidewater glaciers, where the glacier reaches the coastline and doesn't go into flotation; and glaciers ending in ice shelves. *Moon et al.* (2012) surveyed all outlet glaciers with a width of at least 2 km between 1992 and 2007 and found that the vast majority (187 out of 203) were tidewater glaciers and these were found around the whole of Greenland. Of the remaining 16 glaciers, 10 were land-terminating glaciers found in northern and south-western Greenland and only 6 terminated in ice shelves; Petermann, Zachariæ Isstrom, 79N, Ostenfeld, Ryder and Jakobshavn Isbræ. Of these six glaciers, Zachariæ Isstrom and Ostenfeld were found to have lost ice shelf area during this study (*Moon et al.*, 2012), whilst the ice shelf of Jakobshavn Isbræ has since disintegrated (*Weidick et al.*, 2004) and Petermann Glacier has experienced two large calving events (*Falkner et al.*; *Münchow et al.*, 2014).

The remaining ice shelves are all in the northern region of Greenland (*Moon et al.*, 2012) and are constrained within glacial fjords (*Higgins*, 1991), with, in some cases, high fjord walls and a sill near the entrance to the fjord (e.g. *Johnson et al.* (2011)). The existence of ice shelves in this region has been attributed to the ocean waters in this region being cooler than around more southerly regions of Greenland, which are fed with water from the warm Irminger Current (*Straneo et al.*, 2012). The ocean water temperature is an important factor for the continued existence of these ice shelves as warm ocean waters have been attributed to ice shelf disintegration and glacier acceleration (*Holland et al.*, 2008a; *Rignot et al.*, 2012; *Straneo et al.*, 2010). Low surface slope of the glaciers (*Koch*, 1928) and high levels of sea ice cover in the fjords, slowing down and preventing large iceberg calving events (*Higgins*, 1991) have also been attributed as reasons for ice shelves remaining in this region.

1.2.2 Ice shelf mass balance

The balance between the addition and removal of mass from an ice-shelf can tell us about it's current state. If the mass balance is positive (more mass addition than removal) then the ice shelf will grow, if it is negative (more removal than addition) then it will shrink, whilst if it is neutral (addition balances removal) then it is in a steady state. Ice shelf growth can occur through an increase in either ice shelf thickness, extent or both. Likewise a shrinking of an ice shelf can occur through reduction in either thickness, extent or both.

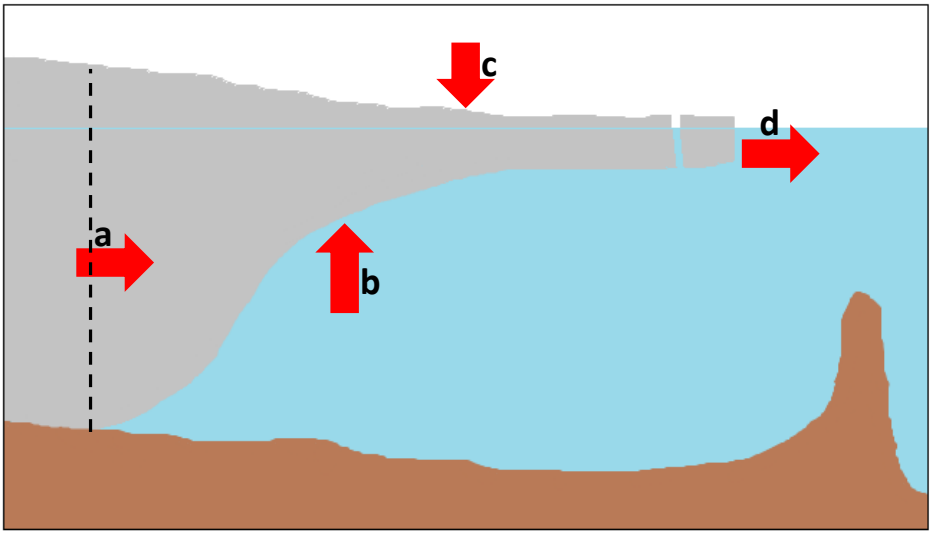

Figure 1.2: Schematic showing the mass balance of an ice shelf with a) ice flux across grounding line, b) ice base mass balance, c) surface mass balance and d) iceberg calving.

The mass balance is affected by several different processes, namely the flux across the grounding line, the ice base mass balance, the surface mass balance and calving at the ice front (Fig. 1.2). The flux across the grounding line brings ice from the grounded section of the glacier into the ice shelf and is thus a positive term in the mass balance. The ice base mass balance is the sum of ice lost due to oceanic melting and the addition of ice due to oceanic water freezing onto the base of the ice shelf. The surface mass balance is the sum of ice lost due to melting and the accumulation of snow over the ice shelf. Calving is the loss of large chunks of ice from the ice front,

and is therefore a negative term in the mass balance.

The relative importance of each term in the balance varies between ice shelves and is dependent on many factors including 1) air temperature, 2) ocean temperature, 3) sea-ice cover, 4) topography and 5) local precipitation. These relative sizes can be used to hypothesize the future stability of an ice shelf under differing scenarios.

1.2.3 Ice sheet mass loss mechanisms

There are several different mechanisms through which ice can be removed from an ice sheet, these includes, but are not restricted to, the following:

1) Air temperature, when above the local freezing point, will increase the levels of surface melt. However an increase in air temperature will also increase its moisture bearing capacity, allowing for a higher level of snowfall. The surface air temperature over Greenland has been increasing for the past two decades (*Box et al.*, 2009), with 2010 being an exceptionally warm year for west Greenland where Nuuk experienced it's warmest year since records began (*Tedesco et al.*, 2011).

2) Ocean circulation brings warm water into contact with the edge of the ice sheet. The interactions that occur here have a major effect on the ice sheet's mass budget (*Holland et al.*, 2008a; *Pritchard et al.*, 2012). The warm ocean waters provide enough thermal forcing to drive the high submarine melt rates seen at both ice shelves (*Holland and Jenkins*, 1999; *Rignot and Jacobs*, 2002; *Pritchard et al.*, 2012) and tidewater glaciers (*Holland et al.*, 2008a; *Rignot et al.*, 2010).

3) Oceanic ice melt rates can be very large (*Motyka et al.*, 2003; *Dutrieux et al.*, 2013), with the melt rate proportional to the oceanic thermal forcing and oceanic flow speed (*Holland and Jenkins*, 1999). The acceleration of glaciers in southern Greenland at the beginning of the century has been attributed to enhanced melting caused by the intrusion of warm water of subtropical origin into fjords (*Holland et al.*, 2008a; *Murray et al.*, 2010; *Straneo et al.*, 2011). Modelling studies have shown that

an increase in submarine melting leads to a reduction in back stress felt by the glacier, leading to glacier acceleration (*Payne*, 2004; *Nick et al.*, 2013; *O'Leary and Christoffersen*, 2013).

4) As surface meltwater drains through the ice shelf to the bed, water pressure is increased and basal friction is reduced, leading to a speed up of the ice above, resulting in an increase in ice discharge. This process is known as basal lubrication (*Zwally et al.*, 2002). Drainage events leading to basal lubrication are common in northeast and southwest Greenland, but rarely seen in the southeast and northwestern regions (*Selmes et al.*, 2011).

5) Iceberg calving, from both ice shelves and tidewater glaciers, is an important mechanism for mass loss. It can lead to a reduction in buttressing, through a loss of back stress, leading to an acceleration of the glacier and hence an increase in ice crossing the grounding line (*Nick et al.*, 2012). The potential causes of calving are varied and include melt-driven processes (*Benn et al.*, 2007), ocean swell and tsunamis (*MacAyeal et al.*, 2006; *Brunt et al.*, 2011) and as a final response to gradual change (*Scambos et al.*, 2000).

1.2.4 Changing Arctic and Greenland

The latest Intergovernmental Panel on Climate Change (IPCC) report confirms that over the last two decades, the ice sheet has been losing ice mass and contributed to global sea level rise (Fig. 1.3), with an average ice mass change of -121 [-149 to -94] Gt/a (equivalent to a sea level rise of 0.33 [0.41 to 0.26] mm/a) between 1993 and 2010. Over the last five years of this period, the average rate of change in ice mass increased to -229 [-290 to -169] Gt/a (a sea level rise equivalent of 0.63 [0.80 to 0.47] mm/a) (*Vaughan et al.*, 2013).

van den Broeke et al. (2009) have shown that the increase in mass loss can be split approximately evenly between the surface mass balance (surface melt and runoff)

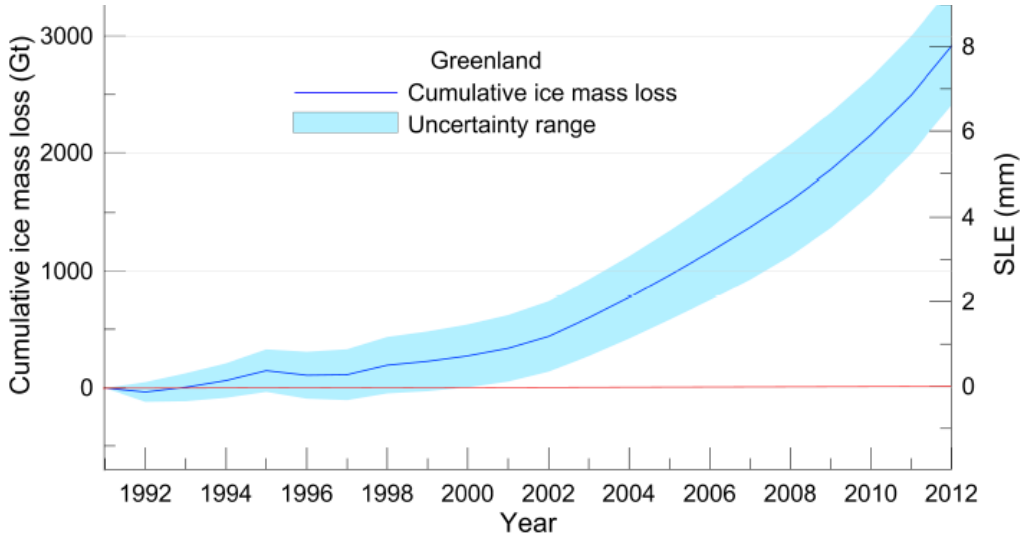

Figure 1.3: Cumulative Greenland Ice Sheet mass loss and sea level equivalent (Source: *Vaughan et al.* (2013).

and ice discharge across grounding lines of the ice sheet's outlet glaciers. Regionally, however, the relative importance of these two mechanisms varies, with surface mass balance being dominant in north, southwest and northeast regions, whilst discharge across grounding lines is dominant in the southeast, west and northwest regions (*Howat et al.*, 2007; *van den Broeke et al.*, 2009; *Pritchard et al.*, 2009).

During this period of increasing mass loss, the surface melt area has been increasing, with an acceleration over the past few years (*Fettweis et al.*, 2011; *Tedesco et al.*, 2011). In July 2012, an extreme melt event occurred, lasting a couple of days, where the melt area increased to cover 90% of the ice sheet (*Tedesco et al.*, 2013). This increase in surface melt area has led to a change in the surface albedo of the ice sheet, allowing more solar energy to be absorbed by the ice sheet, leading to higher levels of surface melting. Over the 12 summers between 2000 and 2011, the largest change in albedo (-0.091 $\pm$ 0.021) was found over the coastal ablation area whilst a significant change in albedo of -0.046 $\pm$ 0.006 was observed over the accumulation area (*Box et al.*, 2012).

It should be noted, however, that this positive feedback is not seen over the

whole ice sheet. In the ablation zone, the cold season accumulated snow is being melted earlier, exposing the darker, impurity rich, bare ice surface, reducing the albedo and hence amplifying melt volume. This positive feedback accounts for 85% of the increase in surface melt in the ablation area between 2000 and 2011. In the accumulation area, melting occurs over a much shorter time period, and the additional absorbed solar energy is used in snowpack heating rather than surface melting, providing a dampening to the positive albedo feedback seen in the ablation area. However this dampening of the positive feedback is not sufficient to balance the effect of warming, and there is a resultant overall albedo decline (*Box et al.*, 2012).

Results from the Gravity Recovery and Climate Experience (GRACE) satellite show that ice loss in southeast Greenland was greatest in 2005 with a subsequent decrease in ice loss, whilst ice loss decreased in the northwest after 2007 (*Khan et al.*, 2010; *Chen et al.*, 2011; *Harig and Simons*, 2012). These results agree with measurements of ice discharge from major outlet glaciers, confirming the importance of ice flowing across grounding lines in these regions (*van den Broeke et al.*, 2009).

In the northwest, it is probable that the increase in ice mass loss seen between the 1996-2006 period and 2006-2010 period was at least partially caused by higher accumulation rates in the late 1990's compared to other years (*Sasgen et al.*, 2012), however an increase in outlet glacier flow speed between 2000-2010 indicates that ice dynamics also played an important role (*Moon et al.*, 2012). An 80-year-long aerial photograph record of the south east shows that many land-terminating glaciers retreated faster in the 1930's, whilst tidewater glaciers retreated at a faster rate during the most recent warming (*Bjørk et al.*, 2012).

The environment of the Arctic and regions surrounding Greenland is changing with the potential for global impacts through climate feedback mechanisms. Some of these changes have been in the form of long term trends, such as the decrease in

sea ice extent (*Serreze et al.*, 2007), whilst others have been more sudden, such as the disintegration of Ayles Ice Shelf in northern Canada (*Copland et al.*, 2007), but they all either have an affect on, or provide insight into, the long term future of the Greenland Ice Sheet and its ice shelves.

The disintegration of ice shelves in northern Canada (*Copland et al.*, 2007) and the fast retreat of Jakobshavn Isbræ's ice shelf (*Holland et al.*, 2008a; *Weidick et al.*, 2004) indicate that ice shelves around Greenland and the Arctic regions are susceptible to sudden, potentially irreversible, changes which have a knock-on effect on the stability of the ice sheet.

Over the latter decades of the 20th Century and into the 21st Century the ocean temperatures in the subpolar North Atlantic have been increasing (*Bersch et al.*, 2007; *Straneo and Heimbach*, 2013). Figure 1.4 shows the major oceanic currents around Greenland. It shows that the warming North Atlantic water would first come into contact with marine terminating glaciers in the southeast of Greenland, before spreading to the southwest and then northwest. This circulation agrees with the observed spread of ice mass loss into the northwest of Greenland (*Khan et al.*, 2010). There is some spatial variability in terms of glacier retreat along the western coast of Greenland, for instance Jakobshavn Isbræretreated prior to the more southerly Kangerlussuaq glacier, however the overall trend is that described previously.

An increase in subsurface water temperature was found to have a linear effect on melting at the calving face of tidewater glaciers (*Xu et al.*, 2012), whilst *Holland et al.* (2008b) found a quadratic relationship between subsurface water temperature and ice shelf basal melting. In both these studies, under some assumptions, melt rate was expressed as the product of mixed layer flow speed and the temperature difference between the mixed layer and deep-water. *Xu et al.* (2012) used a three-dimensional z-coordinate general circulation model containing the vertical ice face of the calving front, with melting occurring on the vertical face, whilst the model

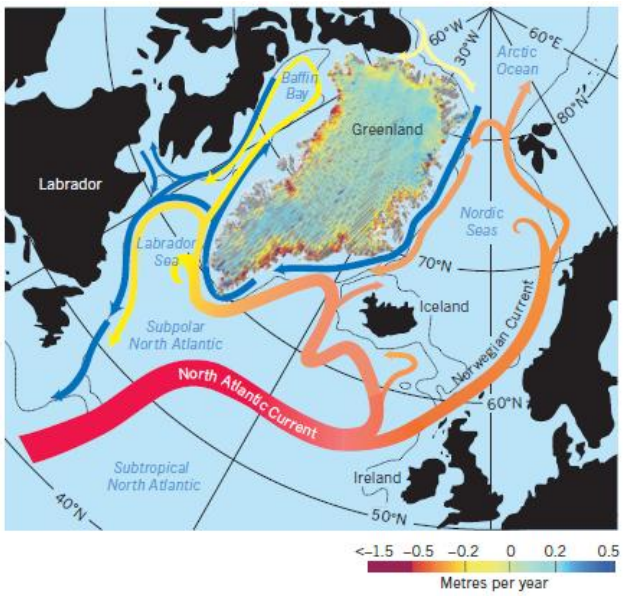

Figure 1.4: Schematic of the large scale ocean circulation around Greenland. The Atlantic-origin pathways are in red to yellow, whilst Arctic-origin pathways are in blue. The Dynamic thinning of the Greenland Ice Sheet (in m/yr) is superimposed (Source: *Straneo and Heimbach* (2013)).

used by *Holland et al.* (2010) was a three-dimensional iso-pycnic coordinate model, consisting of ten uniform density layers beneath a mixed layer which interacts with the overlying ice shelf or atmosphere. In the model of *Holland et al.* (2010) melting occurred along the base of a floating ice shelf.

In both cases the relationship between the temperature difference and ocean warming was found to be linear. *Xu et al.* (2012) found no increase in ocean flow speed with ocean warming, whilst *Holland et al.* (2008b) found a linear increase in ocean flow speed, hence explaining the difference in relationships between ocean warming and basal melting in these two studies. These relationships show that marine terminating glaciers and hence their grounded portions, are highly affected by oceanic warming, with *Holland et al.* (2008a) attributing the acceleration of Jakobshavn Isbræ, prior to it's rapid retreat, to a warming of subsurface ocean waters.

The extent of Arctic sea ice has been decreasing since the late 1970's with negative trends found in the annual means as well as for the four seasons and all months

(*Serreze et al.*, 2007; *Parkinson and Cavalieri*, 2008). As well as a reduction in extent, sea ice thickness was found to have reduced after the 2007 minimum by 0.26 m compared to the previous 6-year mean, with the thinning more pronounced in the Western Arctic with reduction of 0.49 m compared to the 6-year mean (*Giles et al.*, 2008). An increase in surface air temperature has been raised as one potential driver of this decrease (*Serreze et al.*, 2007), however other thermodynamic and dynamic processes such as changes in radiative fluxes and ocean currents have been suggested.

The observed decrease in sea ice extent has led to an increase in area of darker open water that readily absorbs solar radiation, increasing the heat content of the surface mixed layer. This has the potential for multiple impacts, including the positive feedback of the warmer water melting further sea ice, in turn increasing the area of open water, leading to greater absorbtion of solar radiation and further increase the heat content of the ocean (*Serreze and Barry*, 2011).

This increased absorption of solar radiation in the Arctic climate system can affect the Greenland Ice Sheet in two ways. The warmer water of the Arctic Ocean is advected southwards through both Nares Strait, powered by the Beaufort Gyre, and through Fram Strait in the East Greenland Current. This warmer water can propagate into Greenland's fjords and come into contact with outlet glaciers, increasing oceanic melting and glacier acceleration. Whilst the increase in heat transfer from the ocean to the atmosphere in the winter due to a smaller ice extent (*Serreze and Barry*, 2011) can lead to warmer winter air temperatures with the potential to increase ice sheet surface melt and hence thinning and acceleration.

1.3 Ice-Ocean Interactions

Ice-ocean interactions include, but are not restricted to, basal melting, basal freezing and water mass transformation. These interactions are controlled by the circulation of the ocean beneath the ice shelf.

1.3.1 Circulation beneath an ice shelf

Melting at the base of an ice shelf is dependent on the temperature of the water in contact with the ice shelf being greater than the in-situ freezing point, which is dependent on pressure and the salinity:

$$T_F = aS_b + b + cp \tag{1.1}$$

where T_F is the in-situ freezing point, S_b is the salinity, p is the pressure, $a = -0.0575\,^{\circ}\mathrm{C\ psu}^{-1}$, $b = 0.0901\,^{\circ}\mathrm{C}$ and $c = -7.61 \times 10^{-4}\,^{\circ}\mathrm{C\ Pa}^{-1}$. An increase in either pressure or salinity will result in a decrease in the in-situ freezing point. It is this decrease in T_F with depth that plays an important role in ice-ocean interactions. However, it is not just T_F that is important to the melt rate, the internal temperature of the ice shelf, roughness of the ice base, temperature of the water in contact with the ice base, and the speed with which that water flows are all important factors. Full details are given in Section 3.2.

A turbulent boundary layer is formed by the water flowing past the base of the ice shelf. It is through this boundary layer that the energy required for basal melting and freezing is transported. If the boundary layer temperature is greater than T_F, then melting occurs. The meltwater mixes with the boundary layer, causing a freshening and cooling. This freshening causes the boundary layer to be less dense than the surrounding water, and it rises up the ice base. As the fresher water rises, T_F changes. If the temperature of the boundary layer is still greater than T_F, further melting will occur resulting in continued freshening and cooling of the boundary layer. This continues until one of two things happen. Either the meltwater reaches a level of neutral buoyancy and flows away from the ice shelf, or the boundary layer becomes cooler than the in-situ freezing point.

When the buoyancy layer becomes cooler than the in-situ freezing point, seawa-

ter freezing starts to occur on the base of the ice shelf, causing an increase in the boundary layer temperature and salinity, further altering it's buoyancy. The boundary current continues to rise up the base of the ice shelf until it either reaches a level of neutral buoyancy or it reaches the surface (Fig. 1.5).

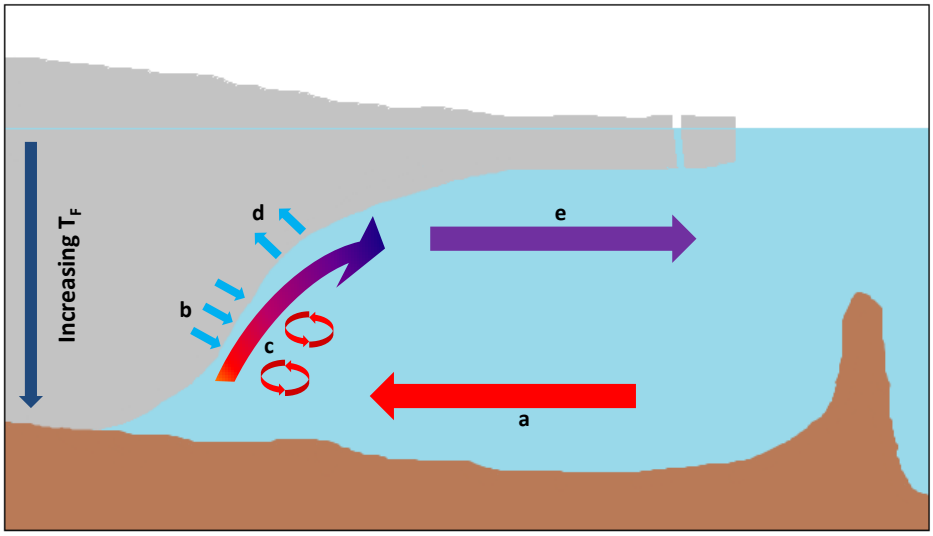

Figure 1.5: Schematic showing the circulation within a sub-ice shelf cavity, a) warm water enters the cavity, b) warm water causes basal melting, c) change in buoyancy causes mixed layer to rise and entrain warm water, d) mixed layer is cooler than local freezing point and seawater freezes onto base of ice shelf and e) mixed layer reaches a level of neutral buoyancy and flows away from the ice shelf.

As described above, relatively warm water comes into contact with the base of an ice shelf, causing the ice to warm until it melts. When considering the energy budget, to a first approximation some assumptions can be made. The energy required to warm the ice to it's melting temperature (sensible heat transfer from the ocean to the ice) is small relative to the energy required to melt the ice (latent heat uptake) and can therefore be neglected (Latent heat uptake : sensible heat transfer = 334:2 $\mathrm{Jkg}^{-1}\,^{\circ}\mathrm{C}^{-1}$). The energy required to heat the meltwater is also small relative to the latent heat (due to the small volume of meltwater compared to oceanic water) and can also be neglected. Under these assumptions it can be shown that the boundary layer will have temperature (T_M) and salinity (S_M) properties which follow the line

in Θ - S space defined by (*Gade*, 1979; *Jenkins*, 1999):

$$T_M(S_M) = T_O + \frac{L}{c_O}\Big(1 - \frac{S_O}{S_M}\Big), \tag{1.2}$$

where T_O and S_O are the temperature and salinity of the warm ocean waters prior to melting, L is the latent heat of fusion for ice and c_o is the specific heat of sea water. This line is known as a Gade Line and can be calculated for ocean waters with differing properties and is useful for determining whether water has been modified by interactions with an ice shelf. When plotted in potential temperature-salinity space (Θ - S space), water which has been modified by an ice shelf will lie on the Gade Line, whilst water that has been modified by other means, such as freshwater run-off, will lie off the line.

1.3.2 Current knowledge on channel influenced melting

Channels carved into the base of ice shelves (basal channels) have been recorded in several ice shelves around both Greenland and Antarctica, typically those with a strong oceanic thermal driving. In Greenland, *Rignot and Steffen* (2008) found that the floating tongue of Petermann Glacier has pronounced channels aligned in the direction of ice flow, while *Motyka et al.* (2011) revealed the existence of a large channel in the base of Jacobshavn Isbræ's ice tongue before it's retreat from 1998 onwards. Basal channels have also been found under the ice shelf of Antarctica's Pine Island Glacier (*Payne et al.*, 2007; *Mankoff et al.*, 2012; *Vaughan et al.*, 2012; *Dutrieux et al.*, 2013).

Both *Payne et al.* (2007) and *Mankoff et al.* (2012) found that the presence of these channels had an impact on the oceanography within the sub-ice-shelf cavity, directing the meltwater along the channels from the inner cavity towards the ice front. *Payne et al.* (2007) suggested this would lead to enhanced melting within the

channels and channel deepening. Instead, *Dutrieux et al.* (2013) show that these channels are carved by ocean melting near the grounding line, and then diminished downstream by melting at the keels between channels. *Payne et al.* (2007) found that the channeling of meltwater plumes resulted in enough residual heat reaching the sea surface at the ice front to cause the formation of small polynyas. *Mankoff et al.* (2012) noted that basal channels are common on ice shelves, but are only prominent on those which undergo intense basal melting.

There are several proposed mechanisms for the formation of basal channels. *Gladish et al.* (2012) found that undulations in ice thickness at the grounding line are amplified by oceanic melting to form longitudinal channels, whilst channels failed to form under an ice shelf with a constant grounding line thickness. *Le Brocq et al.* (2013) suggest that ice shelf channels can be formed by subglacial water crossing the grounding lines in a channelized manner, entraining warmer ocean water, inducing large localised melt rates, forming small basal channels which are further enhanced by oceanic melting. *Sergienko* (2013) found that in the presence of lateral shear, basal channels can spontaneously appear, even without undulations at the grounding line.

The question of the overall importance of basal channels to ice shelf stability remains open. *Rignot and Steffen* (2008) suggested that there is an increase in mechanical weakness at the crest of channels, where the ice is thinnest. *Vaughan et al.* (2012) showed that the settling of crests and keels towards hydrostatic equilibrium is responsible for fracturing the ice, weakening it further.

In contrast, *Gladish et al.* (2012) formulated a coupled ice shelf-meltwater layer model, finding that basal channels actually increased the stability of ice shelves by preventing the development of focussed high melt rates which melted completely through the ice shelf in the absence of channels. Moreover, the basal melt rate of the ice shelf decreased monotonically with an increasing number of (smaller) channels. The reduced ocean physics in the simple model of *Gladish et al.* (2012), however,

precluded an investigation of the physical mechanism behind this sensitivity.

1.4 Petermann Glacier

1.4.1 Introduction

Petermann Glacier, named after the German geographer and cartographer August Petermann, is a major outlet glacier on the north-western coastline of Greenland, located at approximately 81°N and 61°W (Fig. 1.6). The glacier flows northwest into Petermann Fjord where it forms a long thin floating ice shelf. The fjord has high cliff faces on each side and narrows from 20 km at the grounding line to 15 km near the ice front, after which it opens out into Hall Basin in Nares Strait, which links the Arctic Ocean to the north with Baffin Bay to the south (*Johnson et al.*, 2011). It is one of the most influential glaciers in northern Greenland in terms of both the drainage area of the Greenland Ice Sheet (*Rignot et al.*, 2001) and ice discharge into the ocean (*Rignot et al.*, 1997). It is one of four Greenland outlet glaciers where a significant portion of its drainage basin is substantially below sea level (*Bamber and Layberry*, 2001). Petermann Glacier is also one of only two Greenland glaciers which have retained a significant floating ice shelf (*Falkner et al.*).

Petermann Fjord was first discovered in August 1871 by the U.S. Steamer *Polaris* expedition (*Koch*, 1928), however it was not until 1876 that Coppinger and Fulford realized that the fjord was filled with a glacier and it was not until 1892 that Peary discovered that the glacier reached far inland (*Koch*, 1940). The presence of the floating ice shelf was not noted until 1917, when *Koch* (1928) discovered that the downstream section of the glacier beyond a line drawn between Cape Agnes and Cape Coppinger was afloat.

In 2010 the floating section of the glacier was observed to be approximately 70 km long, 20 km wide and thinned from 600 m at the grounding line to 60 m at the

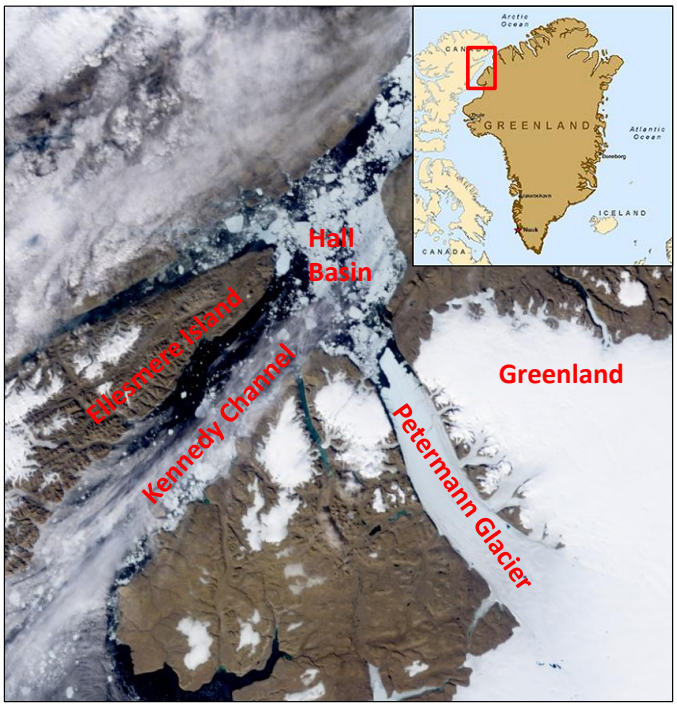

Figure 1.6: Modis image from 28th July 2010 showing Petermann Glacier, Hall Basin, Ellesmere Island and Kennedy Channel.

ice front (*Johnson et al.*, 2011). Since 2010 there have been two large calving events which are discussed in section 1.4.5. The ice front was first mapped by the British Arctic Expedition in 1876, and subsequently in 1922 where it had a similar position and again in 1962 where it was within 6 km of the first mapped position (*Falkner et al.*). Historical aerial photographs suggest that the ice front position changed very little in the later half of the 20th century (*Higgins*, 1991).

Despite the evidence of stability of the ice front position, Petermann Glacier is far from slow moving. It flows at over 1 km/a (*Higgins*, 1991; *Rignot et al.*, 1997) making it the fastest flowing outlet glacier in northern Greenland (*Rignot et al.*, 1997), with 12 ± 1 Gt/a of ice crossing the grounding line each year (see section 1.4.3).

1.4.2 Oceanography of Petermann Fjord and Nares Strait

Petermann Fjord opens into the Hall Basin section of Nares Strait, which connects the Arctic Ocean in the north to Baffin Bay in the South, and runs between Ellesmere Island and Western Greenland. Nares Strait, along with Fram Strait to the east of Greenland, provide important pathways for freshwater fluxes towards the North Atlantic (*Aagaard and Carmack*, 1989). Simple models suggest that freshwater transport through Fram Strait is only approximately 60% of that transported through Nares Strait and the Canadian Arctic Archipelago (CAA) (*Steele et al.*, 1996), however contributions of ice through the CAA are small due to the presence of land-fast ice (*Melling et al.*, 2008).

Rabe et al. (2010) found that the 3-year mean geostrophic velocity across Kennedy Channel, just to the south of Hall Basin and Petermann Fjord, had two distinct surface-intensified southward flows, one on the eastern side of the channel and one in the middle of the strait with velocities up to 0.20 and 0.14 m/s respectively. Direct ADCP measurements by *Münchow and Melling* (2008) found a northward flow near the coast of Greenland during the same time period.

The water on the Ellesmere Island side of the strait was found to be the coolest and freshest, with the water warming and becoming more saline with both depth and moving across the strait to Western Greenland. The isopycnals were found to generally have their maximum slope in the centre of the channel which is consistent with the enhanced flow in the centre of the strait (*Rabe et al.*, 2010).

Johnson et al. (2011) recorded the presence of a sill in the mouth of Petermann Fjord separating the fjord from the adjacent Nares Strait, with the sill no deeper than about 450 m. They found that the water column structure was similar to that of many Arctic regions with a cold fresh water mass overlaying a warmer, saltier layer of modified Atlantic Water. Below about 100 m, both isotherms and isohalines sloped across the fjord with cooler, fresher water on the northeastern side of the

fjord, with the coldest water at a depth of approximately 50 m on the northeastern side. *Johnson et al.* (2011) estimated a necessary heat flux into the fjord of 1.1×10^{11} W to melt the ice shelf at the rate reported by (*Rignot and Steffen*, 2008) (0.327 mSv). Using the information collected across a section near the ice front, *Johnson et al.* (2011) calculated a net heat transport into the fjord of 3.1×10^{11} W, indicating that, at least during summer when the measurements were made, there was ample heat throughout the water whole water column to melt the volume of ice calculated by *Rignot and Steffen* (2008) (Section 1.4.3), including in the coldest water, with temperatures several degrees greater than the in-situ freezing temperature at depths greater than 200 m. The surface salinity was found to be similar to that of water in Nares Strait.

Johnson et al. (2011) found that below a depth of 185 m, the $\Theta - S$ profiles close to the north eastern fjord wall exhibited a slope of approximately 2.5 °C/PSU which is similar to the Gade line for the modified Atlantic Waters found in Petermann Fjord. Above this depth and away from the north-eastern wall, the profiles have a shallower slope in Θ - S space, indicating the modified Atlantic Water is mixing with fresher water, without providing the latent heat required to accomplish melting. These profiles indicate that the meltwater leaves the ice shelf cavity along the north-eastern boundary between depths of approximately 185 and 500 m. The intrusion of a relatively low density surface layer blocks the rising meltwater plume, forcing it to detach from the base of the ice shelf, explaining why no signal is seen above approximately 135 m. Water properties below the sill depth were relatively homogenous and distinct from those at corresponding depths in Nares Strait, indicating that the fjord had been filled to sill depth by Nares Strait water from within a narrow range of depths. Figure 1.7 is a graphical representation of the distribution of water masses within Petermann Fjord.

Hydrographic sections across the fjord, taken in 2007 and 2009, were used to

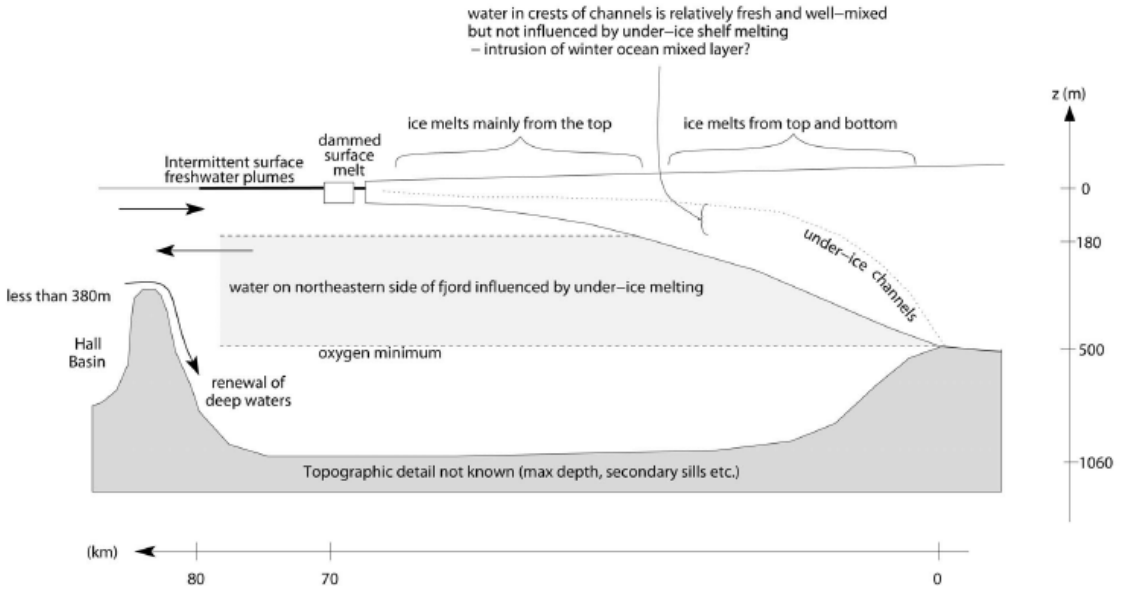

Figure 1.7: Schematic representing the distribution of water masses within Petermann Fjord (Source *Johnson et al.* (2011)).

determine the geostrophic flow within the fjord. In determining the flow, a uniform barotropic velocity was added across the section to ensure there was no net flow into the fjord above 500 m. This was an approximation due to the fjord extending deeper than 500 m, and there being a small net flux out of the fjord equal to the amount of freshwater crossing the grounding line. Below 50 m, there is a flow out of the fjord on the northeastern side, with 2009 velocities reaching a maximum of 0.2 m/s at a depth of 100 m. The outward flow was compensated by a flow into the fjord on it's southwestern side, with the inward flow extending to the surface. The 2007 velocity field was similar to the 2009 data, with weaker velocities (*Johnson et al.*, 2011).

Properties of the water between 180 and 500 m depth on the southwestern side of the fjord are indistinguishable from those from north Kennedy Channel (just south of the fjord mouth) in $\Theta - S$ space which, when paired with the inflow described above, suggests that water from the northward flow in Kennedy Channel enters into

the fjord along the southwestern side (*Johnson et al.*, 2011).

Tidal currents within Petermann Fjord were calculated by *Johnson et al.* (2011) using shipboard ADCP measurements, assuming htat the tide was entirely semi-diurnal. The tidal amplitude was found to decrease by a factor of 2 from 0.16 m/s at a depth of 30 m, to 0.08 m/s at a depth of 100 m. These tidal amplitudes are smaller than those recorded in Nares Strait which can reach 0.24 m/s (*Münchow and Melling*, 2008). The decrease in tidal amplitude may be caused by either the strong stratification within the fjord and/or inertial oscillations which have a period similar to that of the semidiurnal tide at this latitude. As Petermann Fjord is north of the critical latitude for the M2 tide (74.5 °N), density anomalies generated between the barotropic tide and the sill are unlikely to propagate as internal waves, with the energy channeled into near-inertial motions instead (*Johnson et al.*, 2011).

Although the tidal amplitudes are smaller than those seen in Nares Strait, tides are a potential source of kinetic energy for mixing underneath the ice shelf, which has implications for the ice-ocean interaction processes, detailed in Chapter 3, which govern basal melting (*Johnson et al.*, 2011).

1.4.3 Mass balance of Petermann Glacier Ice Shelf

The mass balance of Petermann Glacier Ice Shelf was calculated by *Rignot and Steffen* (2008). Radarsat-1 InSAR ice velocity data was used between the years of 2000 and 2006, to show that the ice shelf could be treated as stable in terms of ice velocity interannual variability.

Grounding line ice thickness of 600 m was recorded by Kansas University's 150-MHz Ice Sounding Radar (*Gogineni et al.*, 2001), which combined with the InSAR velocity data, provided an ice input estimate of 12 ± 1 Gt/yr. As discussed in Section 1.2.2, there are three main processes through which an ice shelf can lose mass; iceberg calving, surface mass balance and ice base mass balance.

Higgins (1991) estimated iceberg production at Petermann Glacier to be 0.6 Gt/yr. *Rignot and Steffen* (2008) deployed two automated weather systems on the ice shelf in 2002 to measure the surface energy balance and calculated a surface ablation of 1.2 m/yr water equivalent between the years of 2002 and 2005, whilst annual snow accumulation was negligible in 2002 and approximately 10 cm between 2003 and 2005 (*Steffen and Box*, 2001). The remainder of the mass lost from the ice shelf, approximately 80%, occurs through basal melting.

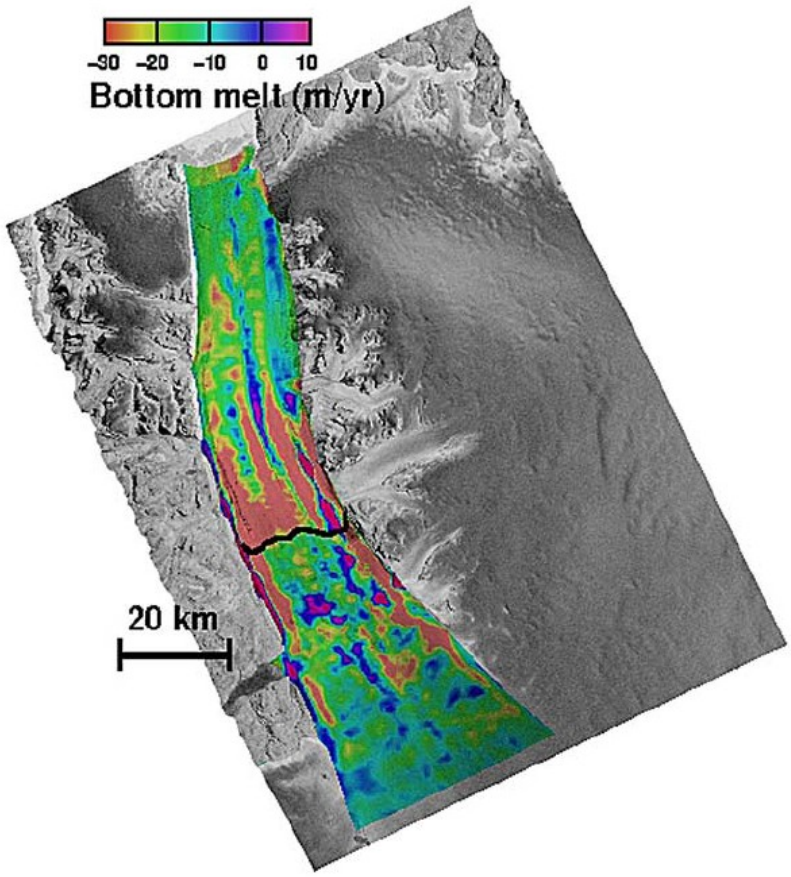

Figure 1.8: Petermann Glacier steady state basal melt rates (m/y) calculated from divergence of ice flux. The black line represents the grounding line (Source: *Rignot and Steffen* (2008)).

Rignot and Steffen (2008) calculated basal melt rates (Fig. 1.8) from the divergence of ice discharge assuming that the ice thickness is in steady state, and a

uniform 1.2 m/yr surface melt rate. Melt rates were found to increase from 0 m/yr near the grounding line to a maximum of approximately 25 m/yr 10 km downstream and subsequently decrease towards the ice front. The whole width of the ice shelf was not used in these calculations as ice thickness measurements were not well constrained along the ice shelf/fjord margins. *Johnson et al.* (2011) calculated that, in summer time at least, there was ample heat contained in the modified Atlantic Water entering the fjord to account for these high levels of basal melting.

1.4.4 Presence of basal channels

Whilst calculating the mass balance, *Rignot and Steffen* (2008) noticed pronounced across-shelf variations, or channels in ice thickness. These channels were 1-2 km wide, 200-400 m deep, spaced approximately 5 km apart and were aligned with the ice shelf flow direction (Fig. 1.9). The channels were found to develop initially near the ice-shelf's grounding line, however there were no significant variations in ice thickness on the grounded ice. Their formation was therefore attributed entirely to ice-ocean interactions.

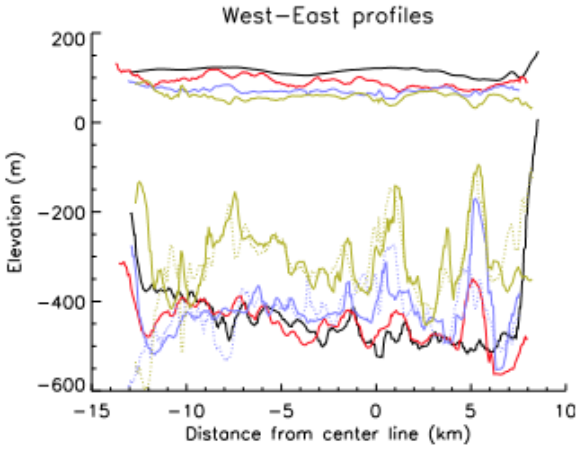

Figure 1.9: Ice Sounding Radar across-shelf profiles of Petermann Glacier's ice shelf surface and base. The black and red profiles are across the grounded section of the ice shelf, whilst the blue profile is close to the grounding line and the yellow profile further downstream form the grounding line (Source: *Rignot and Steffen* (2008)).

Airborne radar data profiles, collected before the 2010 calving event, (see section 2.1.2) taken along both channel crests and keels, show that the channels deepen rapidly by approximately 20 km upstream, after which the crest remains at a relatively constant depth for the rest of the ice shelf, whilst the channel keels tend to shallow linearly. The channel keel and crest profiles approach the same depth approximately 50 km downstream from the grounding line, suggesting that at this location the channels have been removed. This channel structure is confirmed by a satellite digital elevation model of the ice surface, which, since the ice is floating, can be used to infer the topography of the ice shelf base by applying Archimedes' principle (see section 2.1.1).

1.4.5 Recent ice-island calving

As seen in section 1.4.3, calving accounts for only a small portion of the mass lost from Petermann Glacier's ice shelf. *Higgins* (1991) showed that icebergs calve as large tabular bergs at intervals of 5-10 years or more and predicted that the largest tabular bergs were of the order 12 km by 10 km. A review of calving events between 1958 and 2001 showed this to be largely true, with three large calving events in this period. Between 1959 and 1961 the ice-shelf calved approximately 153 km^2 (*Higgins*, 1991; *Johannessen et al.*, 2011), a further 168 km^2 calved in 1991 (*Johannessen et al.*, 2011) and in 2001 a calving event removing approximately 70-80 km^2 occurred (*Box and Decker*, 2011; *Johannessen et al.*, 2011). There was a further smaller calving event of about 31 km^2 in 2008 (*Box and Decker*, 2011; *Johannessen et al.*, 2011).

This history indicates that Petermann Glacier undergoes a cycle of large tabular calving events followed by a period of ice front advance. During these periods of advancement, there are small levels of calving along the margins of the ice shelf, due to the opening of crevasses caused by the velocity difference between the centre and margins of the ice shelf (*Higgins*, 1991). This results in a central tongue of

ice protruding from the ice shelf which can be seen in satellite imagery (Fig. 1.6. Observations from satellite imagery suggest that the majority of mass lost through calving occurs as large tabular bergs of the order 70 - 150 km^2 on a near decadal timescale (*Johannessen et al.*, 2011).

In August 2010 another large calving event occurred, which tied in with the near decadal time scale. This event, however, was distinguishable from the other known events for two reasons; firstly it was significantly larger then the previous calving events at about 270-290 km^2 (*Box and Decker*, 2011; *Johannessen et al.*, 2011) and secondly because the ice front retreated further than any previous observations (*Box and Decker*, 2011; *Falkner et al.*). This is not to say that the ice front has not retreated to this point previously. *Falkner et al.* argue that gaps in the observational record allow for scenarios where the ice front could have hypothetically retreated to a similar distance between 1880 and 1920 and between 1920 and 1940.

Box and Decker (2011) noted that there was a large rift upstream of the 2010 calving front and predicted a further calving event of approximately 150 km^2. In 2012 another large tabular berg of around 120 km^2 calved from the terminus of Petermann Glacier (*Münchow et al.*, 2014). Whether the short time span between these two large calving events is the beginning of a change in the stability of the ice shelf, or it is previously unrecorded natural variability is unknown. What is known is that these two large calving events have occurred over a much shorter time interval, and has resulted in the ice shelf terminus retreating further than previously recorded. The location of the ice front post calving events, and grounding line estimate, are shown in Figure 1.10.

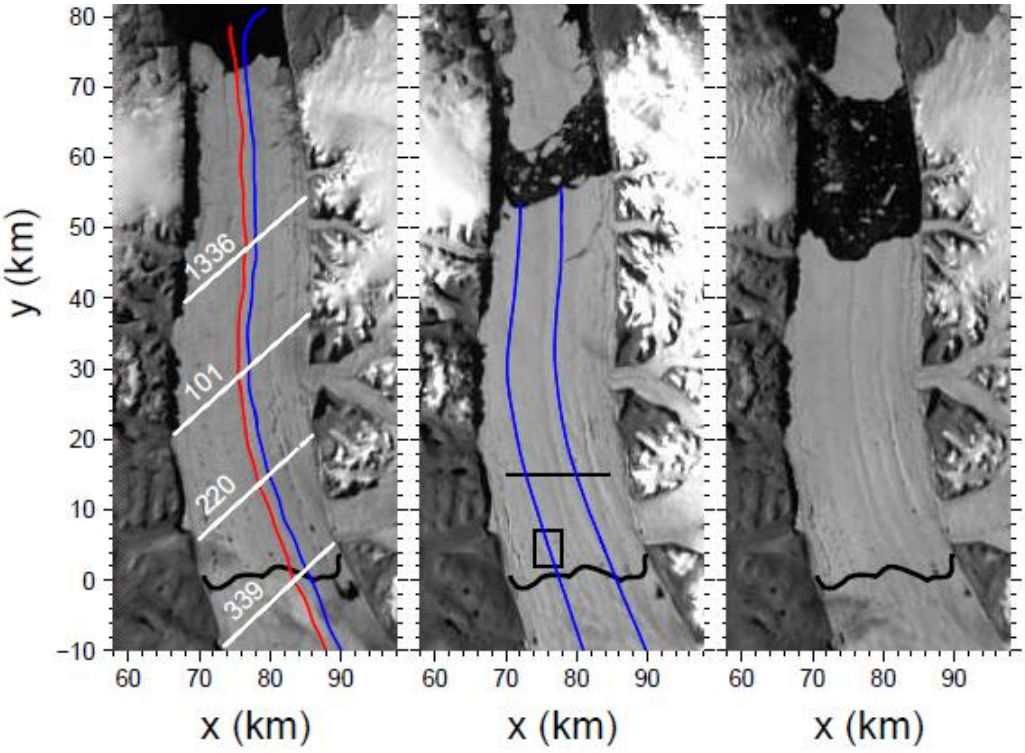

Figure 1.10: MODIS images of Petermann Glacier acquired a) in 2003 before major calving events, b) post 2010 calving event and c) post 2012 calving event. The thick black line near y = 0 km is the grounding line from *Rignot and Steffen* (2008) (Source: *Münchow et al.* (2014)).

Chapter 2

Topography of Petermann Glacier Ice Shelf and Fjord

2.1 Data

To be able to model the ice shelf cavity beneath the floating ice shelf of Petermann Glacier, the fjord bathymetry and ice shelf topography are required. However, due to it's remote location and the inherent difficulties with accessing sub-ice shelf cavities, it is difficult to directly map these. To combat this, the ice shelf topography is inferred from satellite imagery and airborne radar data, via the creation of a digital elevation model (DEM) of the ice surface topography, whilst the fjord bathymetry can be interpolated from the available swath bathymetry in the fjord and bedrock profile at the grounding line. The following sections introduce the data and methodology used to create the topography and bathymetry required to model Petermann Glacier.

2.1.1 Satellite images

The DEM of the ice shelf was created using images from two satellites; Landsat7 and Terra. The Landsat7 satellite provided imagery of the area from which a mask of

the ice shelf was created, whilst the Terra satellite's instrument ASTER (Advanced Spaceborne Thermal Emission and Reflection Radiometer) provided a DEM of the ice shelf and surrounding area.

Landsat7 was launched in April 1999 as part of the Landsat program which is jointly managed by NASA and the US Geological Survey. The Enhanced Thematic Mapper Plus (ETM+) is a satellite-mounted earth observing instrument, providing images of the Earth's surface. The ETM+ senses electromagnetic radiation in seven bands ranging from 0.45 to 12.50 μm with a resolution of 30 m and an eighth band (panchromatic) which measures radiation in the range 0.52 to 0.90 μm at a resolution of 15 m. Each image produced by the ETM+ is 183 km by 170 km in size and images are taken with a temporal resolution of 16 days. The mask of the area was created using Landsat 7 ETM+ images of Petermann Glacier and the surrounding area taken on 21st July 2001. The images used consisted of data from bands 1, 2 and 3 (blue, green and red respectively) and from band 8 (panchromatic) (*Landsat*, 2010).

The ASTER instrument is mounted aboard the Terra satellite, which is part of NASA's Earth Observing System. The DEM consists of a mosaic of overlapping tiles, arranged such that there are no inconsistent boundaries between tiles. Each tile is approximately 1 degree by 1 degree in size and consists of a smaller DEM which was calculated relative to the WGS84 ellipsoid, from a stereoscopic-pair of images of the same area taken with nadir (downwards) and backwards angles. Depending on the size and location of the area of interest, a DEM can consist of data from several different tiles.

It is possible to use a DEM to infer the topography of the base of an ice shelf since it is floating. This means that the assumption that the ice shelf is in hydrostatic equilibrium can be made which, means the ice draft can be calculated as a function of freeboard (ice thickness above the sea surface) and densities of the ocean and ice. This is explained further in Section 2.3.

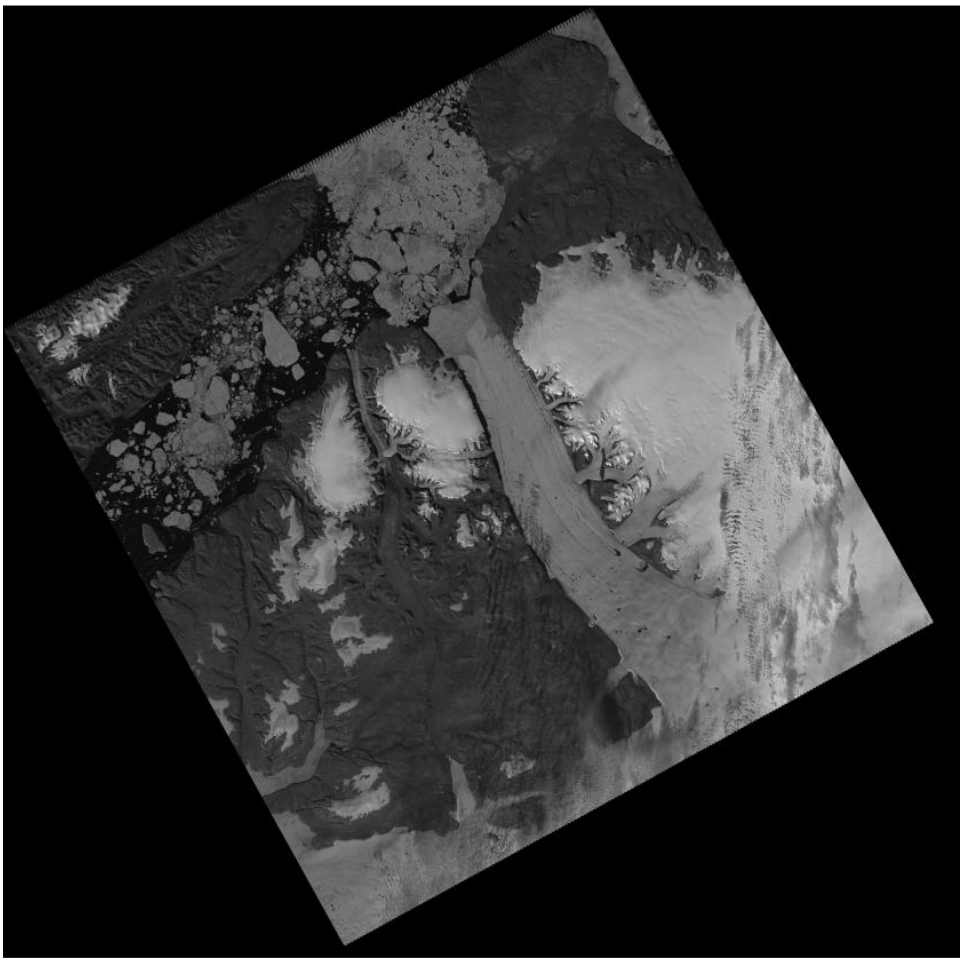

Figure 2.1: Landsat7 ETM+ panchromatic image of Peterman Glacier and the surrounding area.

DEMs over large areas such as the Greenland Ice Sheet are most commonly created from satellite-borne instruments as they are the only sensors to date that provide elevation data of sufficient coverage, accuracy and density for such large areas. DEMs created from stereoscopic imagery have a high level of precision yet low accuracy (between ±7 m and ±15 m (*Hirano et al.*, 2003)), therefore it is important to calibrate the Satellite data with airborne radar data to reduce these errors and obtain a more accurate DEM.

2.1.2 Radar data

The Centre for Remote Sensing of Ice Sheets (CReSIS), led from the University of Kansas, was formed with the aim of developing new technologies and models to predict and measure the response of sea level change to the mass balance of both the Greenland and Antarctic ice sheets (*CReSIS*, 2014). This involved collecting aerial radar measurements over the Greenland Ice Sheet and it's outlet glaciers. Measurements recorded included the elevation of the onboard radar relative to the WGS84 geoid, the time for the radar signal to return from the ice surface, time and location. The distance between the plane and ice surface is calculated using the speed of the radar signal in air.

Campaigns were flown over Petermann Glacier Ice Shelf in May 1999, May 2002 and May 2003 (Fig. 2.2). The 1999 campaign consisted of one flight line along the length of the ice shelf and one in the across shelf direction, over the grounded ice just upstream of the grounding line. The 2002 campaign consisted of 9 along shelf flight lines and the 2003 campaign consisted of two along shelf flight lines and three across shelf flight lines, two of which spanned the whole ice shelf and one which crossed the grounding line from grounded to floating ice halfway across the ice shelf.

The across shelf flight lines are all situated near to the grounding line and there are not any close to the ice shelf terminus. This is due to the high cliff faces of the fjord, which make it difficult for an aircraft to descend to the ice shelf and then ascend again before reaching the opposite fjord wall. Like wise the along shelf profiles are situated away from the fjord walls.

This means that the margins and downstream across shelf structure from the satellite imagery and radar data cannot be directly compared. The existing radar profiles will have to be relied upon to correct the satellite imagery to discover the ice shelf basal structure of these areas.

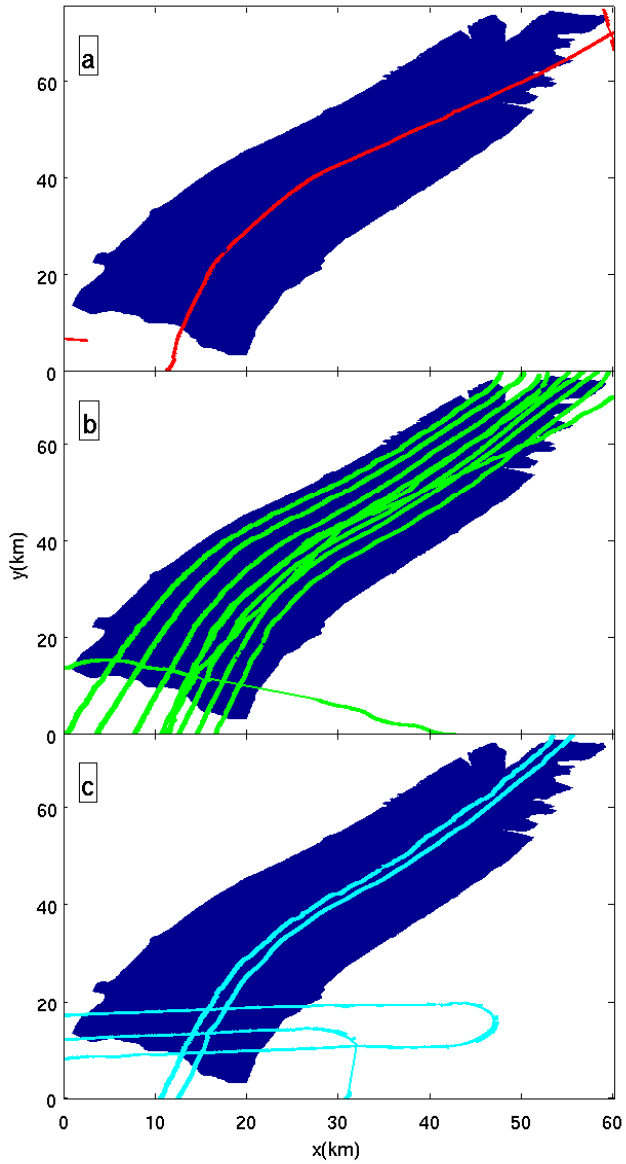

Figure 2.2: Locations of CReSIS radar flights over Petermann Glacier's ice shelf (blue area) in a) 1999, b) 2002 and c) 2003.

2.1.3 Grounding line

The grounding line, used to locate the change from the grounded ice to the floating ice of Petermann Glacier, was provided by Professor Eric Rignot and is the 1996 grounding line defined by *Rignot* (1998). Professor Rignot located the grounding line using satellite-radar interferometry, which is a technique using two radar interferograms spanning the same time interval. The interferograms were created using

data from the European Space Agency's Earth Remote Sensing Satellites (ERS-1 and ERS-2). The interferograms were first corrected for surface topography, using a digital elevation map of north Greenland (*Ekholm*, 1996), before being differenced to create a measure of tidal displacement of the glacier.

This difference interferogram highlighted the section of the glacier affected by tides (ice shelf), along with the areas which were not (grounded ice). *Rignot* (1998) defined the grounding line location as the point at which the glacier stopped being affected by the tide and, using this technique, could be located with a lateral precision of 30m. This technique relied on the assumption that the glacier creep remained constant during the observation period so that the displacement signal due to creep was cancelled out during the differencing process (*Rignot*, 1998).

Rignot (1998) found that the grounding line migrated back and forth on a short term basis (days to months), which was attributed to changes in ocean tides. A retreat of several hundred metres was identified between 1992 and 1996, this retreat was attributed to a change in the glacier thickness.

2.2 Methodology

2.2.1 Image processing

The first stage in creating the DEM of the ice shelf was to create a mask of the area to allow the differentiation between floating ice, ocean and land/grounded ice using the Landsat7 ETM+ imagery. ArcMap 9.3.1 was used to view the images, which were projected into the North Polar Stereographic (NPS) projection. This projection was applied as it preserves the relative areas of features. The location of the grounding line was overlain on top of the images, and the outline of the ice shelf, land/grounded ice and ocean were visually drawn. Once obtained the mask was saved on a 10 m resolution grid.

Landsat band 8 (Fig. 2.1) was predominantly used to create the mask due to its higher spatial resolution, allowing for a more detailed mapping of the area. The panchromatic band was, however, unable to easily differentiate between shadow and the bottom of the fjord cliffs and also between the front of the glacier and sea ice. Bands 1 to 3 were used to distinguish between these features, albeit at a slightly lower resolution (Fig. 2.3). Once created (Fig. 2.4), I applied the mask to the ASTER DEM of the whole area to create a DEM of the ice shelf.

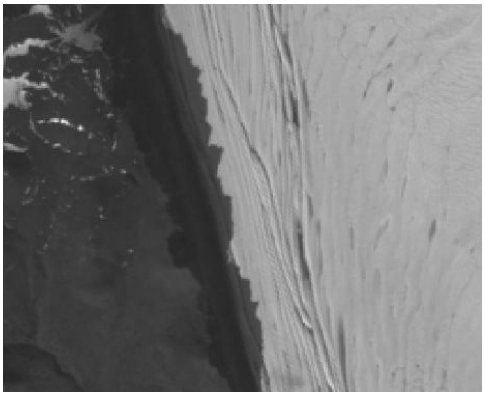

Figure 2.3: Landsat Band 1 image, focusing on a section of the western edge of Petermann Fjord. It is possible to distinguish between the shadow of the cliff and the edge of the Fjord using the imagery from this band.

The World Geodetic System 84 (WGS84) is an ellipsoid co-ordinate system used by satellites and to which their measurements are referenced. The raw ASTER DEM values are relative to WGS84. As the freeboard of a floating ice shelf is being considered, the DEM needs to be found relative to the geoid (the equipotential surface corresponding to a hypothetical motionless ocean) rather than to WGS84. Therefore I subtracted geoid-ellipsoid differences, obtained from the International Centre for Global Earth Models (*ICGEM*, 2014), from the ASTER DEM after the mask was applied, resulting in a DEM of Petermann Glacier's ice shelf (Fig. 2.5).

An area of ice shelf height of 0 m can be seen at the ice front. This is most likely caused due by calving events changing the ice front position between the Landsat and ASTER images being collected. This issue is addressed in Section 2.4.2.

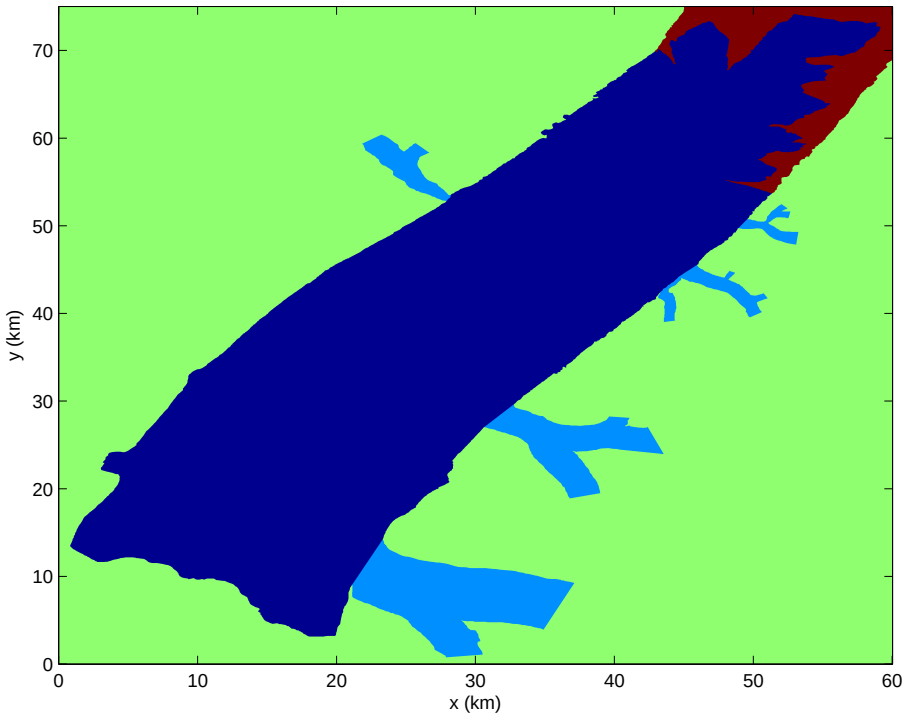

Figure 2.4: Landsat7 mask of Petermann Glacier ice shelf in polar stereographic projection. The ice shelf flows from bottom left to top right. Dark Blue represents the ice shelf, light blue represents tributary glaciers, green represents land or grounded ice and red represents water or sea ice .

2.2.2 Radar data correction

The Satellite data needed to be calibrated with airborne radar data to correct for any error in elevation due to the angle between the satellite and the Earth. To be able to do this the location of the radar data first needed to be converted into NPS projection. This was done using equations (2.1) to (2.5):

$$x = \rho \sin(\lambda - C_m), \tag{2.1}$$

$$y = -\rho \cos(\lambda - C_m), \tag{2.2}$$

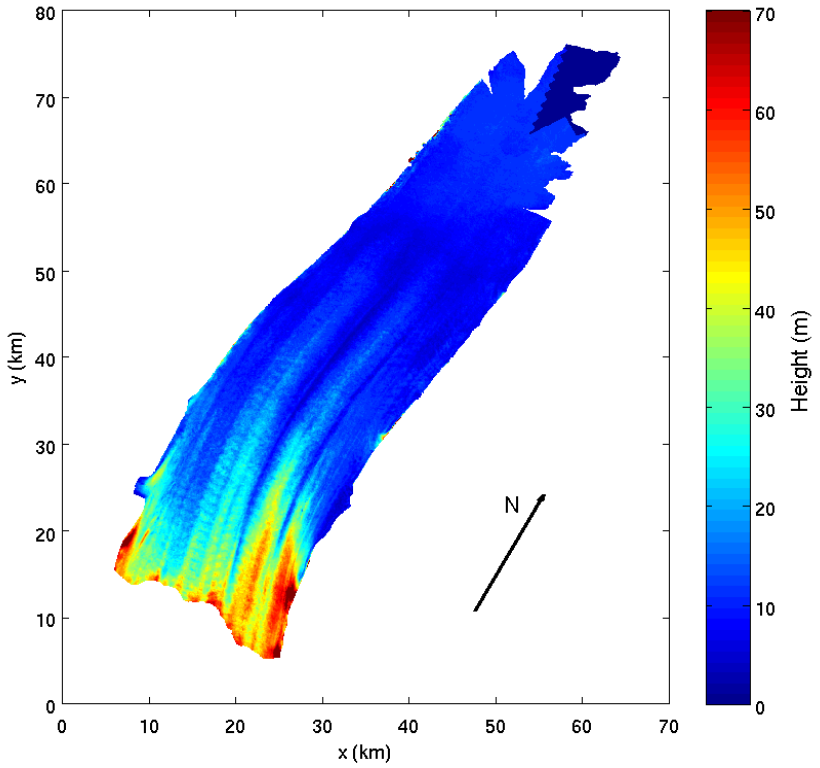

Figure 2.5: ASTER DEM of Petermann Glacier's ice shelf, corrected for the Geoid, in polar stereographic projection.

$$\rho = \frac{2at}{[(1+e)^{(1+e)}(1-e)^{(1-e)}]^{1/2}}, \tag{2.3}$$

$$t = \frac{\tan(\pi/4 - \phi/2)}{[(1 - e\sin\phi)(1 + e\sin\phi)]^{e/2}}, \tag{2.4}$$

$$e^2 = 2f - f^2, \tag{2.5}$$

where C_m is the central meridian for the projection, (ϕ,λ) is the latitude and longitude of the point to be projected, f is the flattening of the ellipsoid and a is the semi-major axis.

Due to the onboard radar's elevation being relative to the WGS84 ellipsoid, this needed to be corrected for before any calibrations could take place. The corrections

were made using the same Geoid corrections as used for the ASTER DEM correction. The Landsat7 mask was then applied to the radar data to extract the corrected surface elevation measurements for use in calibrating the ASTER DEM.

2.2.3 Calibration

Due to the orbit of the Terra satellite, ASTER imagery is taken from an oblique angle. This results in a dataset with high relative precision but poor accuracy. There is a 2-D field of bias in the DEM. To counteract this bias and the problems discussed in Section 2.1.1, the DEM is calibrated using airbourne radar data.

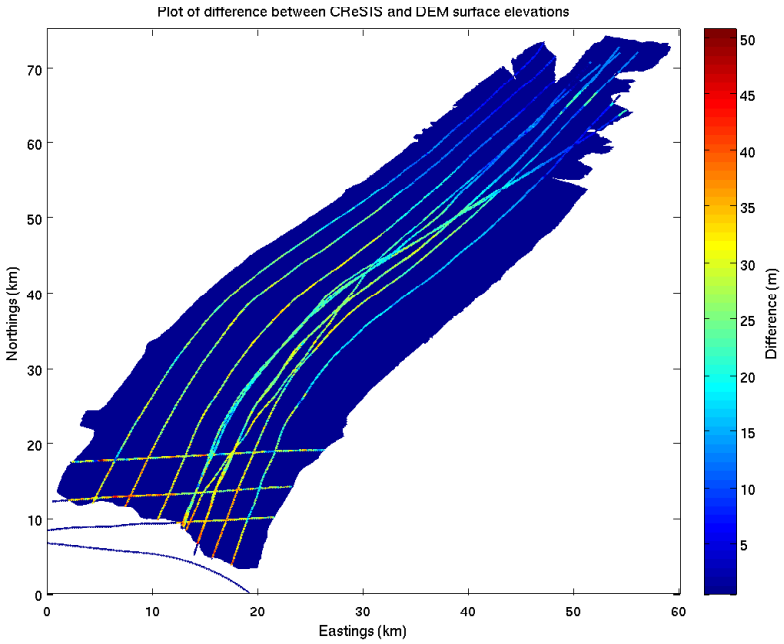

Figure 2.6: Difference between CReSIS and ASTER DEM elevations.

To investigate the relationship in differences between DEM and Radar surface elevations, the spatial pattern of differences was plotted (Fig. 2.6). The figure shows that as you move downstream of the grounding line, there is a decreasing trend (red to green) in elevation differences. This decreasing trend continues until a northing of approximately 54 km, after which point the differences become more consistent before beginning to increase again near the ice front.

To be able to observe the change in trend more easily, the differences were re-plotted with the colour scale readjusted to focus on the shallower elevations near the ice front (Fig. 2.7). This figure shows that north of 54 km near to the margins, the differences become relatively consistent at approximately 8 m, whilst in the centre of the ice shelf the differences increase again to the order of 15 m.

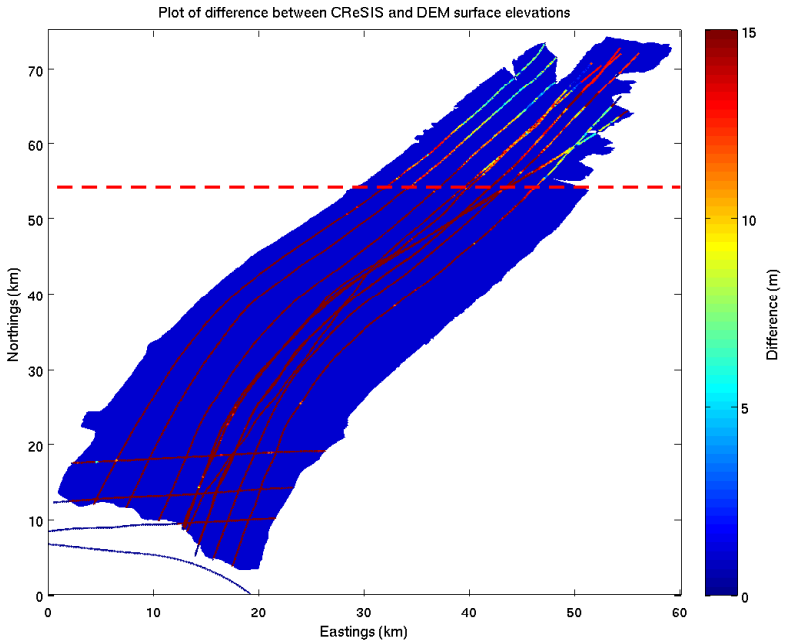

Figure 2.7: Difference between CReSIS and ASTER DEM elevations with a focused colour scale to show increasing pattern at ice front. Dashed red-line indicates 54 km North.

This change in the pattern of differences is most likely caused by the dynamic nature of an ice front. Having a shallow draft, the ice front it susceptible to both tidal flexing and calving, meaning that the ice shelf could have different elevations between two measurements collected at different times. This is supported by the area of ice shelf with an elevation of 0 m near to the ice front (Fig. 2.5). Further upstream from the ice front where the ice shelf is thicker, tidal flexing is of a smaller amplitude, and the risk of calving is significantly lower, therefore resulting in more reliable elevation measurements.

Therefore, due to the dynamic nature of the ice front, and the potential incon-

sistencies between measurements, only elevations southwards of 54 km north were included in the calibration. The calibration took the form of a linear fit through the data, with a gradient of 1.1922 and an intercept of 23.9133 m. The error in the calibration was calculated using the method of Root Mean Square Error and was calculated as 6.61 (Fig. 2.8).

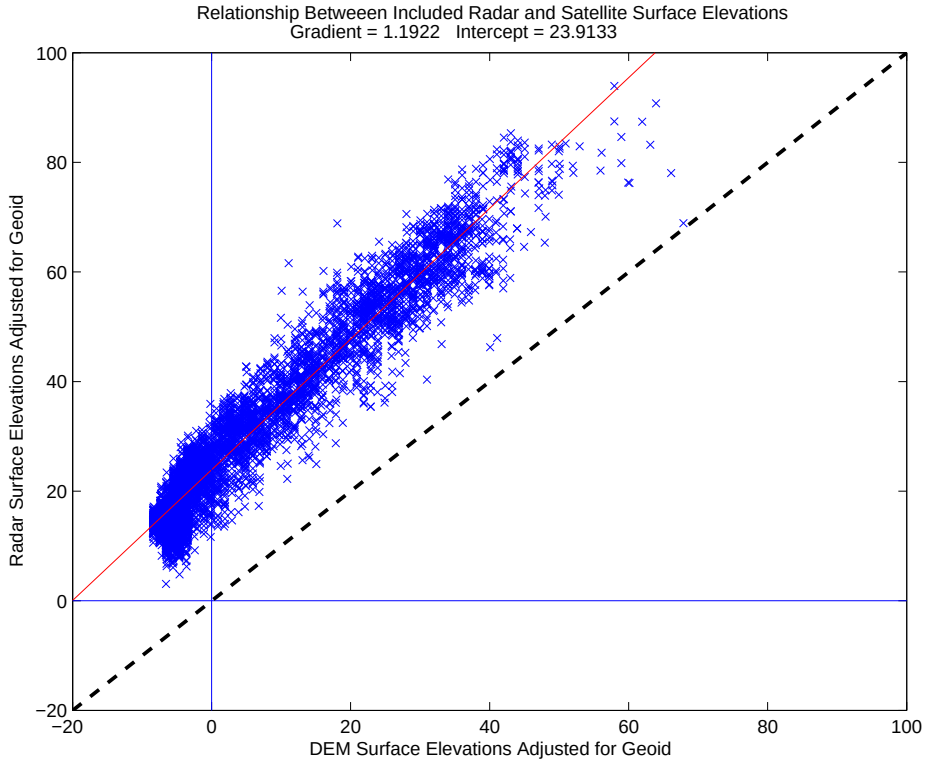

Figure 2.8: Relationship between ASTER surface elevations and radar surface elevations south of 54 km North (red line). Black dashed line represents a one to one relationship.

Figure 2.9 shows the elevation map of the ice shelf after it has been calibrated with the airborne radar data. The data near the ice front are still included in this figure and are discussed when creating the realistic model domain in Section 2.4.2 after the DEM has been converted to ice draft.

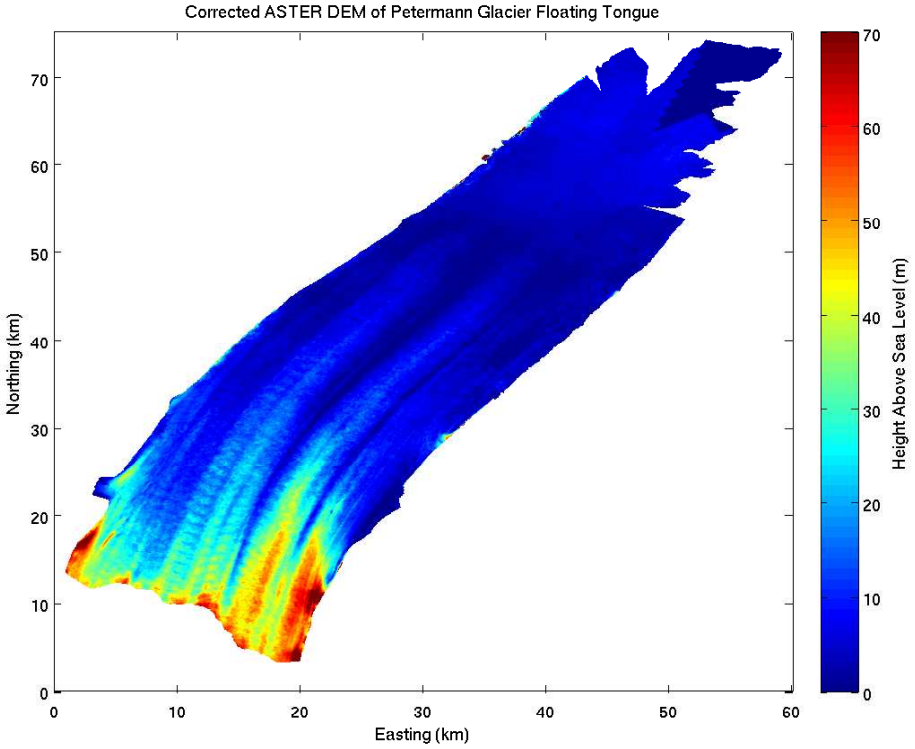

Figure 2.9: Calibrated ASTER DEM.

2.3 Corrected Ice Draft Map

To convert the DEM into a map of the draft of Petermann Glacier's ice shelf, the assumption of hydrostatic equilibrium was made. This means that the ice is assumed to be floating and not supported by either the grounded portion of the glacier or the vertical cliffs of the fjord walls. This assumption is valid for the majority of the ice shelf; however, in areas of small scale gradients in ice thickness, 'bridging stresses' will prevent the ice from floating in equilibrium. However within a distance of several ice thicknesses from the grounding line, the assumption is typically not valid. This is due to a number of factors including ice rheology, dynamics and bedrock topography (*Griggs and Bamber*, 2011). Although the assumption is not valid close to the grounding line, confidence is gained in the resultant ice draft map due to the continuation of ice shelf features upstream from the grounding line, into a portion of the ice shelf where the assumption of hydrostatic equilibrium is valid.

Using the assumption of hydrostatic equilibrium, the draft of the ice shelf can be calculated (depth of submerged ice) using Archimedes' principle, which states that the mass of water displaced by the ice is equal to the mass of the ice displacing it. As ice is less dense then seawater, we know that the volume of water displaced is less than the volume of ice doing the displacement, resulting in floating ice. Figure 2.10 shows a schematic of floating ice and defines the dimensions used to calculate ice draft (Eqns. 2.6 to 2.8).

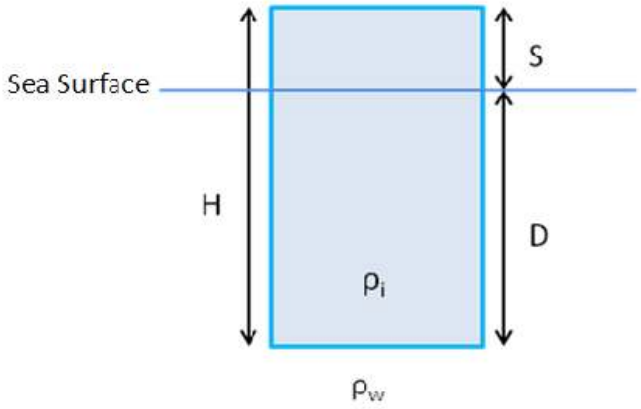

Figure 2.10: Schematic showing ice in hydrostatic balance. H is height of ice column, S is surface elevation, D is ice draft ρ_w is the density of water and ρ_i is the density of ice.

$$D\rho_w = H\rho_i \tag{2.6}$$

and

$$H = D + S, \tag{2.7}$$

$\Rightarrow$

$$D = S\left(\frac{\rho_i}{\rho_w - \rho_i}\right). \tag{2.8}$$

In converting ice surface elevations to ice draft the values of 1028 kg/m for ρ_w and 918 kg/m for ρ_i were used. Figure 2.11 shows the corrected ice draft map for

Petermann Glacier's ice shelf. The prominent basal channels are clearly seen evolving near the grounding line, before widening and reducing in amplitude.

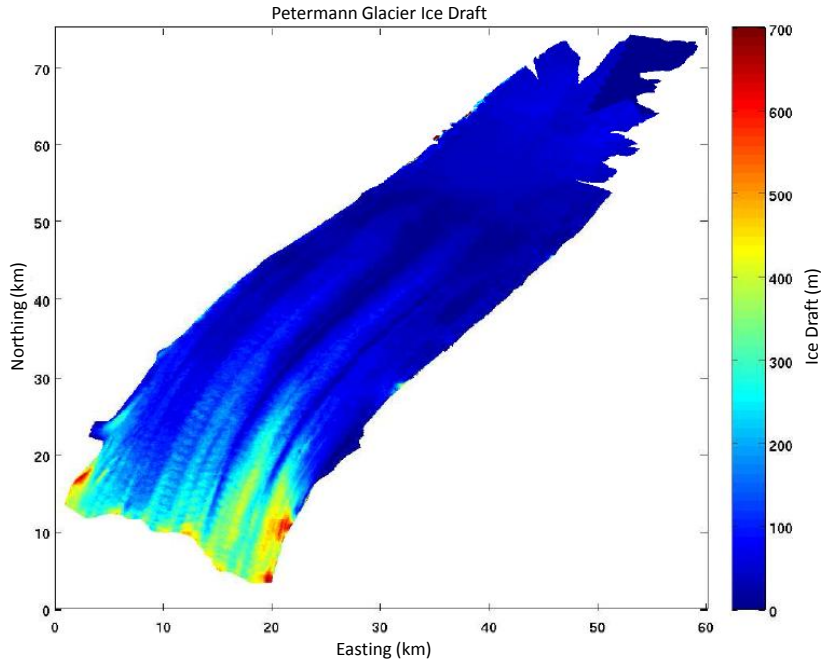

Figure 2.11: Ice draft map of Petermann Glacier's ice shelf assuming it is floating in hydrostatic equilibrium.

2.4 Model Domain

2.4.1 Idealised Representation

The MITgcm is used to model the circulation in the ocean cavity beneath an idealised version of Petermann Glacier with ice shelf topography based on the final ice draft map (Fig 2.11). The model is a north-south orientated rectangle, 100 km long, 20 km wide and 900 m deep, with a horizontal resolution of 250 m and a vertical resolution of 10 m. Free-slip walls on the southern, eastern and western edges of the domain represent the glacier's grounding line and the fjord walls respectively. Free slip boundary conditions were used as, given the model horizontal resolution, it was

not expected to be able to resolve the boundary layer at the edge of the domain.

The ice shelf extends 70 km from the southern boundary, spans the width of the domain, and thins from a draft of 600 m at the grounding line to 60 m at the ice front,roughly in accordance with observational data from Petermann Fjord (*Rignot and Steffen*, 2008) (Fig. 2.12). Channels which run north-south and are sinusoidal in the cross-shelf direction are introduced across the entire width of the ice shelf base.

The ice draft under the channel crests thins quadratically at first in the along-stream direction, before thinning linearly to the ice front (Eqn. (2.9)). This profile was chosen to approximately reproduce the features seen in the ice draft map and in *Rignot and Steffen* (2008). We will run test cases with a variable number of channels, ranging from no channels to 8 channels.

The along-shelf shape of the channel keels is based on a tangent function (Eqn. (2.10)). For a case of no basal channels, the ice profile is taken as the across shelf mean profile of the channel cases, ensuring that the mean ice draft is consistent for all model runs. The domain size remains fixed for each configuration of channel number, implying a decrease in channel width and an increase in the steepness of channel slopes as the number of channels increases. The ice base is given by:

$$d_c = \begin{cases} ay^2 + by + c & \text{if } y \leq 20km, \\ -116 + (y \times \frac{4}{5}) & \text{if } y > 20km, \end{cases} \tag{2.9}$$

$$d_k = k_a \times \arctan(k_b \times (y - k_c)) - k_d, \tag{2.10}$$

where d_c is the channel crest draft (m), d_k is the channel keel draft (m), y is distance from southern boundary (km), a = -1.21, b = 49.2, c = -600, k_a = 229.8041, k_b = 0.09, k_c = 15 and k_d = 375.164. Figure 2.12 shows the ice geometry of the four channel configuration.

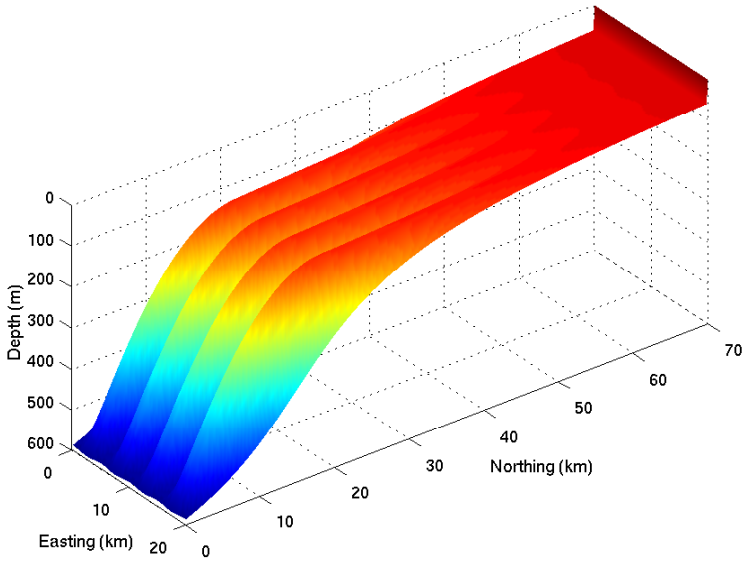

Figure 2.12: Ice shelf geometry for the idealised four channel configuration.

2.4.2 Realistic Domain

Chapter 6 shows results from modelling the circulation in the cavity beneath an ice shelf with realistic Petermann Glacier topography. The domain is a north-south orientated rectangle, 110 km long and 30 km wide. The bathymetry and ice shelf draft data are in a north polar stereographic projection, which has been rotated so that the ice shelf is aligned with the long dimension of the domain.

2.4.2.1 Ice Draft

The ice draft map used in the realistic domain is based upon the pre-calving, calibrated draft (Fig 2.11). The 'rough' ice topography can lead to sharp gradients when represented on a cartesian z-grid, as well as the possibility of individual ocean cells protruding up into the ice base, with the four surrounding cells being ice. This will not allow for any melting in the model as no flow will be possible in this cell. To

combat these problems some manipulation to the ice draft map was required.

The data was first interpolated onto a 10 m by 10 m grid to allow for the data to be easily 'binned' onto the lower resolution (250 m by 250 m) model grid. Data is 'binned' onto a coarser grid by taking an average of all the data from the finer grid that will be represented by one point on the coarser model grid. So in this case each point on the model domain is an average of 25 by 25 data points of the interpolated data. The interpolation was necessary so that the resolution of the model grid could be altered easily if needed. Once the data was 'binned' the ice shelf topography was still relatively rough, although the finer resolution perturbations had been removed. To combat the remaining steps in the ice draft map, it was smoothed using a discretised spline smoothing function with the influence of outlying data minimised.

Due to the sharp edges and unreliable DEM mosaic tiles near the ice front, the ice shelf was cropped at 66.75 km north of the grounding line. This left a thickening of the ice shelf at the ice front which was not thought to be realistic and a relic of unreliable DEM tiles. To remove this thickening, the ice draft at 51.5 km was simply extended to the ice front. This prevented ice shelf thickening, however it also extended the channels present at this point to the ice front.

Channels are not believed to extend to the ice front at Petermann Glacier, however in extending this draft profile to the ice front, the potential for pooling of meltwater behind thicker ice in the model, which could prevent realistic model results, is prevented. The extension of channels to the ice front is not expected to have a significant effect on basal melting, water mass transformation or flow patterns as it is shallow and not in contact with the deeper 'warm' water. Figure 2.13 shows the final realistic ice shelf topography.

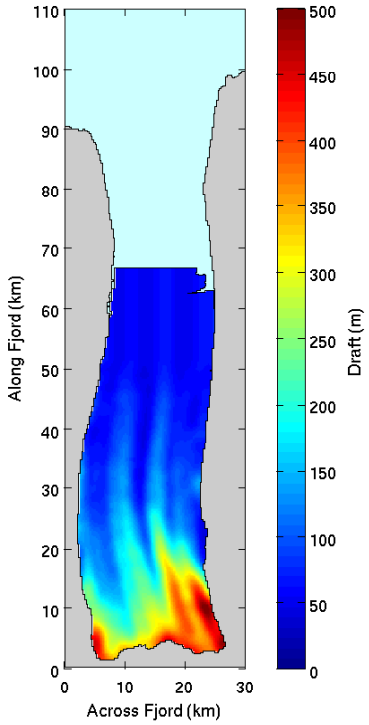

Figure 2.13: Ice shelf topography for the realistic Petermann Glacier domain.

2.4.2.2 Bathymetry

Due to its remote location and ice shelf covering a large portion of the fjord, detailed measurements of the fjord bathymetry are limited. The International Bathymetric Chart of the Arctic Ocean (IBCAO) (*Jakobsson et al.*, 2012) has an accurate coastline of the fjord mouth and Hall Basin, however its coverage of the fjord's bathymetry is limited. Therefore the IBCAO data set was used to create the coastline only and depth data from within the fjord was not incorporated.

Bathymetry data was collected during three research cruises to the area. Two of these cruises were conducted before the calving events of 2010 and 2012 aboard the USCGC Healy in 2003 and the CCGS Henry Larsen in 2009. These data were used by *Johnson et al.* (2011) in producing their bathymetry map of Hall Basin and the mouth of Petermann Fjord. The third research cruise aboard the CCGS Henry

Larsen in 2012 was after these calving events, allowing the vessel to enter further into the fjord. This research cruise provides bathymetry data for underneath the pre-calving ice shelf used in the realistic domain.

These data show the presence of a shallow sill as noted by *Johnson et al.* (2011) with a deep basin inshore of the sill. Further to *Johnson et al.* (2011) the data show that the basin is on the north-eastern side of the fjord, whilst there is a shelf at a shallower depth on the south-western side. We do not know the extent to which the deep basin protrudes underneath the ice shelf, however we do know the thickness of the ice at the grounding line, from the DEM, and the bedrock follows the profile of the ice draft at this location. There is also an indication of a shelf in the south-western side in the grounding line depths, however the contrast with the depths on the north-eastern side of the fjord is less extreme.

Although the bathymetry in the fjord mouth and at the grounding line is known, it is not known how the bathymetry is behaving underneath the ice shelf. Therefore I combined the data in three different ways to investigate the effect of bathymetry on the circulation and ice-ocean interactions with the fjord.

To allow the construction of these different bathymetries, bathymetry data was first interpolated onto a 10 m grid before being 'binned', using the same method a for the ice shelf topography, onto the model grid. The data was then interpolated between the data sets to create the following three bathymetry scenarios.

1. The deep basin shallows quickly to the grounding line depth and then remains at this depth for majority of the fjord.

2. Bathymetry shallows linearly between the cruise data and grounding line.

3. The deep basin protrudes close to the grounding line, at which point the bathymetry shallows steeply to the grounding line depth.

To create the first scenario, the grounding line profile was added close to the cruise

data before interpolation took place, the second scenario was created by linearly interpolating the cruise and grounding line data, whilst the third scenario was created by adding an across fjord profile which bisected the deep basin, close to the grounding line before interpolating. All three of these scenarios were smoothed using the same technique as used for the ice shelf topography. After smoothing, bedrock was removed wherever necessary to ensure that there was at least 10 m of ocean underneath the whole ice shelf. 10 m was chosen as this is the vertical resolution of the model and the distance which ice-ocean interaction processes occur over (See Chapter 3). Figure 2.14 shows the three different bathymetry scenarios.

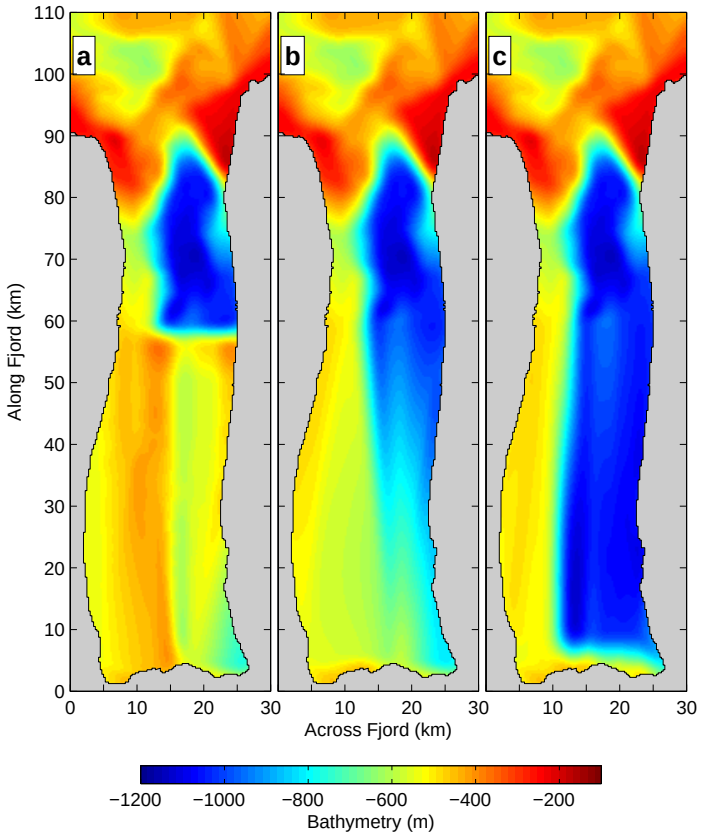

Figure 2.14: Realistic bathymetry scenarios with a) small basin, b) linear shallowing and c) large basin.

It should be noted that of the three scenarios, the linearly sloping bathymetry looks the most geophysically realistic. However even this scenario has some poten-

tially unrealistic features. It is possible that there are undulations on the seabed with the potential for across fjord ridges or further basins. However as the geology underneath the ice shelf is unknown, these scenarios were chosen by interpolating known data without the addition of other potential features.

Chapter 3

Modelling Ice-Ocean Interaction

3.1 Dominant momentum balance

To be able to understand the flow of a layer of meltwater beneath an ice shelf, an understanding of its momentum balance is required. To do this we consider the depth integrated Boussinesq Navier-Stokes equations of *Jungclaus and Backhaus* (1994), as applied by *Holland and Feltham* (2006). Figure 3.1 shows a layer of meltwater beneath an ice shelf with the relevant coordinates used in the depth integrated equations 3.1 and 3.2.

$$\begin{aligned}\frac{\delta(DU)}{\delta t}+\frac{\delta(DUU)}{\delta x}+\frac{\delta(DVU)}{\delta y} =&\frac{\delta}{\delta x}\Big(A_h D\frac{\delta U}{\delta x}\Big)+\frac{\delta}{\delta y}\Big(A_h D\frac{\delta U}{\delta y}\Big)+\frac{gD^2}{2\rho_o}\frac{\delta\rho_a}{\delta x}\\ &+g'D\frac{\delta A}{\delta x}-c_d(U^2+V^2)^{\frac{1}{2}}U+DfV,\end{aligned} \tag{3.1}$$

$$\begin{aligned}\frac{\delta(DV)}{\delta t}+\frac{\delta(DUV)}{\delta x}+\frac{\delta(DVV)}{\delta y} =&\frac{\delta}{\delta x}\Big(A_h D\frac{\delta V}{\delta x}\Big)+\frac{\delta}{\delta y}\Big(A_h D\frac{\delta V}{\delta y}\Big)+\frac{gD^2}{2\rho_o}\frac{\delta\rho_a}{\delta y}\\ &+g'D\frac{\delta A}{\delta y}-c_d(U^2+V^2)^{\frac{1}{2}}U-DfU,\end{aligned} \tag{3.2}$$

where D is the meltwater layer depth, U is depth integrated u-velocity, V is depth integrated v-velocity, A is the depth of the meltwater layer base, g' is the reduced gravity, g is the gravitational constant, c_d is the drag coefficient between the meltwater layer and base of the ice shelf, ρ_a is the plume density, ρ_o is a reference density, A_h is the eddy viscosity for momentum and f is the coriolis parameter.

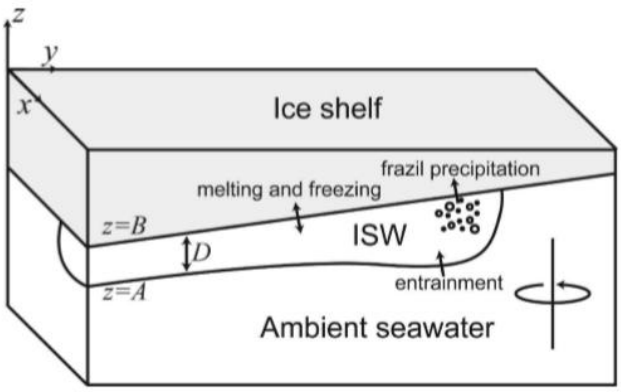

Figure 3.1: Schematic of a layer of meltwater (ISW) between a floating ice shelf and ambient seawater. Relevant processes (melting, freezing and entrainment) along with coordinates used in equations 3.1 and 3.2 are shown (Source: *Holland and Feltham* (2006)).

A scaling analysis was performed to find the relative importance of each term in equations (3.1) and (3.2).The following values were used in the scale analysis; $t = 1.5552\times10^{8}$ s, D =15 m, $U/V = 0.5$ m/s, $\delta x = 2500$ m, $\delta A = 300$ m, $g' = 2.8628\times10^{-2}$ m/s^{2}, $c_d = 1.5\times10^{-3}$, $f = 1.4301\times10^{-4}$ s^{-1}, $A_h = 15$ m^{2}s^{-1}, $g = 9.81$m/s^{2}, $\rho_o = 1028$ kg m^{-3} and $\frac{\delta\rho_a}{\delta x}$ =1×10^{-4} kg m^{-4}. These values represent either model parameters, model geometry, or scales representative of scales representative of model runs.

These values gave the following scales for the terms in order; 4.82×10^{-8}, 1.50×10^{-3}, 1.50×10^{-3}, 1.80×10^{-5}, 1.80×10^{-5}, 1.07×10^{-4}, 1.43×10^{-3}, 5.30×10^{-4} and 1.07×10^{-3}. The buoyancy term is dependent on the slope of the ice shelf, however a sensitivity analysis of basal slope found the buoyancy term to be important for basal gradients as low as 20% of the value used in this scaling analysis. The effect of the value of the viscosity parameter was investigated and found to need a 70 fold increase before it

affected the scaling analysis. Reducing equations (3.1) and (3.2) to dominant terms (scales of the order $\times 10^{-3}$) results in:

$$\frac{\delta(DUU)}{\delta x} + \frac{\delta(DVU)}{\delta x} = g'D\frac{\delta A}{\delta x} + DfV, \tag{3.3}$$

$$\frac{\delta(DVV)}{\delta y} + \frac{\delta(DUV)}{\delta y} = g'D\frac{\delta A}{\delta y} - DfU, \tag{3.4}$$

Whether the buoyancy term (3rd term) is balanced by the inertial (1st and 2nd terms) or rotational (4th term) terms is dependent on their relative sizes. If the inertial term is much bigger than the rotation term then the balance is between buoyancy and inertia.

$$\frac{\delta(DUU)}{\delta x} + \frac{\delta(DVU)}{\delta x} = g'D\frac{\delta A}{\delta x}, \tag{3.5}$$

$$\frac{\delta(DVV)}{\delta y} + \frac{\delta(DUV)}{\delta y} = g'D\frac{\delta A}{\delta y}, \tag{3.6}$$

If the rotational term is much larger than the inertial term then the balance is geostrophic between buoyancy and rotation.

$$g'D\frac{\delta A}{\delta x} = -DfV, \tag{3.7}$$

$$g'D\frac{\delta A}{\delta y} = DfU, \tag{3.8}$$

If the two terms are of the same relative importance then the balance remains that in equations (3.3) and (3.4). The conditions that define which balance is involved can be found by considering the ratio of scales between the inertial and rotational

terms. Inertial terms dominate rotational terms when:

$$\frac{\frac{D_* U_*^2}{\Delta x}}{D_* U_* f} \gg 1, \tag{3.9}$$

or

$$\Delta x \ll \frac{U_*}{f}, \tag{3.10}$$

where D_* is the meltwater layer depth scale, U_* is the velocity scale and Δx is a horizontal length scale. If the horizontal length scale is much smaller than $\frac{U_*}{f}$ then the flow will be inertial, if they are approximately even then both inertial and rotational terms are important, whilst if the horizontal length scale is much larger than $\frac{U_*}{f}$ then the flow will be geostrophic. This length scale is different from the traditional Rossby radius.

$$L_R = \frac{(g'D)^{\frac{1}{2}}}{|f|} \tag{3.11}$$

The two scale are equal when the plume is 'critical', that is the meltwater layer travels at its gravity-wave speed ($U_* = (g'D)^{\frac{1}{2}}$).

3.2 Ice-ocean thermodynamics

Both melting and freezing at the base of an ice shelf are affected by, and impact on, the sub-ice shelf circulation and the resultant modification of water masses (*Hellmer and Olbers*, 1989). The fluxes of both heat and salt across the ice-ocean boundary layer are an important driver in the sub-cavity circulation, as described in section 1.3.1. To be able to predict and model these interactions at the base of an ice shelf we need to be able to describe these fluxes and their impacts mathematically.

Figure 3.2, redrawn from *Holland and Jenkins* (1999), shows a schematic representation of the a) heat and b) salt fluxes at the base of an ice shelf. The total oceanic heat flux towards the ice-ocean interface (Q_M^T) is balanced by the latent heat

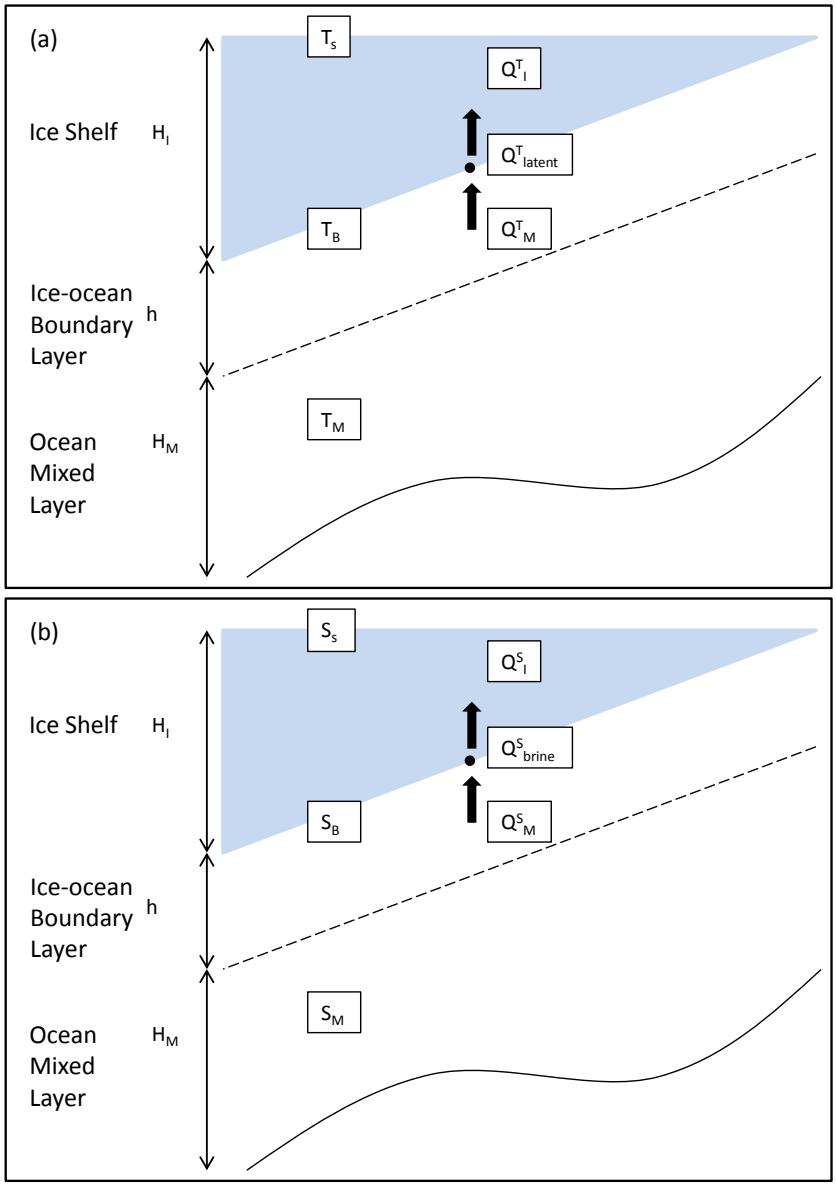

Figure 3.2: Schematic of a) heat and b) salt balance at the base of an ice shelf (Redrawn from: *Holland and Jenkins* (1999)).

consumed during melting or released during freezing (Q^T_{latent}) and the molecular heat conduction through the ice (Q^T_I):

$$Q^T_M = Q^T_{latent} + Q^T_I, \tag{3.12}$$

The individual terms can be expressed as:

$$Q_M^T = \rho_O c_O \gamma_T (T_B - T_M) \tag{3.13}$$

$$Q_{latent}^T = m \rho_I L \tag{3.14}$$

$$Q_I^T = \rho_I c_I \kappa_I \frac{T_S - T_B}{H_I} \tag{3.15}$$

where m is the basal melt rate; $c_o = 3994$ Jkg^{-1} °C^{-1} and $c_I = 2000$ Jkg^{-1} °C^{-1} are the specific heat capacity of water and ice respectively; $L = 3.34 \times 10^5$ Jkg^{-1} is the latent heat of ice fusion; ρ_O is the density of the boundary layer; $\rho_I = 917$ kgm^{-3} is the density of the ice shelf; $\kappa_I = 1.541 \times 10^{-6}$ m^{2}s^{-1} is the molecular thermal conductivity of the ice shelf; H_I is the ice shelf thickness; T_M is the temperature of the mixed layer; T_B is the temperature at the ice-ocean interface; $T_S = -20$ °C is the far-field internal temperature of the ice shelf and γ_T is the thermal exchange velocity. Substituting equations (3.13) to (3.15) into equation (3.12) we get:

$$\rho_O c_O \gamma_T (T_B - T_M) = m \rho_I L + \rho_I c_I \kappa_I \left(\frac{T_S - T_B}{H_I} \right) \tag{3.16}$$

As there is no diffusive flux of salt into the ice shelf (Q_I^S) (*Holland and Jenkins*, 1999), it is neglected from the salt balance. The total oceanic salt flux towards the ice-ocean interface (Q_M^S) is therefore balanced by the freshwater or salt flux due to melting or freezing respectively at the interface (Q_{brine}^S):

$$Q_M^S = Q_{brine}^S \tag{3.17}$$

The individual terms can be expressed as:

$$Q_M^S = \rho_O \gamma_S (S_B - S_M) \tag{3.18}$$

$$Q_{brine}^S = m \rho_I S_B \tag{3.19}$$

where γ_S is the haline exchange velocity, S_B is the salinity at the ice-ocean interface and S_M is the salinity of the mixed layer. Substituting equations (3.18) and (3.19) into equation (3.17) we get:

$$\rho_O \gamma_S (S_B - S_M) = m \rho_I S_B \tag{3.20}$$

The ice-ocean interface is at the in-situ freezing point (T_F) which can be expressed as a function of the interface salinity and pressure (p).

$$T_F = a S_B + b + cp, \tag{3.21}$$

where $a = -0.0575\,^{\circ}\mathrm{Cpsu}^{-1}$, $b = 0.0901\,^{\circ}\mathrm{C}$ and $c = -7.61 \times 10^{-4}\,^{\circ}\mathrm{CPa}^{-1}$.

Equations (3.16), (3.20) and (3.21) can be solved for S_B and hence the melt rate, m, in terms of T_S, T_M and S_M.

There are several different approaches which have been used to mathematically describe the thermal and haline exchange velocities $\gamma_{T/S}$. The simplest of these is to choose a constant value for each exchange velocity, which is an approach followed by *Hellmer and Olbers* (1989). However the exchange of both heat and salt across the boundary layer is due to the turbulence within the layer, therefore it is more realistic to make the exchange velocities functions of the friction velocity u_*:

$$u_*^2 = c_d (u_m^2 + v_m^2), \tag{3.22}$$

where $c_d = 1.5 \times 10^{-3}$ is a drag coefficient, and u_m and v_m are the mixed layer velocity components. This approach was initially developed for sea-ice study and was adapted for ice shelf-ocean interaction by *Jenkins* (1991). The exchange velocities were parameterised as:

$$\gamma_T = \frac{u_*}{2.12\ln\left(u_* h/\nu\right) + 12.5\mathrm{Pr}^{2/3} - 9}, \tag{3.23}$$

$$\gamma_S = \frac{u_*}{2.12\ln\left(u_* h/\nu\right) + 12.5\mathrm{Sc}^{2/3} - 9}, \tag{3.24}$$

where Pr is the molecular Prandtl number (ratio of viscosity to thermal diffusivity); Sc is the molecular Schmidt number (ratio of viscosity to haline diffusivity); ν is the kinematic viscosity of seawater and h is the thickness of the boundary layer.

Holland and Jenkins (1999) went further by considering the buoyancy flux at the ice-ocean interface and its impact on turbulence within the boundary layer. Melting of ice at the interface is a stabilizing buoyancy flux and will suppress mixing, whilst freezing of ocean water is a destabilizing buoyancy flux and will enhance mixing. *Holland and Jenkins* (1999) parameterized the exchange velocities after *McPhee et al.* (1987) as:

$$\gamma_{T,S} = \frac{u_*}{\Gamma_{turb} + \Gamma_{mole}^{T,S}} \tag{3.25}$$

where

$$\Gamma_{turb} = \frac{1}{\kappa}\left(\frac{u_*^2 \xi_N \eta_*^2}{|5f\nu|}\right) + \frac{1}{(2\xi_N \eta_*)} - \frac{1}{\kappa} \tag{3.26}$$

and

$$\Gamma_{Mole}^{T,S} = 12.5(\mathrm{Pr}, \mathrm{Sc})^{2/3} - 6 \tag{3.27}$$

In these parameterisations Γ_{turb} is the turbulent transfer parameter and $\Gamma_{mole}^{T,S}$ is the thermal/haline molecular transfer parameter; $\kappa = 0.4$ is von Kármán's constant, $\xi_N = 0.052$ is a stability constant, $\eta_* = 1$ is a stability parameter, f is the Coriolis

parameter, $\nu = 1.95 \times 10^{-6} \mathrm{m}^2\mathrm{s}^{-1}$, Pr = 13.8 and Sc = 2432.

3.3 The MITgcm

The Massachusetts Institute of Technology general circulation model (MITgcm) is a finite-volume, incompressible Navier-Stokes model designed for the study of the atmosphere, ocean and climate. It can solve hydrostatic and non-hydrostatic equations enabling it to simulate fluid phenomena over a wide range of scales, from global circulation to local convection (*Marshall et al.*, 1997a,b). Its adjoint capability enables it to be applied to parameter and state estimation problems (*MITgcm*, 2014).

The MITgcm works by enabling different code packages depending on the problem to be solved. For example the 'gfd' package is used when solving fluid dynamics problems. Further packages can be added to the model depending on the problem being solved, for instance the 'shelfice' package (Section 3.3.2) and 'icefront' package (Section 3.3.3) which model ice-ocean interactions at the base of an ice shelf and at the vertical ice front of a marine-terminating glacier respectively. The following sections introduce the packages specific to the problems studied here.

3.3.1 The ocean in MITgcm

Within the following models the ocean is treated as hydrostatic ocean and a linear free surface is used. The domain is small and therefore it is treated as an f-plane with a Coriolis parameter of $1.4301 \times 10^{-4}\ \mathrm{s}^{-1}$, which is equivalent to a latitude of 80°N.

The model uses a horizontal diffusivity of $2.5\ \mathrm{m}^2\mathrm{s}^{-1}$, a vertical diffusivity of $1.4 \times 10^{-4}\ \mathrm{m}^2\mathrm{s}^{-1}$, a vertical eddy viscosity of $2 \times 10^{-3}\ \mathrm{m}^2\mathrm{s}^{-1}$, a horizontal eddy viscosity of $15\ \mathrm{m}^2\mathrm{s}^{-1}$, and a horizontal biharmonic viscosity of $2.5\ \mathrm{m}^4\mathrm{s}^{-1}$. A third-order flux-limited advection scheme is used. These values are scaled from those

used by *Losch* (2008) and tuned so that the four channel idealised case provides a relatively consistent mean met rate compared to the observations of *Rignot and Steffen* (2008). These values assume that mixing processed are consistent throughout the whole water column, which does not take into account different levels of mixing within the stratified layer and deeper ambient water. Mixing closure schemes, such as Mellor-Yamada, attempt to model the turbulent fluxes in the model equations. These schemes can be computationally expensive and were therefore not included within the model.

For the idealised model domain, the models were spun up with a 60-second timestep until the maximum strength of barotropic circulation was steady, after five years. Five years was chosen as it allowed all of the different idealised geometries to reach a steady state needed for comparison of simulations. The realistic model domain was spun up with a 6-second timestep until steady, using the same criteria, after a 12 month period. Unless stated otherwise all results are presented as monthly averages of the final month.

3.3.2 Representation of ice shelves in MITgcm

The MITgcm 'shelfice' package (*Losch*, 2008) models processes in the cavity beneath an ice shelf and at the interface between the ice shelf base and the ocean. The ice shelf impacts the ice shelf cavity in two ways, dynamically through altering the pressure in the water column beneath the ice shelf, and thermodynamically via freezing and melting at the ice-ocean interface.

From *Losch* (2008), the total pressure p_{tot} in the ocean can be divided into the pressure at the top of the water column p_{top}, the hydrostatic pressure and the non-hydrostatic pressure contribution p_{NH}:

$$p_{tot} = p_{top} + \int_{z}^{\eta-h} g\rho dz + p_{NH}, \tag{3.28}$$

where g is gravitational acceleration, ρ is the density of the water, η is the dynamic sea surface height and z is the vertical coordinate. z is positive upwards, meaning that in the following equations it takes negative values. For the open ocean, p_{top} is the atmospheric pressure p_a, and h is zero. Underneath an ice shelf, which is assumed to be floating in isostatic equilibrium, p_{top} is the sum of the atmospheric pressure and the weight of the ice shelf. It is this weight that is provided to the model as a boundary condition at the top of the water column.

The weight is computed by integrating a density profile ρ^*, that is constant in time and corresponds to the seawater replaced by the ice shelf, from $z = 0$ to a "reference" ice shelf draft at $z = -h$:

$$p_{top} = p_a + \int_{-h}^{0} g\rho^* dz. \tag{3.29}$$

Beneath the ice shelf, η is the deviation from the "reference" ice shelf draft h. During the model integration, η adjusts such that isostatic equilibrium is maintained for sufficiently slow and large-scale motions.

In the MITgcm, the total pressure anomaly p'_{tot}, which is used for pressure gradient calculations, can be found by substituting a depth-dependent contribution $g\rho_0 z$ with a constant reference density ρ_0 into p_{tot}. Equation (3.28) then becomes:

$$p_{tot} = p_{top} - g\rho_0(z + h) + g\rho_0\eta + \int_{z}^{\eta-h} g(\rho - \rho_0)dz + p_{NH}, \tag{3.30}$$

which, after rearranging becomes:

$$p'_{tot} = p'_{top} + g\rho_0\eta + \int_{z}^{\eta-h} g(\rho - \rho_0)dz + p_{NH}, \tag{3.31}$$

where $p'_{tot} = p_{tot} + g\rho_0 z$ and $p'_{top} = p_{top} - g\rho_0 h$. The non-hydrostatic pressure contribution p_{NH} is neglected in the following.

The ice shelf contribution to p_{top} is computed by integrating equation 3.29 from $z = 0$ to the bottom of the last fully dry cell within the ice shelf:

$$p_{top} = g \sum_{k'=1}^{n-1} \rho^*_{k'} \Delta z_{k'} + p_a, \tag{3.32}$$

where k' is the layer index, n is the vertical index of the first "wet" cell and $\Delta z_{k'}$ is the thickness of the k'th layer. The pressure anomaly for evaluating the pressure gradient is calculated in the centre of the "wet" cell k as:

$$p'_k = p'_{top} + g\rho_0\eta + g \sum_{k'=n}^{k} \left((\rho_{k'} - \rho_0)\Delta z_{k'} \frac{1 + H(k' - k)}{2} \right), \tag{3.33}$$

where $H(k' - k) = 1$ for $k'<k$ and 0 otherwise.

One of the severe limitations of z coordinates is the 'staircase' representation of complex geometry. One way to overcome this limitation is to increase the vertical resolution, however this brings with it an increase in computational cost. Another method of addressing this issue is by implementing the partial cell method. Partial cells are those which have a portion of the cell which is "dry" and a portion that is "wet". This method allows for sea bed topography and ice shelf topography to be approximated more accurately than with full cells and leads to a generally smoother solution (*Adcroft et al.*, 1997). A minimum size of partial cell (hFacMin) can be defined to avoid tiny volumes. Here a value of 0.05 is used for hFacMin, meaning that a wet cell will not be less than 5% ocean, which is equivalent to 50 cm at the 10 m vertical resolution used. For topography which lies between a fully "dry" cell and a cell with a "wet" portion less than hFacMin, then the fraction of the cell which is "wet" is rounded to either 0 or the hFacMin value.

The 'shelfice' package implements ice shelf basal melting using the thermodynamic equations from section 3.2. The calculations depend upon the ocean properties beneath the ice, for which the simple method of *Losch* (2008) is used, which

takes the mean temperature and salinity from all cells within a distance dz from the ice base, where dz is a fixed vertical lengthscale (here $dz = 10$ m). This distance spans both the partial cell and a portion of the full cell below it. We also use the mean velocity components (u_m and v_m) over a distance of dz to calculate the friction velocity u_*. The velocity in the centre of a cell is calculated from v velocity components at the north and south edges of the cell and u velocity components on the east and west edges (MITgcm uses a 'C' grid), so, over a vertical distance dz, the calculation of the friction velocity u_* is dependent on eight u_m and v_m velocity components in total.

3.3.3 Ice Front Melting

Tidewater glaciers, and ice shelves whose ice front is thick enough to penetrate into deeper warm waters, experience significant melting on their near-vertical ice fronts. Such melting may control glacier retreat rates, grounding line position and glacier flow speeds (*Nick et al.*, 2009). Undercutting of a tidewater glacier's ice front, caused by enhanced subaqueous melting, has been found to enhance calving rates by up to ten times the mean melt rate (*O'Leary and Christoffersen*, 2013). It is reasonable to hypothesize that a similar mechanism could occur at the ice front of an ice shelf, meaning that the inclusion of ice front melting is important when assessing the mass balance of an ice shelf.

The 'shelfice' package (section 3.3.2) calculates ice-ocean interactions on the horizontal base of an ice shelf only and not on the vertical face of an ice shelf. This latter feature was introduced in the 'icefront' package by *Xu et al.* (2012), using an equivalent three-equation formula to that used below floating ice shelves (e.g. *Holland et al.* (2008b); *Losch* (2008)). The three equations used in the 'icefront' package

are:

$$T_B = aS_B + b + cp, \tag{3.34}$$

$$c_O \rho_O \gamma_{T'} |w|(T - T_B) = m[L + c_I(T_S - T_B)], \tag{3.35}$$

$$\rho_O \gamma_{S'} |w|(S - S_B) = mS_B, \tag{3.36}$$

where w is the vertical velocity next to the ice face and $\gamma_{(T'/S')}$ are parameterisations of the heat and salinity transfer coefficients. As melting and freezing on a vertical ice face do not have the same stabilizing or destabilizing effect on the buoyant flow as on a near horizontal ice shelf base, it would not be sensible to use the same transfer parameters in Eqn. 3.25. Therefore constant values of $c_d^{1/2}\Gamma_{(T/S)}$ from *Jenkins et al.* (2010b) are used. Equations (3.34) to (3.36) are solved at the vertical ice face to obtain melt rates.

3.3.4 Boundary conditions

There are three different possibilities for the vertical boundaries of a domain in MITgcm. They can be set as a wall, a restoring boundary or an open boundary, all three of which are used at different times in the following modelling studies.

The wall boundary condition is used in all of the following modelling studies to represent the side walls of the fjord. When a boundary is set as a wall, there is no flow or diffusion of tracers across the boundary. The modelling studies contained within this thesis all use free slip walls. This is because we expect the boundary layer to be much smaller than the 250 m horizontal resolution and would therefore not be resolved by a no-slip condition. The free slip boundary condition for boundaries in the x direction is $\frac{\delta u}{\delta y} = 0$ and for boundaries in the y direction $\frac{\delta v}{\delta x} = 0$.

Restoring boundary conditions are used as a 'sponge' layer with a northern wall in the majority of the following idealistic domain studies. They are used to restore salinity and potential temperature to prescribed profiles and to prevent flow from leaving the domain. In all studies involving restoring boundary conditions, salinity and potential temperature are restored over a 24-hour timescale. Restoring boundaries maintain a heat flux into the domain as the properties of the water flowing southwards after contact with the northern boundary have been restored to the prescribed profiles. This maintaining of heat flux means that a flow into the domain does not need to be prescribed on the northern boundary.

Open boundary conditions are used in the realistic domain for the open ocean boundaries on the northern boundary, and the northern section of the eastern and western boundaries. Open boundaries allow water to flow into and out of the domain according to the model calculations. Water flowing into the domain has properties set to a predefined profile, with values depending on the depth of the inflow. Water flowing out of the domain maintains its properties defined by the model. The open boundary conditions balance the flow in and out of the domain to ensure that the volume of water within the domain is conserved.

In all of the modelling studies the sea bed has a prescribed no-slip setting; $u = v = 0$ at $z = -H$, where H is the local depth of the domain. This no-slip setting is implemented as the vertical resolution is of the order of the expected bottom boundary layer and therefore becomes resolvable.

Chapter 4

Impact of Basal Channels in an Idealised Domain

Basal channels have been shown to alter the circulation of melt water in a sub-ice shelf cavity, directing the melt water out of the cavity within the channels (*Payne et al.*, 2007; *Mankoff et al.*, 2012), leading *Payne et al.* (2007) to suggest that this would lead to enhanced melting within the channel crest, causing a deepening of the channel downstream. *Dutrieux et al.* (2013), however, showed that the channels were initially carved via ocean melting, before diminishing downstream as the channel keels were preferentially melted.

The channels' impact on basal melting was investigated by *Gladish et al.* (2012) who created a coupled ice shelf-ocean plume model. They found that basal channels actually increased the stability of ice shelves by preventing the development of focussed high melt rates which melted completely through the ice shelf in the absence of channels. However, the reduced ocean physics of this simple model precluded a study of the physical mechanism behind this sensitivity. Here I use the MITgcm to investigate how the channels impact the channeling of the meltwater, the location and strength of basal melting and their impact on ice shelf stability.

4.1 Model specifics

To investigate the impact of basal channels, the MITgcm, as described in Chapter 3, was used with restoring boundary conditions on the northern boundary. The initial conditions and restoring profiles are detailed below. The 'icefront' package was turned off for models run during this chapter, meaning that melting on the vertical face of the ice front was not modelled.

Nine differing versions of the idealised ice shelf geometry, discussed in Section 2.4.1, with the number of channels varying from 0 to 8, are included. As the channels sinusoidally span the entire width of the ice shelf, as the number of channels increases, the channel width decreases and the channel slope gradient increases. This means that we have a spectrum of ice shelf geometries from a low number of wide, shallowly sloping channels to a higher number of steeper, narrower channels. The no-channel case is a special case where the draft is taken as the across-shelf mean channel and keel profile to ensure the mean draft of all nine geometries remains constant. A Cartesian grid with a resolution of 250 m in the horizontal and 10 m in the vertical was implemented, and partial cells with a minimum height of 0.5 m were used to better represent the ice shelf base. The domain is south to north orientated with the ice shelf extending into the domain from the southern boundary. All model runs were spun up for a total of 5 years with a time-step of 60s.

In 2009, *Johnson et al.* (2011) conducted a CTD section across Petermann Fjord, between the ice front and fjord-mouth sill, and found a cold, fresh water mass overlaying a warmer, saltier layer of modified Atlantic Water. The temperature and salinity profiles used for initial conditions and boundary restoring within the model were based on this observational data. In the top 100 m of the water column the temperature profile increases linearly with depth from $-1.7\,^{\circ}\mathrm{C}$ at the surface to $0.3\,^{\circ}\mathrm{C}$, and salinity increases linearly from 30 to 34.8. The sharp inflection in the profiles represents the sharp pycnocline seen by *Johnson et al.* (2011). The water column is

homogenous below 100 m (Fig. 4.1).

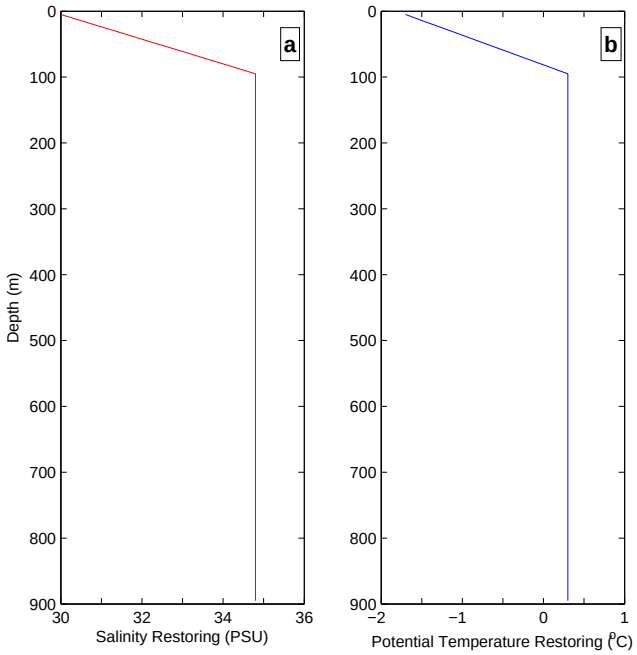

Figure 4.1: a) Salinity and b) potential temperature profiles used for model initialisation and restoring on the northern boundary for all 9 scenarios.

4.2 Results

4.2.1 Oceanography

Within the fjord there is a geostrophic circulation bringing warm modified Atlantic Water into the cavity beneath the ice shelf along the western boundary of the domain, whilst a return flow transports water out of the cavity along the eastern boundary (Fig. 4.2). The warm water melts the ice base, introducing a source of freshwater and hence buoyancy. This buoyant meltwater forms a cooler plume rising against the base of the ice shelf (Fig. 4.3), introducing an overturning element to the cavity circulation. Whilst this water is warmer than the localised freezing point, it will continue to melt the ice base, further increasing the buoyancy of the plume.

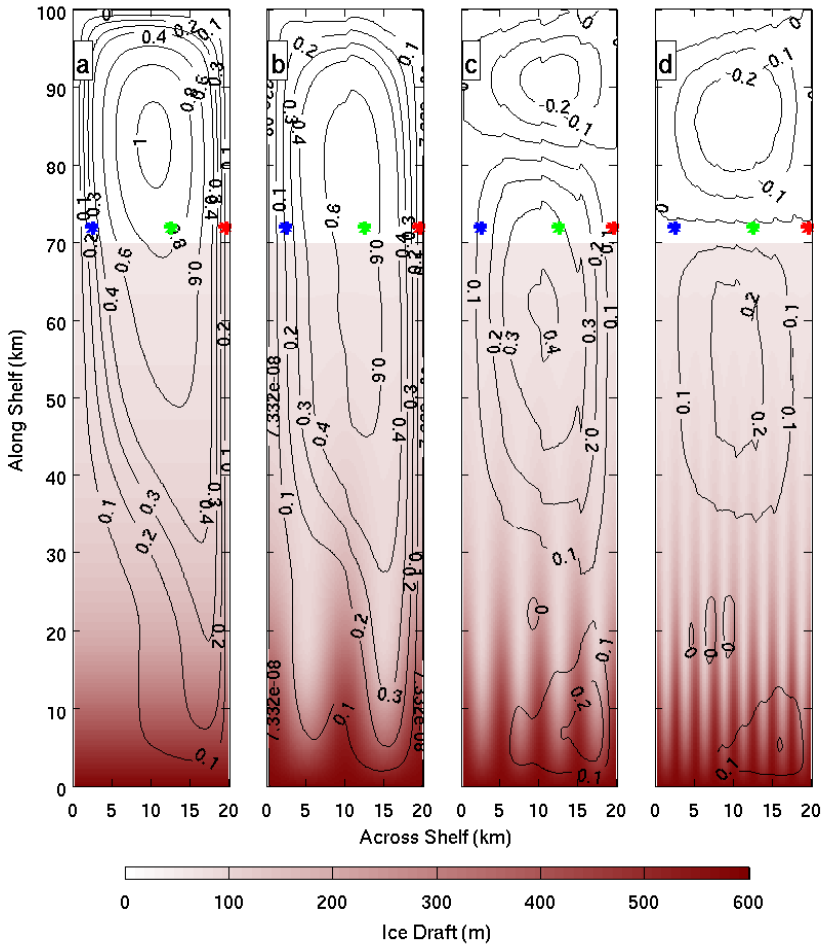

Figure 4.2: Barotropic stream function (contours) overlying ice draft (colored) for a) 0-channel, b) 2-channel, c) 4-channel and d) 8-channel cases. The coloured dots denote the location of the corresponding profiles used in Figures 4.4 and 4.5.

Figure 4.2 shows the barotropic stream function (contours) beneath ice shelves with 0, 2, 4 and 8 channels. The color represents the ice draft. The barotropic stream function beneath an ice shelf with no basal channels (Fig. 4.2a) shows a strong cyclonic circulation within the domain, with a fast flow out of the cavity against the eastern wall (Coriolis favoured), as found previously (e.g. *Losch* (2008)). The flow returning under the ice shelf on the western boundary brings warm fjord water towards the ice shelf and diverts across the ice shelf to feed this jet, approximately 40 km north of the grounding line. As channels are introduced to the base of the ice shelf

(Fig. 4.2b - d) a number of changes occur. The asymmetric nature of the stream function and the strength of the barotropic circulation decrease as the number of channels increases. This weakening occurs in conjunction with a decrease in ice-shelf basal melting (Section 4.2.2), which reduces the buoyancy forcing on the circulation. The weakening reduces the supply of heat to the cavity and ice base, in turn reducing the level of basal melting and hence further reducing the buoyancy forcing.

Figures 4.2c and 4.2d show that when there are more than four basal channels, a separate anticyclonic circulation is spun up in the open ocean section at the mouth of the fjord. As the water column exits the ice shelf cavity on the eastern boundary, there is a step change in water column thickness, due to the transit past the ice front. This leads to a stretching of the water column which, the principle of the conservation of potential vorticity dictates, will result in the water column turning westward after passing the ice front. Viscosity causes water to the north of the exiting flow to also have a westward flow, and the conservation of mass dictates this must cause a southward flow on the northern edge of the eastern boundary, hence setting up the anticyclonic circulation seen. As the step change in water column thickness is small (60 m), this only occurs for weak flows out of the cavity, i.e. cases with a larger number of channels. It should be noted that this fjord mouth circulation may not be realistic since this is a closed domain, unlike Petermann Fjord which opens into Hall Basin. This will be investigated in Chapter 6.

The path of the buoyant meltwater layer formed when the warm modified Atlantic water melts the ice is apparent from the north-south sections of temperature and salinity anomalies (Fig. 4.3). This figure shows the difference between the modelled temperature and salinity at the end of the model run and their corresponding initial conditions in the 2-channel case. For both differences blue represents a decrease from the initial condition whilst red indicates an increase.

The meltwater is cooler and fresher than the initial deep water and flows up

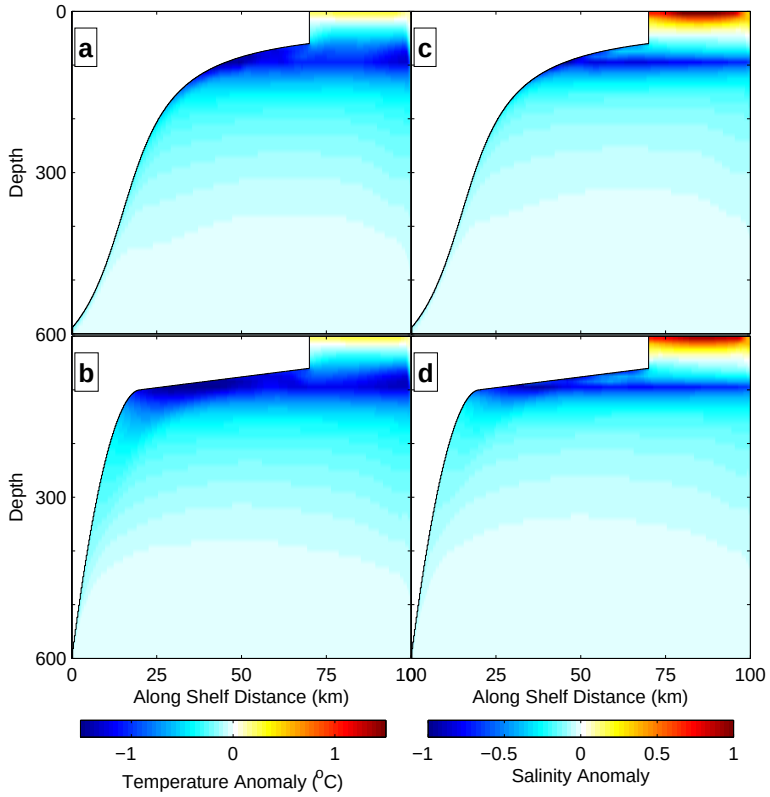

Figure 4.3: Anomaly profiles for the two channel case a) temperature anomaly along the keel down the centre of the domain, b) temperature anomaly along the crest of the eastern channel, c) salinity anomaly along the keel down the centre of the domain and d) salinity anomaly along the crest of the eastern channel. The profile locations are denoted by yellow lines in Figure 4.6.

within the channels until it reaches neutral buoyancy at the prescribed pycnocline, detaches from the ice shelf base, and flows northwards away from the ice shelf. This occurs approximately 20 km north of the grounding line and bears a striking resemblance to the observational interpretation of *Johnson et al.* (2011). This flow is contained within the channels until the keels become shallower than the pycnocline depth, approximately 40 km north of the grounding line. The model has smoothed the potential temperature and salinity depth profiles, from the open ocean section, when compared with the initial conditions. This results in the positive anomalies seen at the surface in Figure 4.3 for both potential temperature and salinity.

Figure 4.4 shows the $\Theta - S$ diagram for selected water columns from the four-

channel configuration, 2 km north of the ice front. There are 3 depth profiles, 2 located in the centre of the first and third channels (blue and green respectively from the western fjord wall) and one 0.5 km from the eastern boundary (red), in the boundary current flowing out of the ice shelf cavity as described above. The black profile is the northern boundary restoring profile.

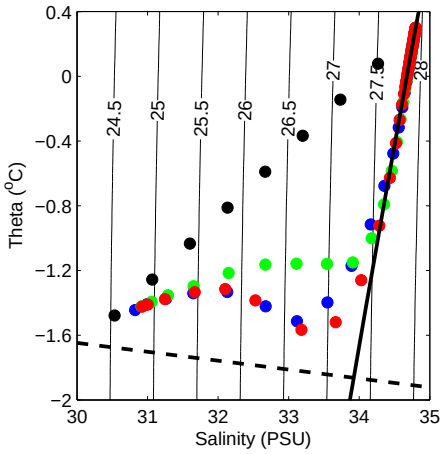

Figure 4.4: $\Theta - S$ diagram for the 4 channel configuration. The solid black line represents the Gade line with gradient 2.77 °C/PSU and the dashed black line represents the freezing temperature. The blue and green profiles are situated in the middle of the first and third channel respectively, whilst the red profile is situated 0.5 km from the eastern fjord wall. The black profile is the northern boundary restoring profile. Contours are density contours (density -1000 kg/m^3) separated by 0.5 kg/m^3. The location of the profiles are shown by the coloured dots in Figure 4.2.

At depths greater than the grounding line, water in the fjord is uniform in all of the profiles. Between a depth of 100 m and the depth of the grounding line, water in all profiles fall on a straight line with gradient 2.77 °C/PSU, which is in agreement with glacial ice melted by sea water with a potential temperature of 0.3 °C and a salinity of 34.8 PSU (Eqn. 1.2). Above 100 m in all profiles the gradient shallows indicating a mixing between waters on the Gade line and cool surface layer waters.

Even though all of the 3 profiles show a meltwater signal up to depths of 100 m,

the temperature of water in the more eastern profiles is cooler, indicating that there is a higher meltwater fraction in these waters than in the more western profiles. This suggests that the majority of meltwater is exiting the ice shelf cavity in the eastern boundary current as seen in Section 4.2.2.

As the number of channels is reduced (Fig. 4.5 a&b) the profiles on the western side of the fjord deviate from the Gade line deeper in the water column whilst the profiles on the eastern side of the fjord deviate at 100 m as in the four channel configuration. For the 8 channel configuration, (Fig. 4.5c), all of the profiles have deviated from the Gade line below a similar depth, 110 m. The meltwater signal seen in configurations with a fewer number of channels is cooler than those with a greater number of channels, indicating that there is a higher meltwater fraction in these channels. This is due to the change in melt rates described in Section 4.2.2.

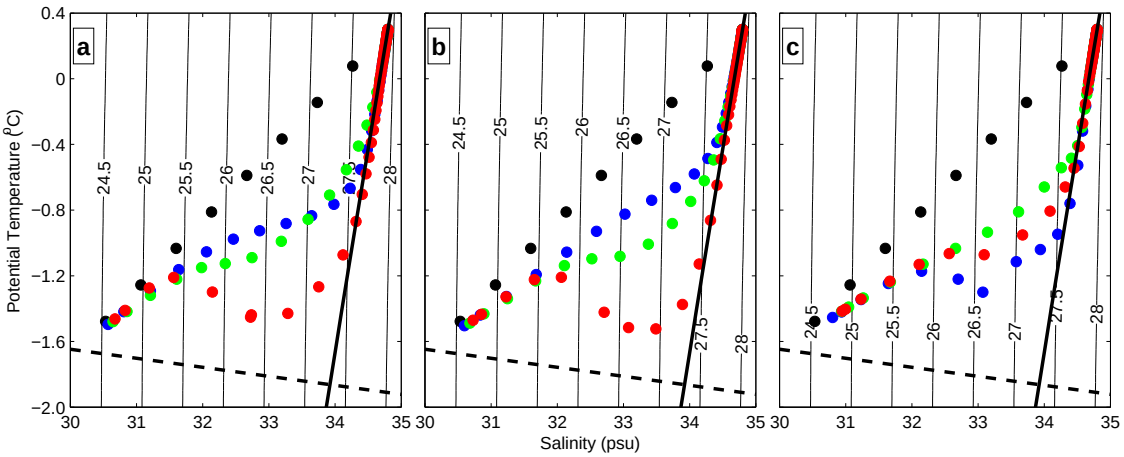

Figure 4.5: $\Theta - S$ space for the a) 0-, b) 2- and c) 8-channel configurations. The solid black line represents the Gade line with gradient 2.77 °C/PSU and the dashed black line represents the freezing temperature. Contours are density contours (density -1000kg/m^3) separated by 0.5kg/m^3. The profiles are taken in the same location as the four channel configuration and their locations are denoted by the coloured dots in Figure 4.2.

This sensitivity indicates that for a configuration with a small number of channels, more of the meltwater deflects towards the eastern boundary and exits the cavity in the boundary current. As the number of channels increases, the meltwater signal can be seen at shallower depths in profiles moving further west across the

domain, indicating a change in sub-ice shelf flow. As the number of channels continues to increase, the meltwater signal deviates from the Gade line at greater depths, suggesting a reduced buoyancy of the meltwater plume, caused by a reduction in melt rates.

4.2.2 Basal Melting

When there are no channels in the base of the ice shelf, a strong geostrophically balanced boundary current is formed in the sub-ice layer, rising along the eastern boundary and leaning on the right hand wall of the fjord (Fig. 4.6a) [e.g. *Holland et al.* (2008b)]. Due to the velocity dependence of melting, the strongest basal melting is focused underneath the strongest part of the boundary current. The Rossby deformation radius (L_R) of the buoyant meltwater layer can be calculated using equation 3.10 and the length scales used for reducing equations 3.1 and 3.2. This gives a Rossby deformation radius of 2.8 km and this is the length scale at which rotational effects become important. We would expect the width of the geostrophically balanced boundary current to be in agreement with this, and we can see from Figure 4.6a that indeed the width is approximately 2.5 to 3 km.

Figure 4.6 shows the monthly averaged sub-ice layer velocities (velocities from the 10 m of the ocean column immediately beneath the ice) overlain on monthly averaged basal melt rates (m/a) for the final month of each simulation. It can be seen that the introduction of channels modifies the formation of the boundary current, inducing a circulation within each channel (Figs. 4.6b and 4.6c). This circulation consists of a southward flow on the western slope of the channel and a northward flow on the eastern slope. There is little flow in the channel crests. There is some transfer over the keels between the channels in an eastward direction, which leads to slightly faster flows and stronger melting in the more easterly channels.

The strong geostrophically balanced boundary current persists for several hun-

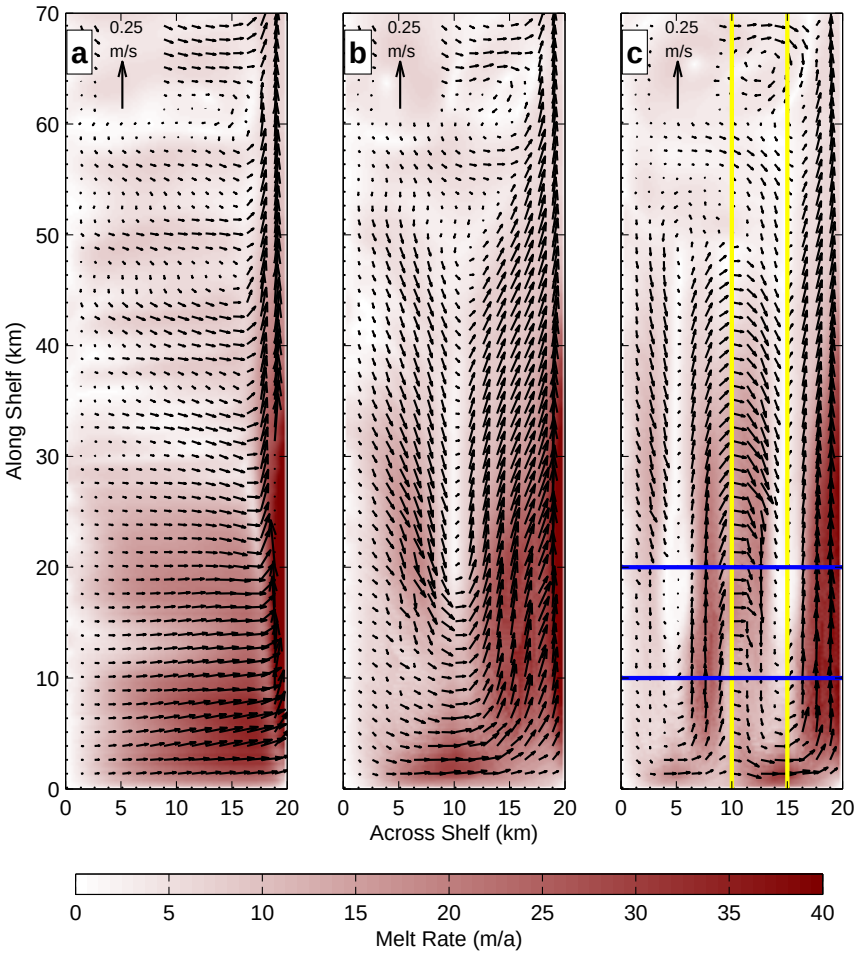

Figure 4.6: Modelled monthly averaged sub-ice layer velocities for a) 0-, b) 1- and c) 2- channel cases overlain on monthly averaged basal melt rates (m/a). Vectors are shown every 5 grid points. The yellow lines in panel c indicate the location of the profiles shown in Figure 4.3, whilst the blue lines show the location of the profiles shown in Figure 4.12.

dred metres beneath the ice shelf. Near the grounding line the impact of the channels on ocean flow can be felt up to 100m deeper than the channel keels. This depth decreases with both an increase in distance downstream of the grounding line, and an increase in the number of basal channels. As the ice shelf draft shallows to above the stratification depth (100 m), the meltwater layer detaches from the ice shelf and there is no channel signature beneath the stratification depth.

Within each channel, melting is strongest in the steepest part of the ice shelf

near the grounding line, where the channels begin, and on the eastern slope of the channels. The current is still strongest on the eastern boundary of the domain, but the maximum flow is decreased, as is the peak melting associated with it. The melt rate is low near the ice front where the meltwater layer is detached from the ice base and the flow is not topographically constrained.

The mean melt rate for the whole ice shelf is roughly the same for the 0- and 1-channel cases, but as more channels are introduced, the mean melt rate decreases monotonically (Fig. 4.7a). There is a reduction of approximately 40% in melting between the 1- and 4- channel cases, after which the sensitivity of the mean melt rate to the number of channels declines, with only a further 8% reduction between the 4- and 8- channel cases.

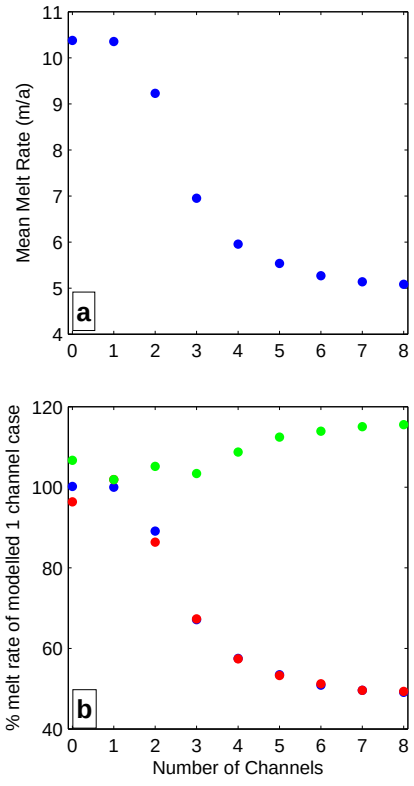

Figure 4.7: (a) Mean melt rate as a function of number of basal channels. (b) derived melt rate as proportion of 1 channel model case for modelled results (blue) keeping $(T_B - T_M)$ constant (red) and keeping u_* constant (green).

To a good level of approximation, the melt rate is proportional to the product of friction velocity, u_*, and thermal driving, $(T_B - T_M)$, (neglecting heat conduction in (3.16)) (*Holland and Jenkins*, 1999; *Holland et al.*, 2008b). To investigate the relative effects of these quantities, the spatial mean values of both were calculated for each model run. I then investigated their effect by substituting these values into (3.16), (3.20), (3.21) and (3.25) - (3.27), and calculating the domain averaged melt rate. We then investigate the effect of u_* in the cases with different channels by keeping $(T_B - T_M)$ constant at the one-channel modelled mean, and likewise we investigate $(T_B - T_M)$ by keeping u_* constant at the one-channel modelled mean.

Figure 4.7b shows modelled and derived melt rates as a percentage of the modelled 1-channel case. The blue dots represent the modelled mean melt rates as a percentage of the 1-channel modelled mean melt rate. The green dots represent the derived mean melt rates when varying only the mean $(T_B - T_M)$ and the red dots represent derived mean melt rates when varying only the mean u_*. The melt rate estimates when varying $(T_B - T_M)$ are basically constant, with only a slight increase, as the number of channels increases, in contrast to the modelled melt rates. The slight increase is caused by the domain mean $(T_B - T_M)$ increasing with the addition of more channels due to the decrease in basal melting. Therefore when the friction velocity is kept constant at the one-channel modelled mean, the increase in thermal forcing will lead to an increase in derived mean melt rate. Varying u_* provides melt rate estimates which are consistent with the modelled melt rates, implying that a change in friction velocity drives the change in melting as more channels are introduced. An understanding of the mechanism behind the change in u_* is therefore necessary to understand the change in the mean melt rates.

Due to the change in sensitivity between the group of ice shelf geometries with a small number of wide channels and the group with a large number of narrow channels, these groups are considered separately.

4.2.3 Wide Channels

To understand the initial strong decrease in u_*, and hence mean basal melt rates when the number of channels is increased, we consider the difference in sub-ice layer u_*, $|v_m|$ and $|u_m|$ between the 1- and 2- channel cases (Fig. 4.8). The figures show the 1-channel field subtracted from the 2-channel field, meaning that a blue color represents a decrease when going from 1-channel to 2-channel, whilst a yellow or red color represents an increase.

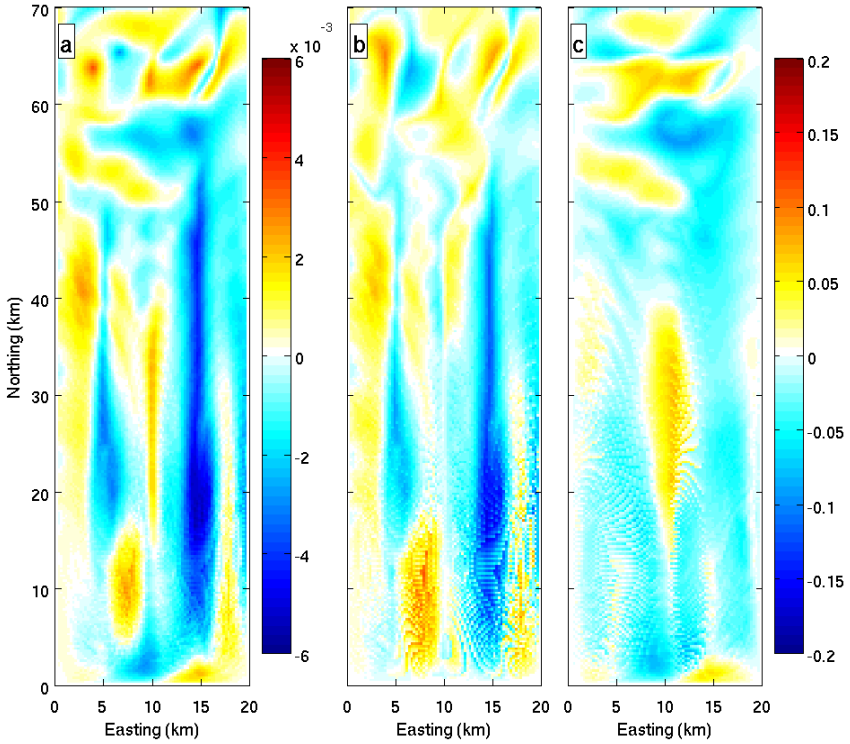

Figure 4.8: Difference in monthly averaged (a) u_*, (b) $|v|$ and (c) $|u|$ between 1- and 2-channel cases

All three panels show a decrease as the number of channels is increased. In the areas representing the channel crests in the two channel case, the flow has changed from a north-south flow to little or no flow, hence the dark blue regions in Figures 4.8a and b. The channel crest on the one channel case has become a keel in the two channel case so the flow has changed from little or no flow to an across shelf flow,

represented by the yellow region in Figure 4.8(c).

Comparison of the spatial patterns show that there is a higher correlation between u_* and $|v_m|$ (0.847) than u_* and $|u_m|$ (0.394),when comparing the first 50 km of the ice shelf, meaning that the majority of the decrease in u_* can be explained by a decrease in $|v_m|$. (Note that the final 20 km of the ice shelf was excluded from the analysis as the channel depth is less than 10 m under this section of ice shelf, and the ocean surface layer is no longer topographically constrained). Therefore to understand the decrease in mean melt rate it is necessary to understand the decrease in $|v_m|$.

Figure 4.9 shows $|v_m|$ 20 km downstream of the grounding line for the 1- (blue) and 2- (red) channel cases. It can be seen that the maximum velocity (excluding the current leaning on the eastern boundary wall) in both cases is similar. The main difference between the cases is the inclusion of more 'no flow' regions; the 1-channel case has one crest, whilst the 2-channel case has two crests and one keel. These extra stagnant regions lead to a decrease in mean $|v_m|$ and hence u_*.

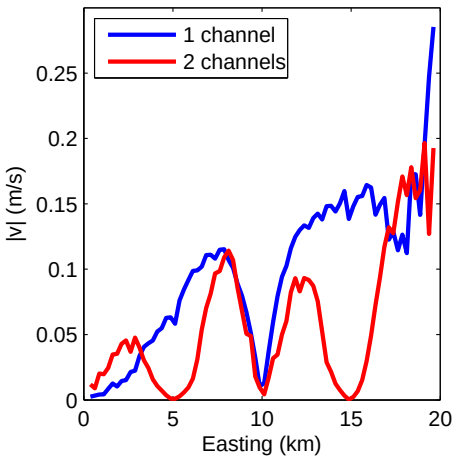

Figure 4.9: $|v|$ velocities 20km downstream of the grounding line (1-channel - blue, 2-channels - red)

The inclusion of these extra 'no flow' regions persists for changing viscosity and diffusivity model parameters, however the maximum $|v_m|$ varies, as does the point at

which the sensitivity of mean basal melt rates to the number of channels, the latter is discussed later in this chapter. Therefore it is believed that the inclusion of further 'no flow' regions is a physical mechanism, rather than model artifact.

Figures 4.10 and 4.11 show the individual terms in the MITgcm momentum balance for the 1- and 2- channel cases. Unlike all other variables these are plotted as an instantaneous 'snapshot' to ensure they are balanced quantities. In both cases the primary balance is between the pressure gradient and Coriolis terms, so the flow is basically geostrophic. This means that the magnitude of the v velocity component is governed by the across-shelf pressure gradients. As more channels are introduced to the ice shelf, the across-shelf gradients in ice draft increase. One might expect that the across-shelf isopycnal slope, and hence pressure gradients, is proportional to the ice base slope. This would imply that the speed of the geostrophic north-south flow on the channel sides would increase as the number of channels is increased, compensating the addition of 'no flow' areas as described above. However this is not the case (Fig. 4.9).

Figure 4.12 shows across-shelf density gradients and isopycnal contours 20 km downstream of the grounding line for the 1- and 2- channel cases. The largest density gradients are closest to the channel slopes, in the rising meltwater, whilst in the middle of the channels the isopycnals are flat. Density gradients are similar in the 1- and 2- channel cases. It is this consistency in isopycnal gradients, despite a doubling of ice-shelf draft gradients, that causes the constant maximum flow speed seen in Figure 4.9.

In summary, for 0 - 4 channels, increasing the number of channels increases the number of 'no-flow' regions, beneath ice keels and crests. The isopycnal gradients beneath ice slopes do not increase to compensate this effect, so the mean north-south velocity decreases overall. This reduction in velocity in turn leads to a rapid reduction in u_* and hence the overall melt rate. However, Figure 4.7 shows that

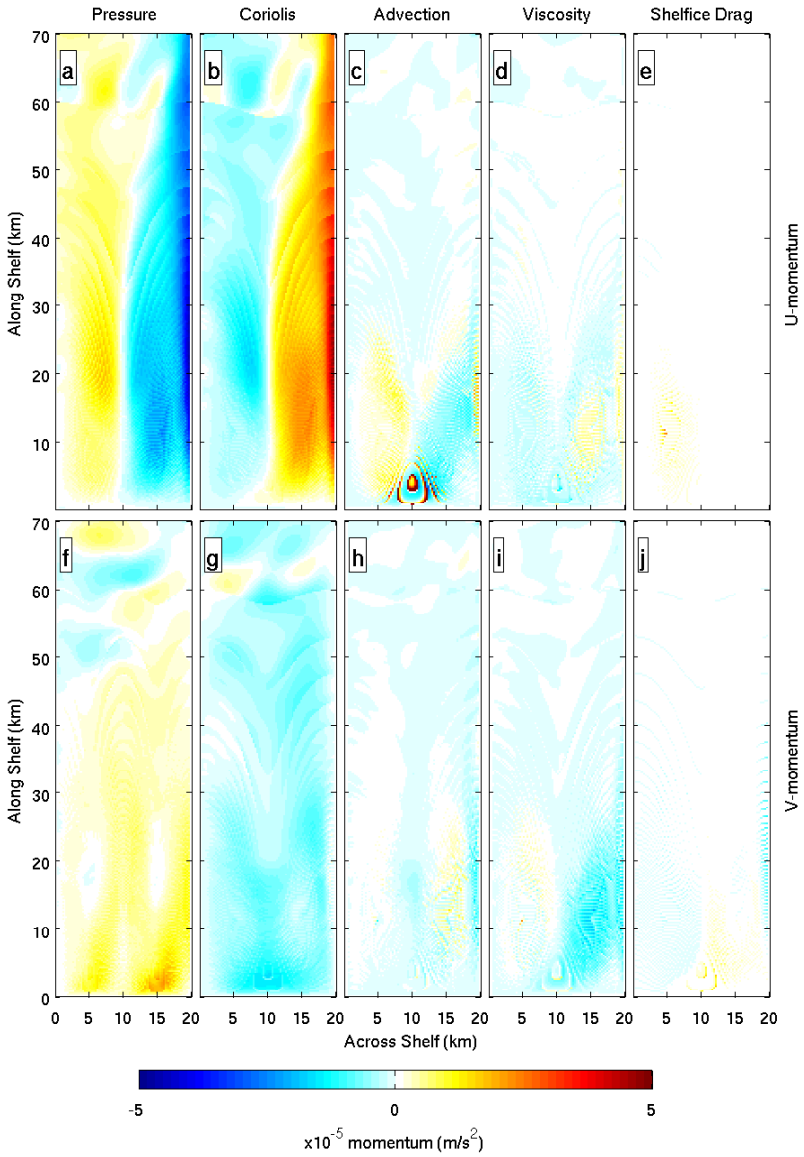

Figure 4.10: Instantaneous momentum terms for 1-channel case. Top row is u-momentum, bottom row is v-momentum.

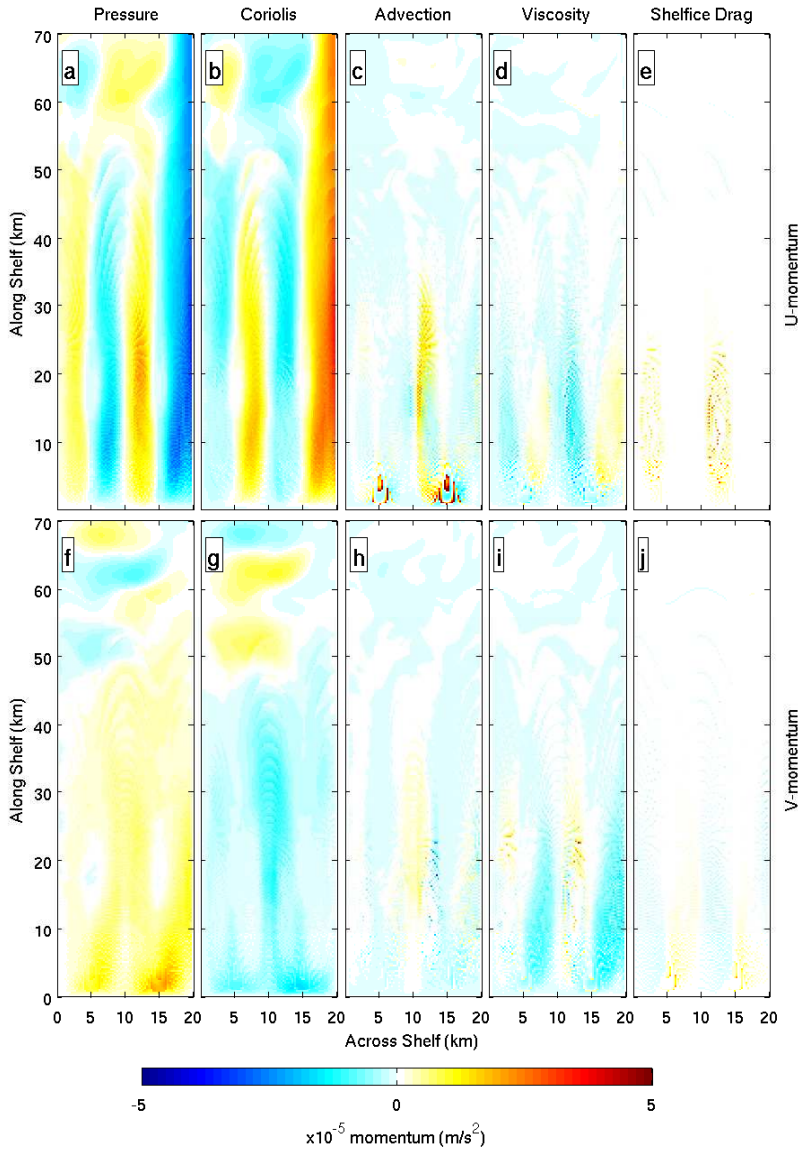

Figure 4.11: Instantaneous momentum terms for 2-channel case. Top row is u-momentum, bottom row is v-momentum)

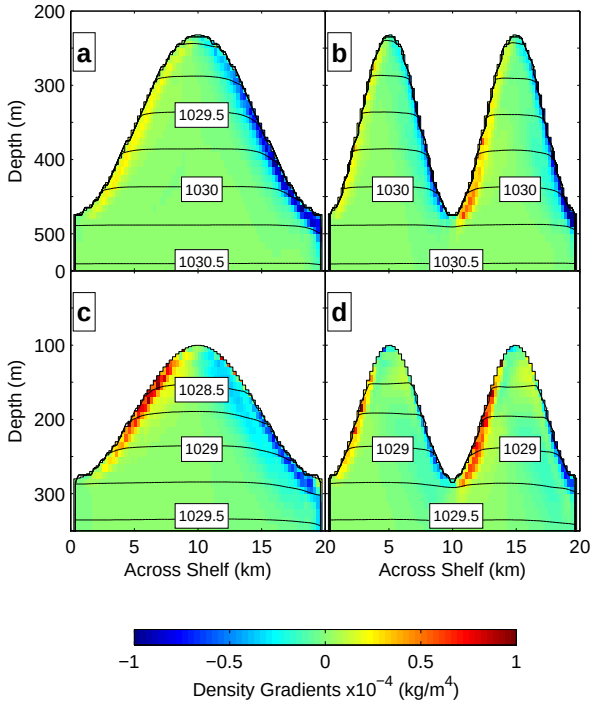

Figure 4.12: Monthly averaged density contours overlaying density gradients for 1- and 2-channel cases, 10 km (top row) and 20 km (bottom row) downstream from the grounding line.

cases with a larger number of channels have a weaker melting sensitivity, suggesting that a different mechanism operates.

4.2.4 Narrow Channels

Figure 4.13 shows the sub-ice layer flow pattern and melt rate under ice shelves with higher numbers of channels. It can be seen that as more basal channels are added, the sub-ice layer circulation within each channel changes from a two-way flow located on both channel slopes, to a single northward flow in the centre of the channels. This represents a change of flow from a geostrophic horizontal circulation to a vertical overturning circulation within the channel. This can be seen by comparing the terms in the momentum equation (Figure 4.14) where it can be seen that the advection and viscosity terms become of the same order as the pressure and rotational

terms. The flow speed is no longer governed by across-shelf density gradients, and all of the above arguments break down. The overturning circulation is driven by mean gradients in the along-shelf direction, which are unaffected, on average, by the number of channels. This explains the insensitivity to channel number after the circulation changes from geostrophic to overturning.

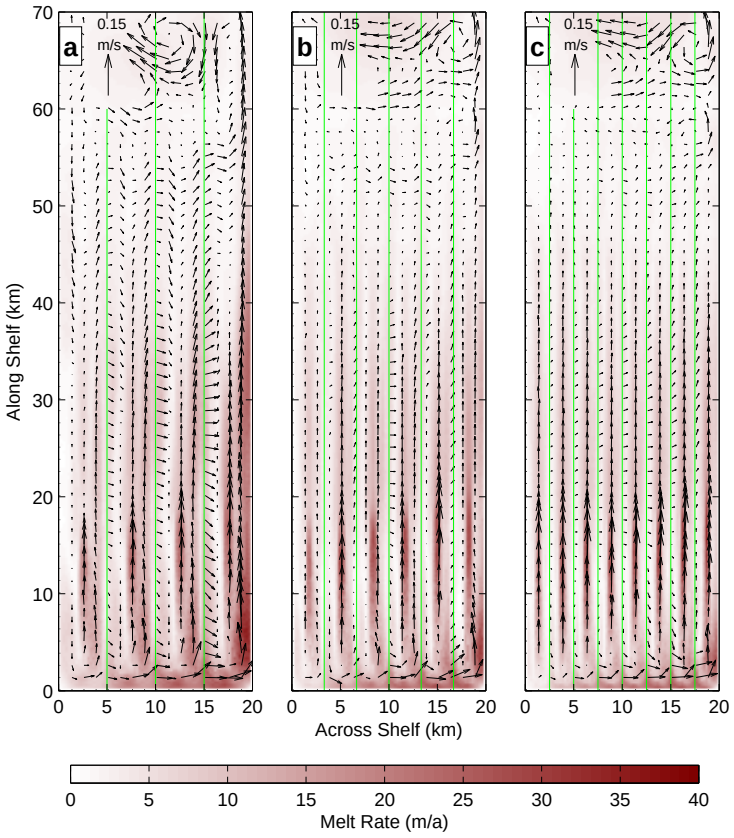

Figure 4.13: Modelled monthly averaged sub-ice layer velocities for 4, 6 and 8 channel cases overlain on monthly averaged basal melt rates (m/a). Vector are shown every 4 grid points. Green lines denote location of channel keels.

Insight into the change in circulation can be gained by varying the horizontal and vertical viscosity values. Figure 4.15 shows the mean melt rates of simulations with 1 to 8 channels for the original prescribed viscosity values along with halved and doubled viscosities. As the viscosity is increased, the change in melting sensitivity to channel number occurs when there are fewer basal channels, likewise when the

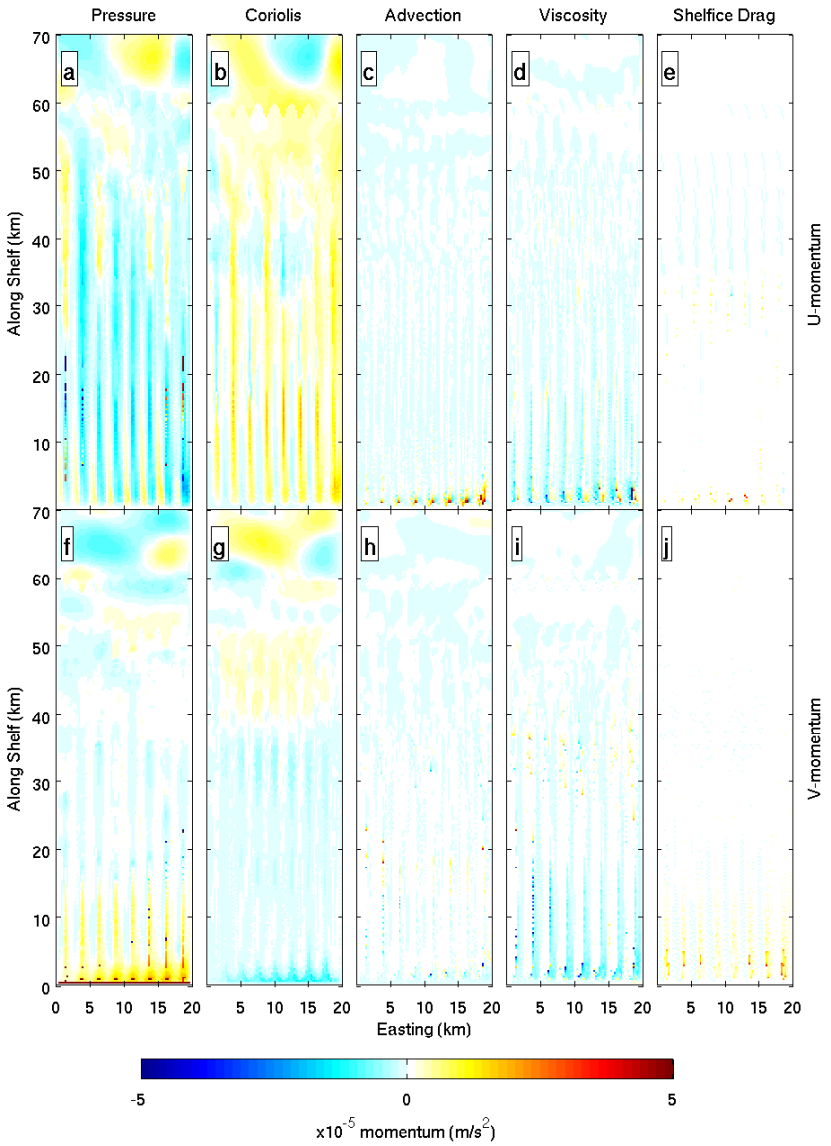

Figure 4.14: Instantaneous momentum terms for 8-channel case. Top row is u-momentum, bottom row is v-momentum.

viscosity is decreased, the change in melting sensitivity occurs when there are more basal channels. This shows that, for a given channel width, there is a viscosity for which the horizontal shear inherent in a geostrophic circulation regime is not permitted; altering the viscosity changes the point at which the flow changes from circulating to overturning. Altering diffusivity was not found to have an effect on the overall pattern and did not change the point at which the mean basal melt rates started to plateau.

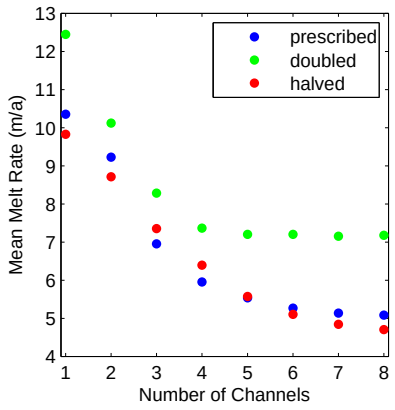

Figure 4.15: Modelled mean basal melt rates for 1 to 8 channels with original prescribed viscosity (blue), halved original viscosity (red) and double original viscosity (green).

It is expected that, for channels narrower than twice than the Rossby radius, the geostrophic circulation will fail, even for low viscosities. However, we find that viscosity also plays an important role in effecting the change between circulations. Viscosity can cause the circulation to change at length scales larger that the Rossby radius by not allowing the shear inherent in the reversing geostrophic regime within the channel. We are unable to separate the two mechanisms as our maximum possible resolution prevents us from properly resolving channels that are narrower than currently considered.

4.3 Discussion

I have used the MITgcm to assess the impact of ice shelf basal channels on ice shelf melting and circulation within an ice-shelf cavity. I find that the inclusion of channels alters the flow of the sub-ice layer beneath the ice shelf, changing the focus and intensity of the melt. In agreement with the findings of *Gladish et al.* (2012), the overall mean melt rate decreases as the number of channels increases. For a small number of larger channels, this sensitivity is high, but for a greater number of smaller channels the sensitivity drops.

For larger channels, a geostrophic flow circulates around the channels. As channels are narrowed, more "no flow" regions are added beneath crests and keels, where isopycnals are flat, whilst geostrophic flow on slopes remains the same. This leads to a decrease in mean mixed layer flow and therefore basal melting.

For narrow channels, this sheared circulation is not viable and is replaced by an overturning circulation. This is much less sensitive to the channel width due to the increase in "no flow" area being smaller, reducing the mean basal melt rate sensitivity to number of channels. Varying the prescribed viscosity changes the number of channels permitted before the circulation changes from a geostrophic circulation to an overturning circulation.

Dutrieux et al. (2013) suggested that basal melt enhances channel features near the grounding line such that they rapidly reach maximum surface expression before thinning towards the ice front. This is in agreement with our modelling results near the grounding line, which suggest strong melting in the steeper section of the channel, and further downstream where melting promotes a widening and shallowing of the channels, also in agreement with the channel profiles seen in the ASTER DEM image.

The presence of basal channels decreases the mechanical stability of an ice shelf (*Rignot and Steffen*, 2008; *Vaughan et al.*, 2012). However the addition of channels

also decreases an ice-shelf's susceptibility to basal melting for two reasons. Firstly, the melting is more evenly distributed, moving away from predominantly beneath the eastern Coriolis-generated boundary current to over more of the ice shelf. Secondly, the mean melt rate decreases for the reasons outlined above. This stabilising effect is a possible explanation as to why basal channels are observed in warm-water ice shelves in Greenland and Antarctica. If the channels stabilise ice shelves, ice shelves with channels are more likely to persist, and a 'survivor bias' makes them more likely to be observed.

There are of course limitations to the model used in this study. Coupled models with an evolving ice shelf are required to test the full impact of the physical processes described here. The profile of the channels is also highly idealised. Nevertheless the principal conclusions are believed to be robust. The findings of this chapter are published as *Millgate et al.* (2013).

Chapter 5

Perturbations to Idealised Domain

This chapter focuses on the changes to both the ice-ocean interactions beneath Petermann Glacier and the conditions within Petermann Fjord for a set of differing scenarios. These scenarios include a change in the stratification of the water column, a seasonal water column signal, warming of the deeper modified Atlantic Water and the calving of large ice-bergs similar to those seen by *Falkner et al.* and *Johannessen et al.* (2011).

In all of the following investigations, the ice shelf and fjord geometry from the idealised four channel case in Chapter 4 were used (Fig. 2.12). The potential temperature and salinity profiles from the same case are used for both model initialisation and restoring on the northern boundary (Fig. 4.1). This forms a base case about which all of the following investigations are perturbed. All model parameters are kept consistent with those in Section 4.1 unless otherwise specified. Likewise, all results shown are monthly averages obtained after the model was spun up to a steady state over a period of 5 years unless stated otherwise. A spin up period of 5 years, with a 60 second time step, was chosen for consistency with the results of Chapter 4, to allow for reliable comparison with the chosen base case.

5.1 Impact of a deepening of the stratified layer

5.1.1 Introduction

With the Arctic experiencing lower levels of sea-ice cover (*Serreze et al.*, 2007), it is possible that Petermann Fjord could spend longer periods of the year ice-free. This would allow the wind within the fjord to have a larger mixing effect on the surface stratified layer of the open ocean sections of the fjord.

This enhanced mixing could lead to a deeper, yet more weakly surface stratified layer, which could impact the circulation beneath the ice shelf and hence the ice-ocean interactions. Conversely if the winds in the area were to die down or there be a change in sea-ice cover trend, the surface stratified layer could become shallower and more strongly stratified.

To investigate the potential changes in ice-ocean interactions and fjord oceanography due to a changing of the surface stratified layer, four perturbations around the base case (stratification depth of 100 m) were run. The stratification depth is defined as the point in the water column above which the water column is stratified and beneath which the water column is homogenous. In all of the perturbations, the potential temperature and salinity values at the surface and at depth remain constant, with the depth over which the stratification occurs varied. One perturbation reduced the stratification depth to 50 m, whilst the remaining 3 perturbations increased the stratification depth to 250 m in 50 m intervals. The stratification was varied in both the potential temperature and salinity profiles. Figure 5.1 shows the salinity and potential temperature profiles for both the initial conditions and restoring on the northern boundary.

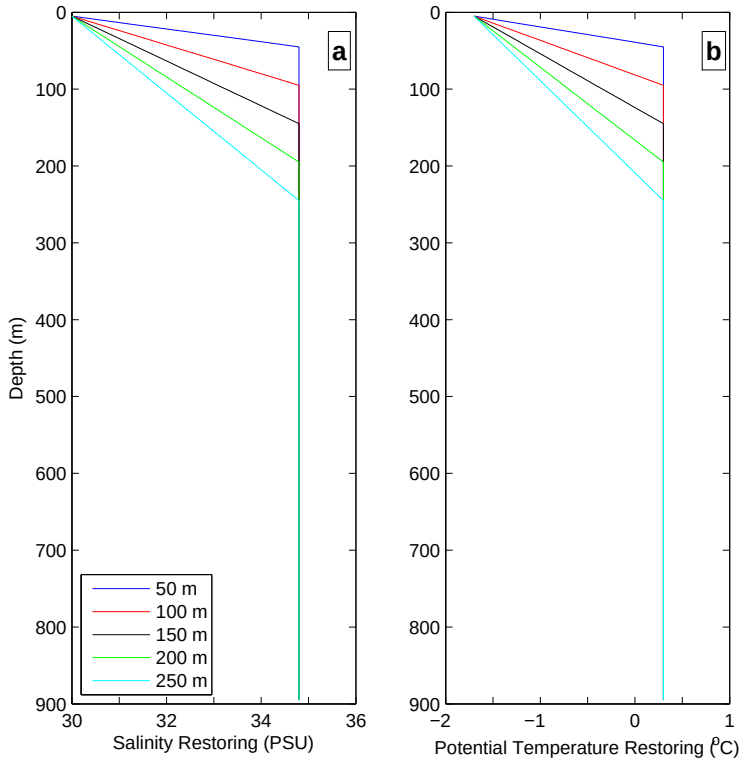

Figure 5.1: a) Salinity and b) Potential Temperature profiles used as initial conditions and restoring at the northern boundary for stratification depths of 50 m (dark blue), 100 m (red), 150 m (black), 200 m (green) and 250 m (cyan).

5.1.2 Results

5.1.2.1 Basal Melting

Figure 5.2 shows the monthly average sub-ice layer velocities overlain on monthly averaged basal melt rates (m/a). A dark red color represents high level of basal melting whilst white represents no basal melting. It can be seen that decreasing the stratification depth to 50 m (Fig. 5.2a), shallower than the minimum draft of the ice shelf (60 m), caused basal melting to extend to the ice front, further downstream than in the base case (Fig. 5.2b). It can also be seen that as the stratification depth is increased (Fig. 5.2 c-e) the distance to which basal melting extends downstream of the grounding line decreases. The pattern of flow within the sub-ice layer is the same as that described in Section 4.2.2, with flow constrained within the channels.

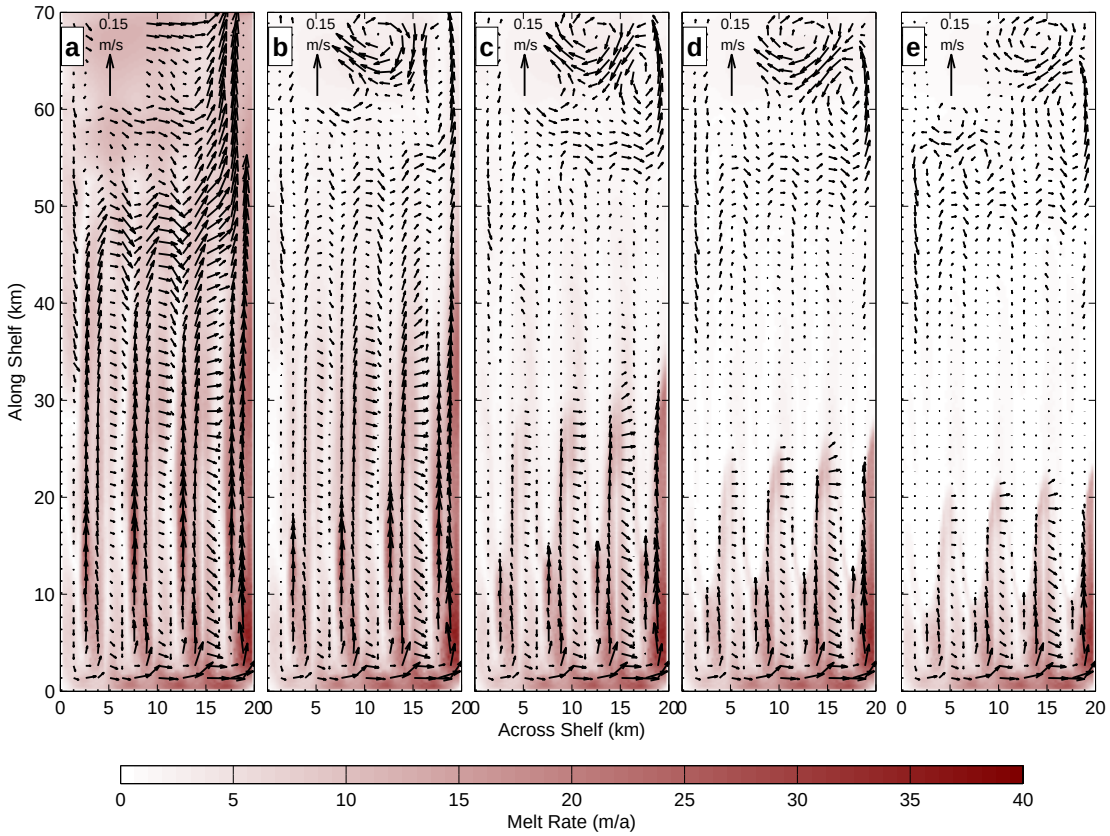

Figure 5.2: Modelled monthly averaged sub-ice layer velocities (m/s) for a) 50 m, b) 100 m, c) 150 m, d) 200 m and e) 250 m stratification depths overlain on monthly averaged basal melt rates (m/a). Vectors are shown every 5 grid points.

The flow is strongest and extends further along the eastern boundary of the domain in the case where the stratification depth is 50 m. Both the strength and extent of the boundary flow decreases as the stratification depth is increased. Close to the grounding line the pattern and magnitude of both basal melting and ocean surface flow is relatively consistent across all 5 scenarios.

Increasing the stratification depth leads to a decrease of the mean melt rate, with the sensitivity decreasing as the stratification depth increases (Fig. 5.3a). As the stratification depth increases, the melt area (area of the ice shelf beneath the stratification depth) decreases in a non-linear fashion, due to the non-linear geometry chosen for the ice shelf.

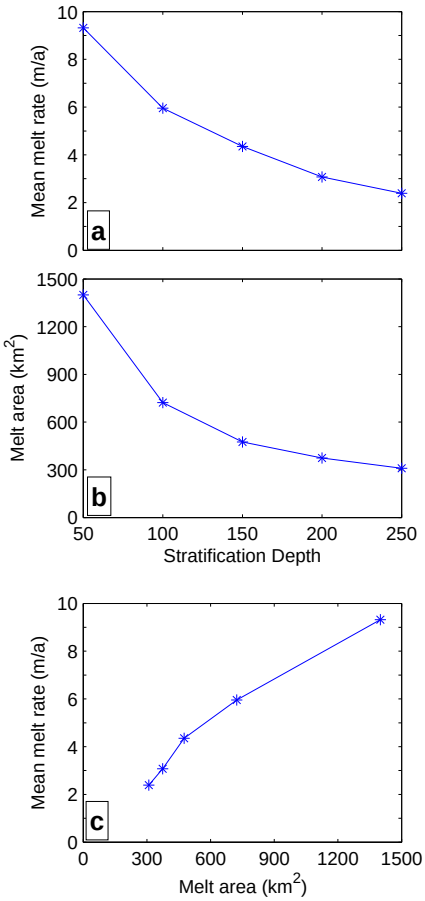

Figure 5.3: a) Relationship between mean melt rate and stratification depth, b) relationship between melt area and stratification depth, c) relationship between mean melt rate and melt area.

Figure 5.3c shows a near linear relationship, indicating that the reduction in melt area is the primary driver behind the reduction in mean melt rate. The stratification depth was chosen as the cut off for melt area, due to the sharp gradient in potential temperature at this depth. This leads to a large difference in $T - T_b$ either side of the pycnocline depth, and therefore a large difference in expected basal melt rates.

5.1.2.2 Fjord Circulation

Within the fjord there is the same geostrophic circulation as seen in Chapter 4, with warm modified Atlantic Water being brought into the cavity beneath the ice shelf

along the western boundary of the domain, and a return flow, transporting water out of the cavity, along the eastern boundary (Fig. 5.4).

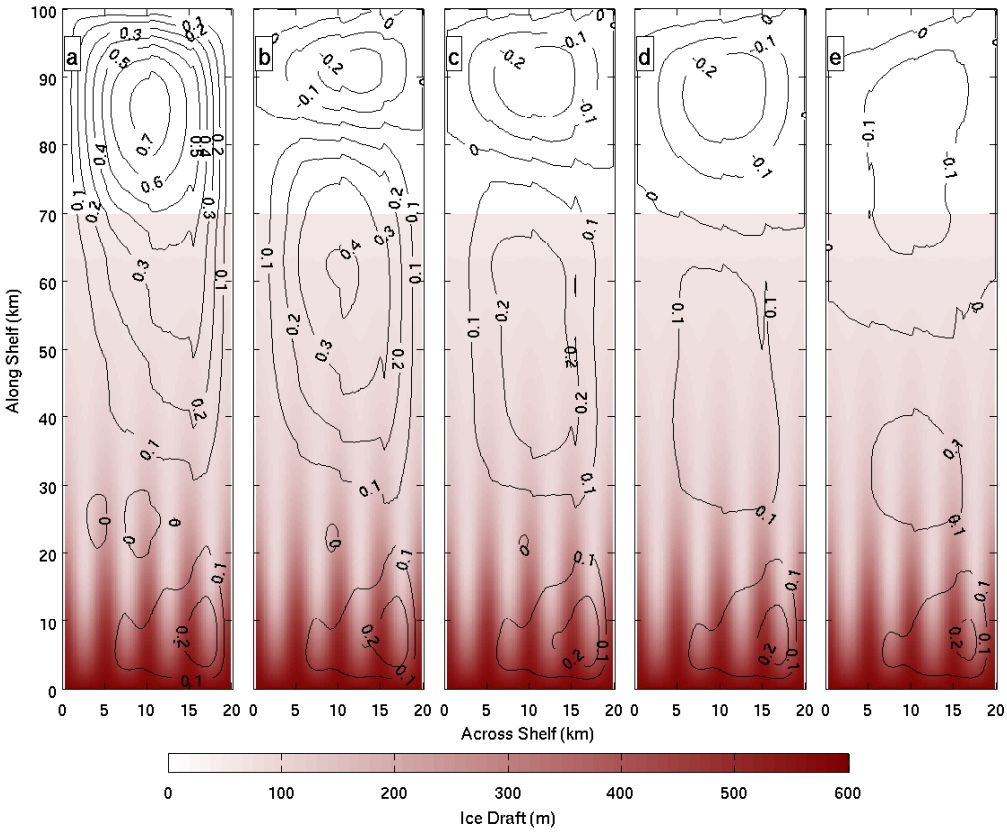

Figure 5.4: Barotropic stream function (contours) overlying ice draft (colored) for a) 50 m, b) 100 m, c) 150 m, d) 200m, e) 250 m stratification depth.

It can be seen from Figure 5.4 that the circulation is strongest for the scenario with a 50 m stratification depth due to the largest levels of basal melting. It can also be seen that as the stratification depth is increased, the strength of the barotropic stream function is decreased in tandem with the reduction in buoyancy forcing from basal melting. As the cyclonic circulation decreases from its maximum strength in the 50 m scenario, it also decreases in extent, so that the northern edge of the circulation moves away from the northern boundary.

In its place an anticyclonic circulation forms in the open ocean section of the fjord as in Section 4.2.1. In the base case, the anticyclonic circulation is about half as strong as the cyclonic circulation and is only 20 km in size compared to the 50 km

size of the cyclonic circulation. As the stratification depth increases, the strength of the anticyclonic circulation decreases. However the cyclonic circulation weakens at a faster rate and, by a stratification depth of 200 m, the anticyclonic circulation has become stronger than the cyclonic circulation. The anticyclonic circulation also becomes larger than the cyclonic circulation and protrudes underneath the ice shelf. It should be noted that this fjord mouth circulation may not be realistic since this is a closed domain, unlike Petermann Fjord which opens into Hall Basin. This will be investigated in Chapter 6.

The overturning circulation due to melting at the ice base introducing a source of cold, fresh buoyant water, as seen Chapter 4, is also present in these scenarios, however its structure is slightly altered (Fig. 5.5 and 5.6), see below.

5.1.2.3 Water Properties

The path of the buoyant meltwater layer formed when the warm modified Atlantic water interacts with, and melts, the ice is apparent from the North-South sections of salinity and potential temperature anomalies (Fig. 5.5 and 5.6). These figures show the difference between the modelled salinity and potential temperature profiles at the end of the model run and their corresponding initial conditions. Negative values mean that the water is fresher / cooler respectively than the initial water condition.

The meltwater is cooler and fresher than the initial deep water and flows up the base of the ice shelf, within the channels, until it reaches a level of neutral buoyancy, where it detaches from the ice shelf base and flows northwards away from the ice shelf (denoted by the strong negative values in Fig. 5.5 and 5.6). These figures show that the depth at which the meltwater finds neutral buoyancy, and hence detaches from the ice base, is dependent on the stratification of the water column. Where the water column has a deeper stratification layer, the meltwater detaches deeper, and hence closer to the grounding line (Fig. 5.5d), whilst for a shallower stratification

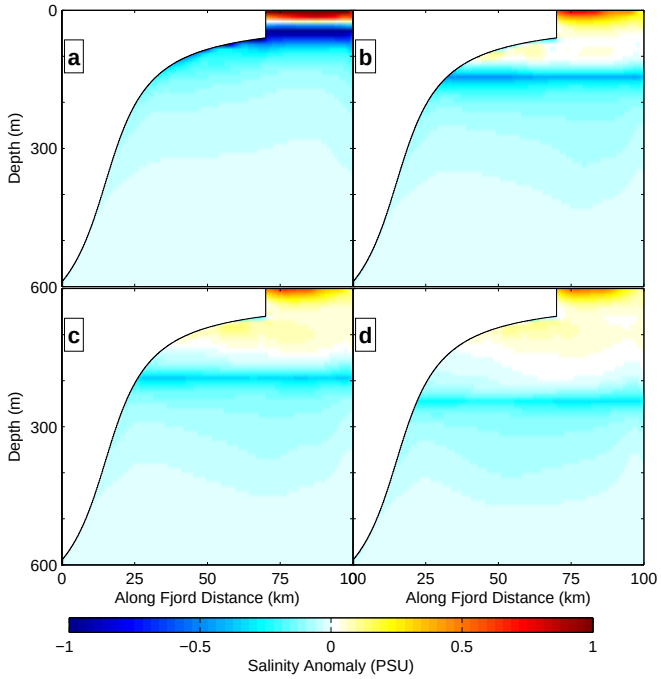

Figure 5.5: Salinity anomaly profiles along the central keel for a) 50 m, b) 150 m, c) 200 m, and d) 250 m stratification depth.

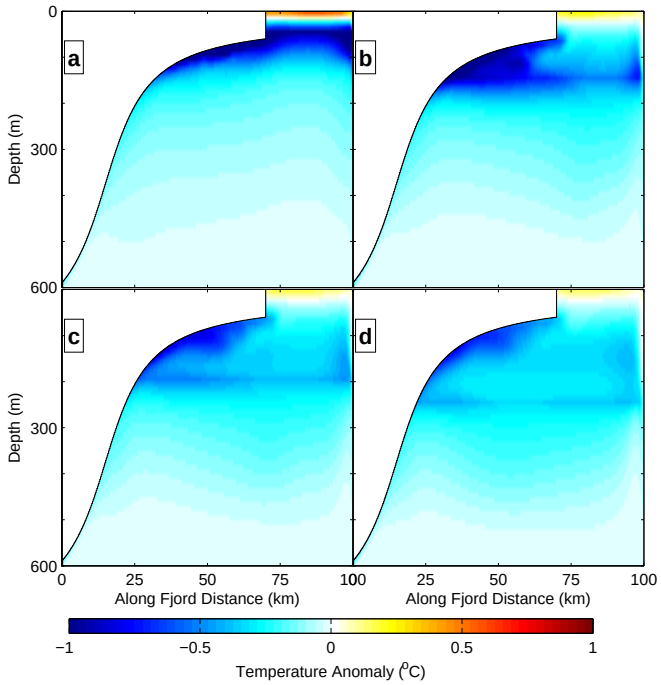

Figure 5.6: Potential temperature anomaly profiles along the central keel for a) 50 m, b) 150 m, c) 200 m, and d) 250 m stratification depth.

depth, the meltwater detaches from the ice base closer to the surface and therefore closer to the ice front (Fig. 5.5a). The point at which the meltwater detaches from the ice base corresponds with the distance to which basal melting extends from the grounding line.

There is an inherent frictional velocity, u_*, on the base of the ice shelf from the meltwater flow. This frictional velocity plays an important role in basal melting, as shown in Chapter 4. By detaching from the ice base, this frictional velocity is removed, leading to a decrease in basal melt rates. As the detachment occurs deeper in the water column as the stratification depth increases, the meltwater detaches from the ice shelf closer to the grounding line, meaning there is a larger portion of the ice shelf with lower melt rates. This is the main driver for the reduction in basal melt rates.

5.1.3 Discussion

The surface stratified layer of the ocean column in Petermann Fjord acts as a protective layer to the base of the ice shelf. The meltwater layer, caused by melting of the deeper sections of the ice shelf, detaches from the ice base and flows along the pycnocline. Therefore any ice above this depth is insulated from the friction velocity that is inherent with this flow, and also from the warmer water that this flow entrains. *Holland and Jenkins* (1999) and *Holland et al.* (2008b) showed that to a good level of approximation (and neglecting heat conduction), that melt rate is proportional to the product of friction velocity, u_*, and thermal driving from entrained warm water, $(T_B - T_M)$, therefore by protecting the ice base from these two factors, little or no melting of the ice base occurs.

If the stratified layer of Petermann Fjord were to deepen, the area near the ice front that is shallower than the stratified layer will increase. As ocean flow and basal melt rates are not dependent on melting downstream, the interactions near the

grounding line remain constant, resulting in a decrease in both ice shelf mean melt rate and strength of ocean circulation. As melt rates decrease at a greater depth, it is possible that the ice shelf could thicken near the ice front, with the potential of increasing the stability of the ice shelf to calving and lead to an advancement of the ice front.

If Petermann Fjord were to tend towards a period of time with prolonged ice-free conditions, assuming oceanic temperature and salinity remain constant, then it is possible for the ice shelf to begin to thicken due to a reduced level of basal melting near the ice front, potentially leading to the ice shelf becoming stronger and growing in length. However this is dependent on the mechanisms which control calving, such as ice front undercutting.

The assumption of constant oceanic temperatures is likely to be invalid. Ice free conditions will decrease the albedo, leading to an increase in the absorbtion of solar energy. This could lead to an increase in surface temperatures, which could be mixed through the surface stratified layer. This would increase the thermal forcing $(T - T_b)$ in the surface stratified layer, with the potential to lead to increased melt rates above the pycnocline, negating the impact of a deepening pycnocline.

However it is more plausible that the stratification will vary on a seasonal basis with the input of freshwater in the summer, due to seasonal glacier melt, and the growth of a winter mixed layer at the surface of the water column, affecting the temperature and salinity profiles. The following section investigates the impacts of a seasonal signal in fjord temperature and salinity, and how changes in this signal could impact upon Petermann Glacier and Fjord.

5.2 Impact of Seasonal Restoring

5.2.1 Introduction

It has been seen in Section 5.1 that the surface stratified layer insulates the ice shelf from the meltwater layer and hence limits basal melting for the insulated area. There are several factors which affect the depth and strength of stratification including freshwater run-off from land melt, sea-ice cover and wind conditions.

During the winter season, Nares Strait experiences full sea-ice cover. During sea ice formation, brine is rejected into the surface layer, increasing its density, causing convection within the water column and the formation of a homogenous surface layer (the surface mixed layer). This layer can be caused by either local sea-ice formation or can advected into the strait from sea-ice formation in the Arctic. Within Nares Strait this layer has a base between 100 and 135 m, which, after advection into Petermann Fjord, allows it to intrude underneath the ice shelf and into the channel crests (*Johnson et al.*, 2011).

Such an intrusion was seen by *Rignot and Steffen* (2008) when drilling through the crest of the most easterly channel approximately 15 km downstream of the grounding line of Petermann Glacier. Figure 5.7 shows the potential temperature and salinity profiles of the through ice CTD casts. The surface mixed layer can be seen as the vertical section of the profiles between depths of approximately 60 and 100 m.

The presence of this layer in the winter means that the profile of the water entering the fjord from Nares Strait varies on a seasonal basis. Such a seasonal signal can be implemented in the MITgcm by introducing a surface mixed layer into the restoring profiles, with the depth of the mixed layer varying sinusoidally throughout the year.

To investigate the effect of such a seasonal signal, three different seasonally-varying scenarios were investigated, one following observation of *Johnson et al.* (2011), one with a deeper surface mixed layer maximum, and one investigating the

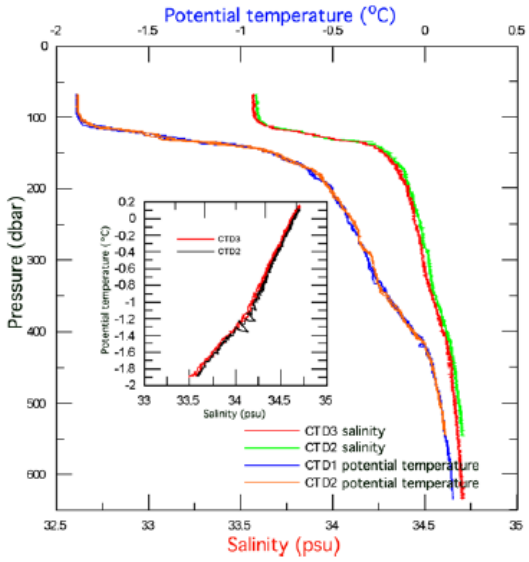

Figure 5.7: Through ice profiles of salinity and potential temperature approximately 15 km downstream of the grounding line. The inset shows the $\Theta - S$ diagram. (Source: *Rignot and Steffen* (2008)).

impact of an extended winter. In each scenario the depth of the mixed layer varies sinusoidally, whilst the thickness of the pycnocline beneath remains constant at 100 m. The temperature profile varies by simply moving the surface stratified layer up and down by the prescribed mixed layer depth. Repeating this for salinity would produce the counterintuitive result that the deepest winter mixed layer would have the greatest freshwater content. The salinity profiles are therefore adjusted such that the total salt content of the water column remains constant throughout the year.

The first seasonally-varying scenario is based upon the maximum surface mixed layer depth reported by *Johnson et al.* (2011). The mixed layer depth is set to vary between a minimum of 0 m in the summer and a maximum of 140 m in the winter. The salinity profile consists of three sections; the mixed layer with a depth of d and a salinity s_{ML}, the pycnocline which has a depth of 100 m and a slope of $\frac{(34.8-s_{ML})}{100}$ psu m^{-1} and finally the deep homogenous layer with a salinity of 34.8 psu (Fig. 5.8). The total salt content was calculated from the salinity restoring profile used in

Chapter 4 as this is the prescribed profile when the mixed layer depth is 0 m.

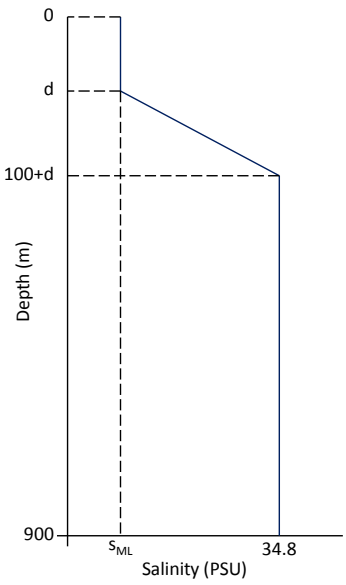

Figure 5.8: Profile used to determine mixed layer depth and salinity for seasonal restoring.

Given the mixed layer depth, the salinity of the surface mixed layer can be found by balancing the depth integrated salinity of the whole water column, with the depth integrated salinity for the surface mixed layer, stratified layer and deep modified Atlantic Water layer.

Using this balance the restoring profiles for the scenario where the surface mixed layer has a maximum depth of 140 m is shown in Figure 5.9. Due to the sinusoidal nature by which the mixed layer depths varies with time, the restoring profiles for August and June are identical, as are the profiles for September and May and so forth. July (height of summer) and January (the height of winter) are the only months to have restoring profiles which are distinct from any other month.

The second scenario maintains the same sinusoidal nature and increases the maximum depth of the surface mixed layer to 200 m, whilst the third scenario encompasses an extended winter. This was achieved by setting the depth of the mixed layer to 150 m for the three winter months (December, January and February), whilst the

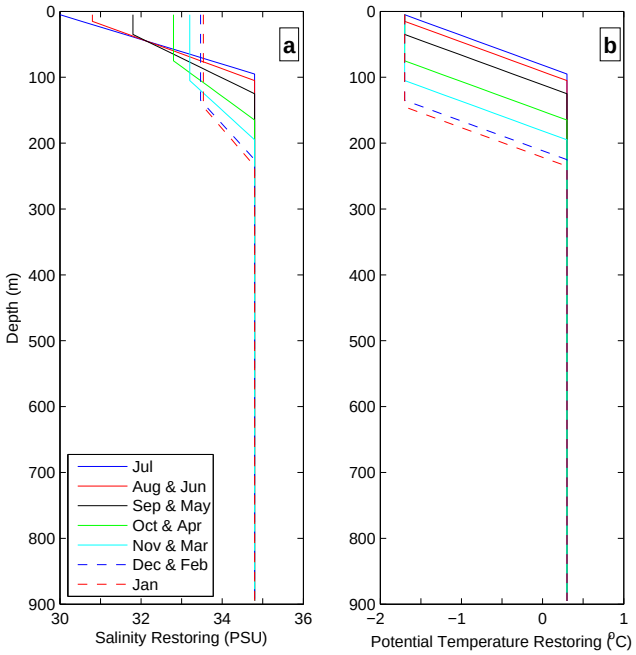

Figure 5.9: a) Salinity and b) Potential Temperature monthly restoring profiles for the 140 m mixed layer scenario.

remaining 9 months followed the sinusoidal pattern for mixed layer depth.

Each scenario is spun up for 5 years, with the January profiles used for initial conditions and the first restoring on the northern boundary. Following this the restoring profiles changed on a monthly basis for the duration of model spin up.

5.2.2 Results

5.2.2.1 Basal Melting and Water Properties

Figure 5.10 shows the mean melt rate and sub-ice layer flow pattern for the months of July and January, along with the difference between these melt rates. A positive difference indicates that more melting occurred during July than January. Sub-ice layer flow and melt rate patterns follow those described in Chapter 4. During July, when there is no mixed layer, melting extends 40 km downstream from the grounding line beneath the eastern boundary current. In January, when the surface

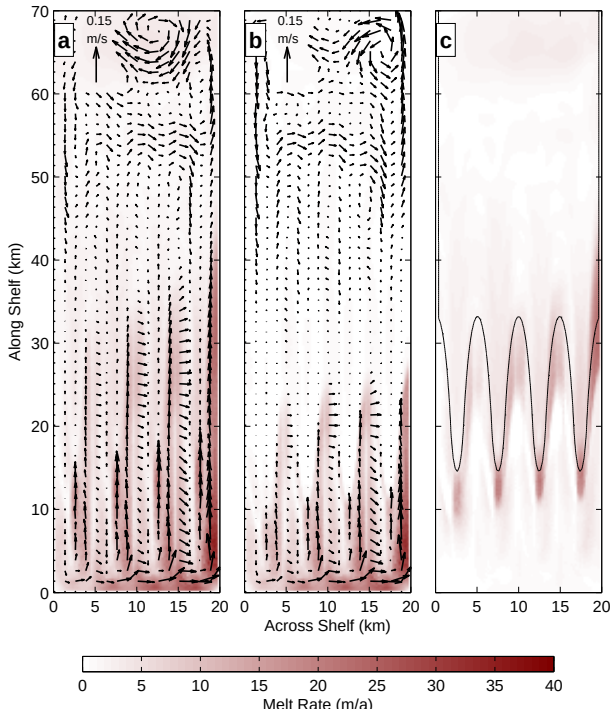

Figure 5.10: Melt rates (m/a) and sub-ice layer flow patterns (m/s) during a) January and b) July for the 140 m surface mixed layer scenario. c) shows the difference in melt rates (m/a) between July and January. The 140 m ice draft contour is shown in black.

mixed layer is at its maximum, the melting under the boundary current only extends approximately 26 km downstream from the grounding line. The difference in melt rates appear to be just deeper than the 140 m (maximum mixed layer depth) ice draft contour (Fig. 5.10c). The melt rate difference is greatest just beneath the maximum mixed layer depth as the mixed layer flows away from the ice base along the stratified layer, which extends from 140 m to 240 m during the winter.

This change in melt rate patterns can be explained when looking at the salinity and potential temperature (Fig. 5.11) sections for July and January. The differences for represent the July - January difference with a positive value meaning that the water was warmer and saltier in July. In summer (July) a cool and fresh layer is confined to the surface layer (Figs. 5.11a/d). In winter (January) there is a layer of cooler and relatively fresh water protruding underneath the ice shelf. This layer insulates the ice shelf from the meltwater plume in winter, similar to that seen

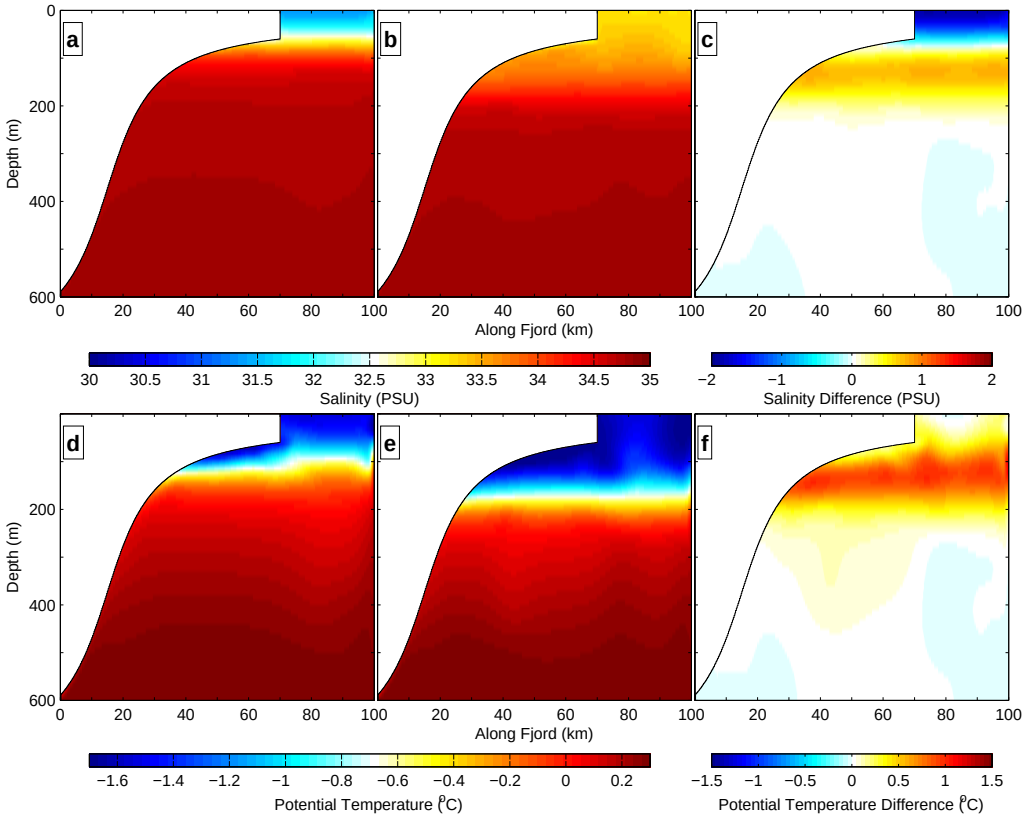

Figure 5.11: Salinity sections down the centre of the domain for the 140 m mixed layer scenario during a) July and b) January. c) July - January difference and Potential temperature sections down the centre of the domain during d) July and e) January. f) July - January difference.

in Section 5.1. Similar melt differences and changes in potential temperature and salinity are seen, but not shown, for the 200 m and extended winter scenarios.

The monthly melt rates follow the same pattern throughout the year for each of the three mixed layer scenarios (Fig. 5.12). For each case the maximum melt rate is reached during July and the minimum during January, with the melt pattern following the sinusoidal pattern of the restoring profiles. The 140 m surface mixed layer scenario has the highest maximum melt, whilst the 200 m scenario has the lowest maximum melt rate. The three-month extended winter has a more constant winter (DJF) minimum melt rate than the other two scenarios, however due to the shape of a sinusoid, the winter melt rates of each scenario have a degree of consistency

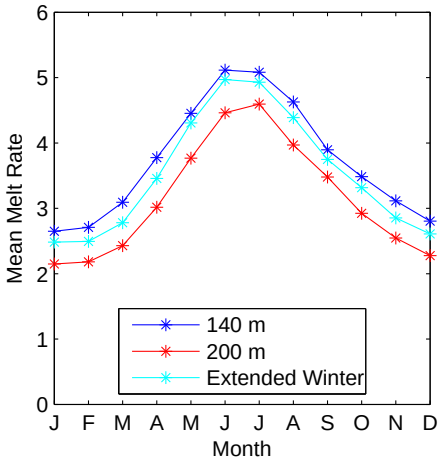

Figure 5.12: Monthly mean melt rates (m/a) for the 140 m (dark blue), 200 m (red) and extended winter (cyan) scenarios.

across these months. The mean annual melt rate was 3.73 m/a for the 140 m scenario, 3.15 m/a for the 200 m scenario and 3.53 m/a for the extended winter scenario.

5.2.2.2 Fjord Circulation

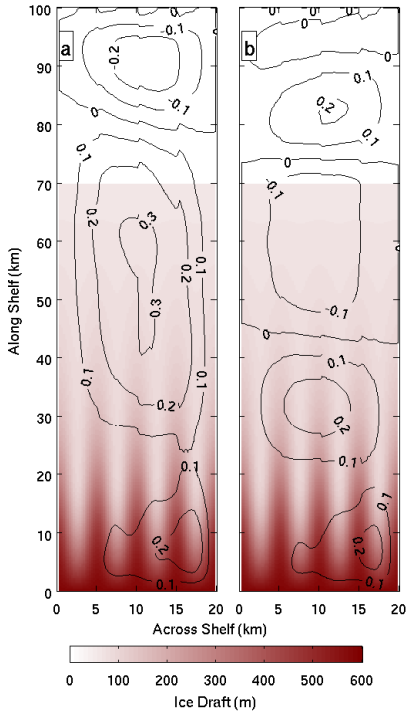

Figure 5.13: Barotropic stream function (contours) overlying ice draft (colored) for the 140 m mixed layer scenario during a) July and b) January.

The barotropic flow within the fjord during July and January for the 140 m mixed layer scenario is shown in Figure 5.13. The cyclonic circulation is strongest during July with a slightly weaker anticyclonic circulation within the open ocean section of the fjord. During the winter the cyclonic circulation reduces both in strength and extent, with a further cyclonic and anticyclonic circulation forming within the fjord. The reduction in strength of the circulation is caused by the same mechanism as explained in Chapter 4, i.e. lower melt rates lead to a reduction in buoyancy input and therefore a reduction in circulation. A similar change in circulations seen in the 140 m scenario is seen in both of the other scenarios. The strength of the circulation is weakest in the 200 m scenario and strongest in the 140 m scenario. This is due to the relative levels of basal melting and freshwater flux for each scenario.

5.2.2.3 Sub Ice-Shelf Mixed Layer

Investigation of the potential temperature and salinity profiles beneath the ice shelf allows for the identification of a mixed layer as seen by *Rignot and Steffen* (2008). Figure 5.14 shows these profiles for the 140 m scenario. The profiles are taken from the centre of the most easterly channel, at a distance of 50 km from the grounding line. This distance was chosen as the ice thickness is similar to that of the ice at the drill site of *Rignot and Steffen* (2008).

It can be seen that although there are the beginnings of the mixed layer in the potential temperature profiles, especially in the January profile, this is not present in the salinity profile. However the top of the water column has similar potential temperature and salinity values as the profile of *Rignot and Steffen* (2008). This suggests that perhaps the mixed layer does not extend deep enough into the water column in the open-ocean forcing. Similar salinity and potential temperature profiles, taken at the same location, were found for the 200 m mixed layer scenario.

As deepening the mixed layer in the restoring profile on the northern boundary

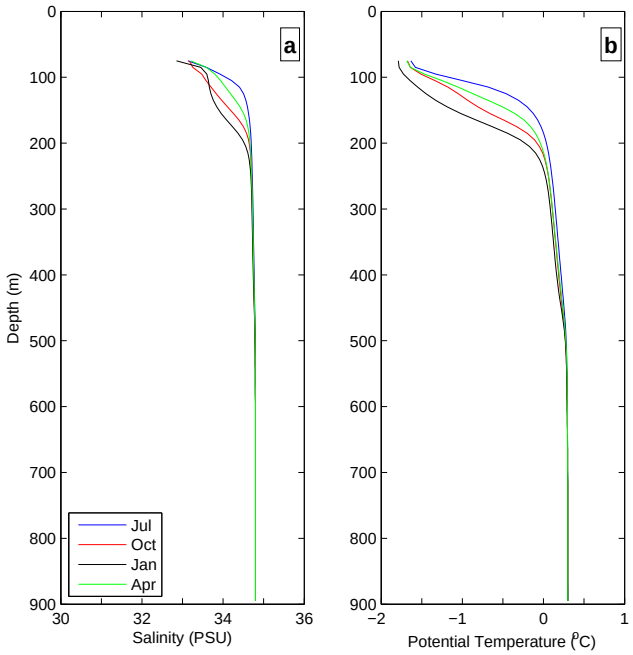

Figure 5.14: Seasonal a) salinity and b) potential temperature profiles for the 140 m scenario, from the centre of the eastern channel 50 km downstream of the grounding line.

did not result in the presence of a mixed layer, this suggests that a longer winter may be needed. Figure 5.15 shows the salinity and potential temperature profiles, taken at the same location, for the extended winter scenario. These profiles show the same features as the previous two scenarios, similar under ice potential temperature and salinity values, but do not indicate the presence of the winter mixed layer as observed by *Rignot and Steffen* (2008).

5.2.3 Discussion

Restoring to a seasonally varying surface mixed layer has had the effect of introducing an 'insulating' layer underneath the ice shelf, similar to that seen in Section 5.1. As the insulating layer moves up and down with the predefined restoring profile, less/more of the ice shelf is insulated, resulting in higher/lower levels of mean basal melting. The insulative layer for the 200 m mixed layer scenario extends deeper into

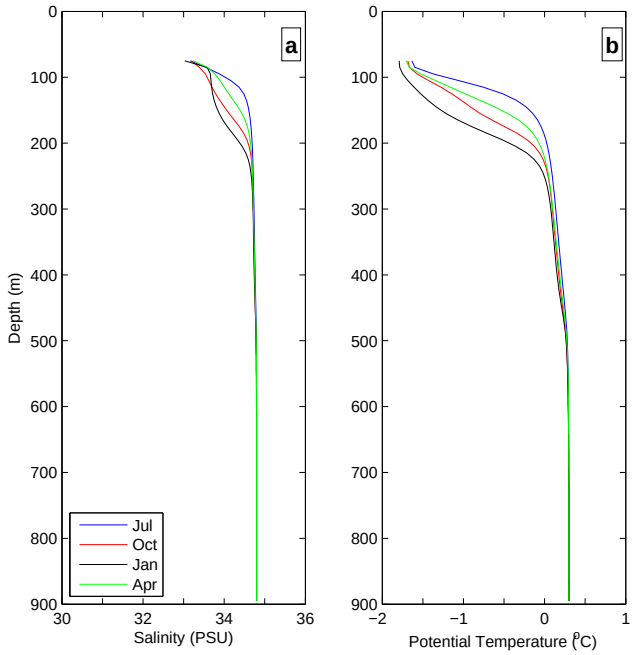

Figure 5.15: Seasonal a) salinity and b) potential temperature profiles for the extended winter scenario, from the centre of the eastern channel 50 km downstream of the grounding line.

the water column than the 140 m mixed layer scenario. This results in the ice shelf being insulated to a greater degree from the meltwater plume, leading to lower basal melt rates.

Even though the prescribed mixed layer depth follows a sinusoidal pattern, the monthly mean melt rates do not follow this pattern precisely. When comparing the same mixed layer depths in spring and summer, the monthly mean melt rate are not the same, with the spring month having a lower mean melt rate. This is due to the spring month following a month with a deeper, cooler mixed layer, whilst the autumn month follows a month with a shallower, warmer mixed layer. The lag in the restoring conditions permeating underneath the ice shelf means that the autumn month still feels some of the warmer water from the previous restoring, whilst the spring month still feels some of the cooler water from its previous restoring, leading to lower melt rate in the spring.

In the three scenarios investigated here, it was not possible to detect the protruding mixed layer as seen by *Rignot and Steffen* (2008) in their through ice CTD casts. This could be due to the chosen salinity profiles used for restoring which could be too saline at the surface, have a too shallow surface mixed layer, or do not have a long enough winter.

It is also possible that the mixed layer detected by *Rignot and Steffen* (2008) could be from another source, such as meltwater crossing the grounding line, mixing with ocean water and rising to the base of the ice shelf, or surface meltwater permeating through cracks in the ice shelf, as suggested by *Johnson et al.* (2011). The mixed layer observed by *Rignot and Steffen* (2008) could also be a remnant from a year in which there was a particularly deep, or long lived, surface mixed layer, which has persisted under the ice shelf.

5.3 Impact of warming subsurface waters

5.3.1 Introduction

Ocean warming has been hypothesized as a cause of glacial destabilisation (*Holland et al.*, 2008a; *Christoffersen et al.*, 2011; *Hanna et al.*, 2009; *Murray et al.*, 2010; *Rignot et al.*, 2010), and model studies have shown ocean warming to enhance subaqueous melting (*Holland et al.*, 2008b; *Xu et al.*, 2012). The disintegration of Jakobshavn Isbræ's ice shelf, the last remaining ice shelf in Greenland's low latitudes (*Weidick et al.*, 2004), has been attributed to the arrival of relatively warm water originating in the Irminger Sea (*Holland et al.*, 2008a). A similar source of warm water has been suggested as the cause of glacial acceleration on the eastern coast of Greenland (*Howat et al.*, 2008; *Straneo et al.*, 2010; *Christoffersen et al.*, 2011).

Rignot et al. (2012) have modelled the spread of warm water around Greenland and found that warm water can quickly propagate into glaciated fjords and these

waters are very likely to increase subaqueous melt rates. *Rignot et al.* (2012) found that the warming signal is spreading to the northwest sector of Greenland, with a modelled increase of 0.4 °C in temperature of modified Atlantic Water within Petermann Fjord during the 2003-2009 period. This is slightly larger than the value of 0.25 °C reported by *Johnson et al.* (2011) over the same time period. If Petermann Glacier was to follow the trend seen in southern and eastern Greenland, this increase in ocean temperature may lead to an increase in basal melting, glacier acceleration and ice shelf instability.

To investigate the impact of sub-surface ocean warming, a suite of experiments was completed. The suite consisted of the base case, three warming scenarios ranging from an increase of 0.3 °C in line with *Johnson et al.* (2011) and *Rignot et al.* (2012) to a warming of 0.9 °C and seven cooling scenarios ranging from a cooling of 0.3 °C to a cooling of 2.0 °C. The final cooling scenario results in the temperature being homogeneous at −1.7 °C throughout the whole water column. The cooling scenarios were included so that the relationship between temperature and melt rate could be inferred. The salinity profile remained constant throughout all of the warming and cooling scenarios. Figure 5.16 shows the salinity profile and the eleven temperature profiles used for restoring at the northern boundary and as the model initial conditions.

5.3.2 Results

5.3.2.1 Basal Melting

Figure 5.17 show the mean melt rates and sub-ice layer flow patterns for two warming scenarios (+0.9 and +0.3 °C), the base case and one cooling scenario (−0.3 °C). It is apparent that as the temperature of the deep modified Atlantic Water warms, basal melt rates at depth are increased. This leads to an increase in the buoyancy of the sub-ice layer flow, causing it to speed up. This increase in flow speed, along with an

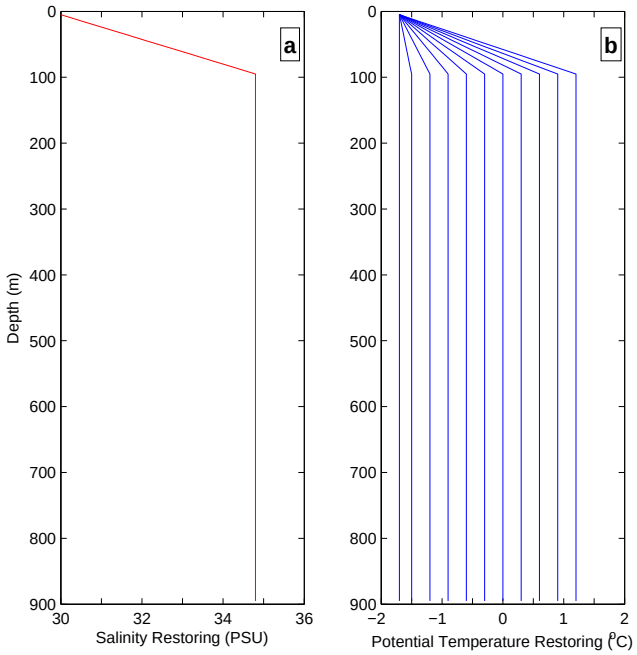

Figure 5.16: a) Salinity and b) potential temperature restoring profiles for the eleven warming and cooling scenarios.

increase in thermal forcing, leads to higher melt rates downstream of the grounding line. The increase in deep water temperature does not lead to a change in the melt rate pattern or the flow pattern of the sub-ice layer.

Figure 5.18a) shows the relationship between the potential temperature of the modified Atlantic Water and the mean melt rate. The relationship is positive, as described above, and quadratic (R^2=0.99) in agreement with *Holland et al.* (2008b). As the deep waters warm, the mean thermal forcing ($T - T_b$) supplied to the base of the ice shelf from the ocean also increases (Fig. 5.18b), as does the mean friction velocity (u_*) (Fig. 5.18c). The quadratic increase seen in mean melt rate is caused by the increase in both the mean thermal forcing and mean friction velocity, caused by the increase in deep water potential temperature, as, to a good level of approximation, the melt rate is proportional to the product of these two factors (*Holland and Jenkins*, 1999; *Holland et al.*, 2008b).

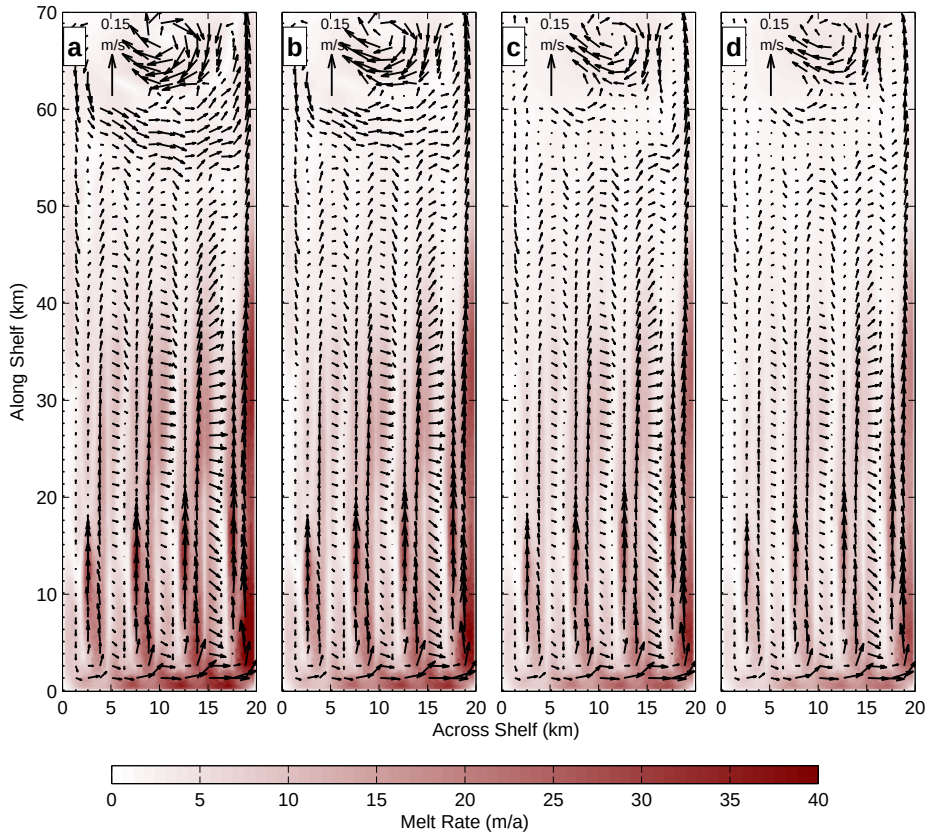

Figure 5.17: Melt rates (m/a) and sub-ice layer flow patterns (m/s) for a temperature difference of a) +0.6 °C, b) +0.3 °C, c) +0 °C and d) −0.3 °C.

5.3.2.2 Fjord Circulation

The increase in both melt rates and sub-ice layer flow speed with warming as seen above is also evident in the barotropic streamfunction (Fig. 5.19). As the potential temperature is increased, the strength of the cyclonic circulation increases, as does its extent, whilst the anticyclonic circulation near the northern boundary decreases in both strength and extent. This is due to the buoyancy force beneath the ice shelf increasing, caused by an increase in melt rates as the deep waters warm. Conversely, as the potential temperature is decreased, the buoyancy force is reduced, due to lower levels of basal melting. This results in a weaker, small cyclonic circulation and a growth of the anticyclonic circulation. As the temperature of the deep water cools

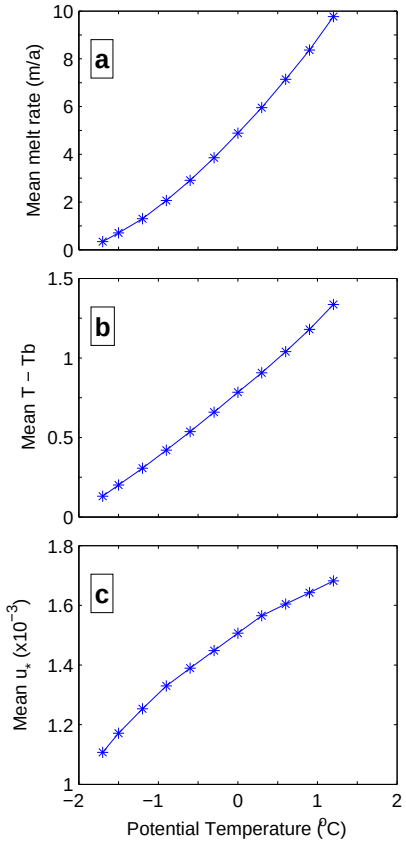

Figure 5.18: Relationship between deep water potential temperature and a) mean melt rate, b) mean $(T - T_b)$ and c) mean u_*.

to that of the surface waters, basal melting is severely reduced, resulting in a much smaller buoyancy flux, leading to little or no sub-ice layer flow or circulation within the fjord.

5.3.2.3 Water Properties

Figure 5.20 shows the potential temperature and salinity anomalies for scenarios with a temperature difference of $+0.9\,^{\circ}\mathrm{C}$, $0\,^{\circ}\mathrm{C}$, and $-0.9\,^{\circ}\mathrm{C}$ respectively. In all cases the meltwater layer detaches from the base of the ice shelf and flows along the pycnocline. It can be seen that the salinity anomaly is stronger for the warming scenario and weakest for the cooling scenario. This is due the warmer waters causing greater levels

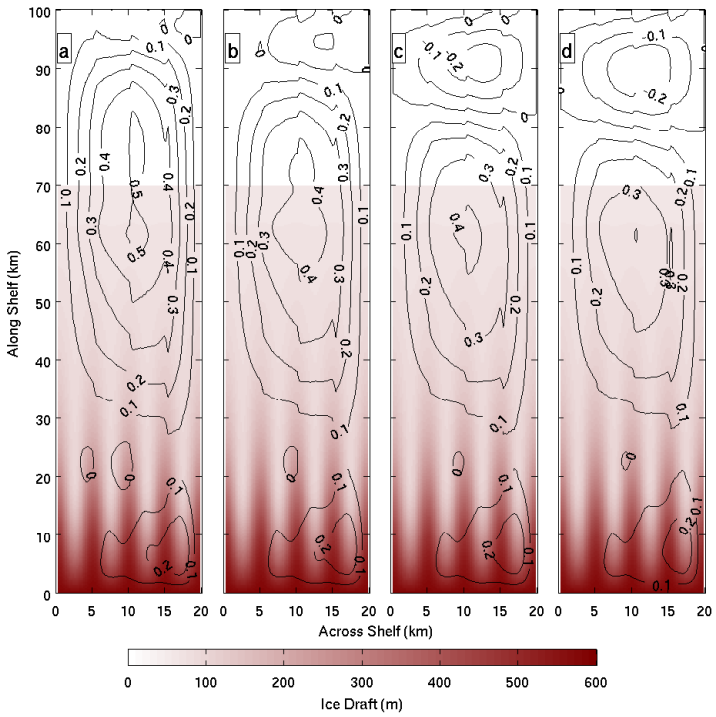

Figure 5.19: Barotropic stream function (contours) overlying ice draft (colored) for a temperature difference of a) +0.9 °C, b) +0.3 °C, c) +0 °C and d) −0.3 °C.

of melting, and hence higher fractions of meltwater in the meltwater layer resulting in a greater salinity anomaly, and vice versa for the cooling scenario. The same trend can be seen in the temperature anomalies, however the signal is aliased with the fact that as the water get warmer, the difference between initial condition and freezing temperature increases, causing the anomaly to become stronger.

5.3.3 Discussion

This study suggests that the warming of the Petermann Fjord waters seen by *Johnson et al.* (2011) is likely to have led to an increase in basal melting. It also suggests that further warming will lead to a greater increase in basal melting due to the relationship seen in Figure 5.18c). This is contrary to the findings of *Johnson et al.* (2011) who concluded that there was already more than the required heat being supplied to the ice shelf cavity for the current levels of basal melting, suggesting that an increase in

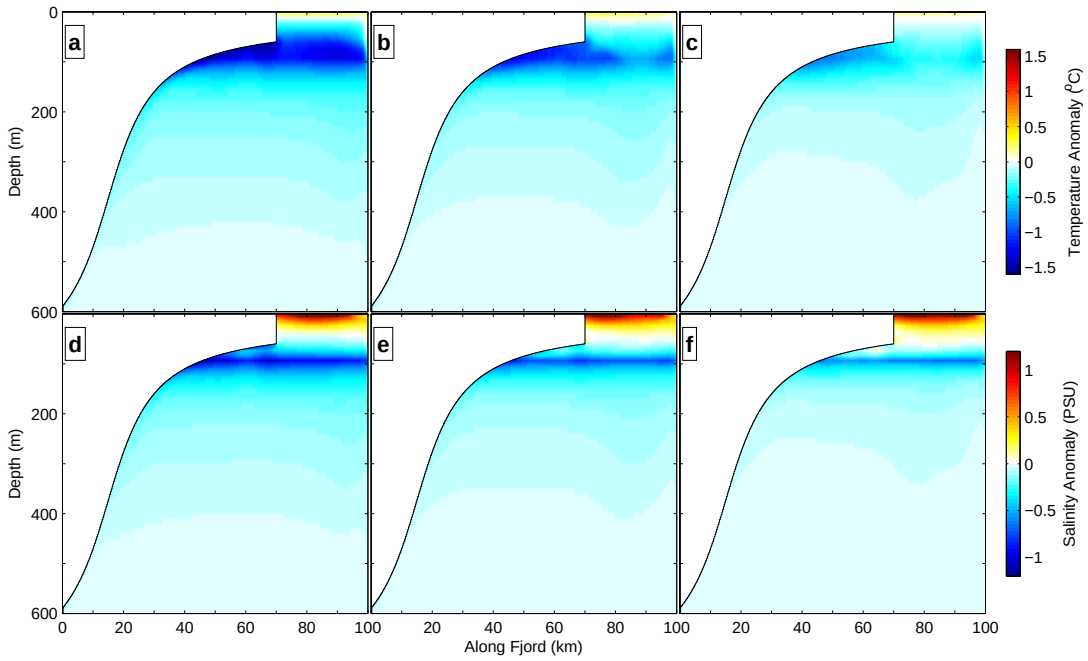

Figure 5.20: Potential temperature anomaly sections along the centre of the domain for a temperature difference of a) +0.9 °C, b) 0 °C and c) −0.9 °C and salinity anomaly sections for a temperature difference of d) +0.9 °C, e) 0 °C and f) −0.9 °C.

heat content, be it interannual variability or a continuous trend, would not increase this further. Therefore the warming effect found here must depend upon the actual ice-ocean interactions themselves rather than just the further input of heat to the cavity.

In all cases the meltwater layer detaches from the base of the ice shelf at the pycnocline depth. This constant detachment indicates that, as long as the pycnocline remains at this depth, the ice shelf would not experience an increase in melting above the pycnocline depth as the ocean warms. However greater melt rates near to the grounding line, caused by an increase in thermal forcing, signals that the ice shelf would thin closer to the grounding line.

This would lead to a decrease in stability of the ice shelf and increase the possi-

bility of large calving events, possibly even the collapse of the ice shelf. The thinning would also mean there is less contact between the ice shelf and fjord walls, leading to a potential reduction in buttressing and hence back stress on the grounded section of the glacier. In turn this could lead to an acceleration of the glacier and thinning of the grounded portion. This would be in agreement with the acceleration and ice shelf collapse seen at Jakobshavn Isbræ (*Holland et al.*, 2008a; *Weidick et al.*, 2004).

Large calving events would leave more of the fjord uncovered, allowing for the formation of more sea ice which could form an ice mélange at the terminus, increasing back stress and helping prevent calving events, however it also means that if there is not any sea-ice cover, more solar radiation could be absorbed by the fjord waters, leading to a warming of the surface layer, with the potential to increase melting underneath the thinner portions of the ice shelf and also on melting on the vertical ice front.

5.4 Impact of large calving events

5.4.1 Introduction

Recent calving events at Petermann Glacier have caused the ice front to retreat further then previously recorded (*Falkner et al.*; *Johannessen et al.*, 2011; *Münchow et al.*, 2014). Whether this is previously unrecorded natural variability or the beginning of an irreversible retreat and collapse of the ice shelf is unknown. *Nick et al.* (2012) used a numerical ice-flow model to assess the impact of such calving and found that calving led to glacier acceleration and ice shelf re-advance to its pre-calving state. However this model did not examine feedbacks of ice calving on oceanic ice-shelf melting.

One aspect that this model did not capture was melting on the vertical face of the ice shelf terminus. Melt rates on such faces can be high, especially when fed

at their base by a source buoyancy (*Xu et al.*, 2012). If Petermann Glacier were to calve far enough that the ice front were protruding beneath the pycnocline, the meltwater plume formed through basal melting could well act as such a source of buoyancy. Melt-induced undercutting on vertical ice faces has been found to have an affect on calving rates for tidewater glaciers (*O'Leary and Christoffersen*, 2013) and it is feasible that such a mechanism could occur for ice shelves.

To investigate the impact of calving events on oceanic melting (both basal and ice front) and fjord circulation, a suite of 13 calving experiments was completed. These scenarios represented a no calving case through to a total collapse case. The location of the calving events are represented by red lines in Figure 5.21. The initial conditions and restoring profiles for both salinity and potential temperature are those used for the base case in Chapter 4. The 'icefront' package (Section 3.3.3) was used in all of the scenarios within this section to calculate interactions between the ocean and vertical ice front.

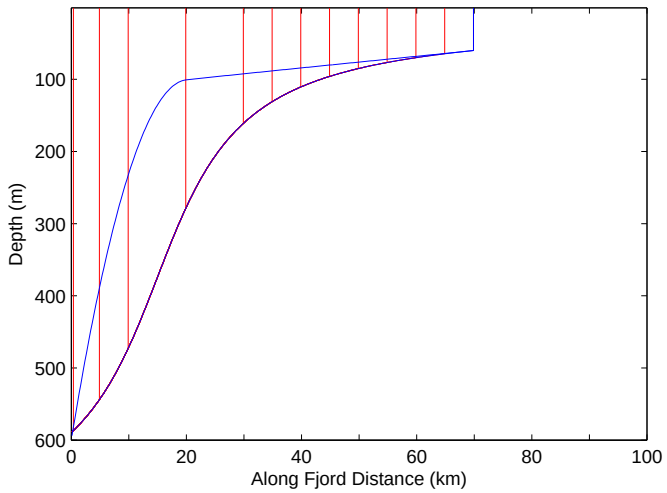

Figure 5.21: Ice draft (m) profiles for the calving scenarios. The blue profiles represent the pre calving channel crest and keel profiles. The red lines represent calving locations.

5.4.2 Results

5.4.2.1 Fjord Circulation

Figure 5.22 shows the barotropic stream functions for different calving scenarios. It can be seen that before any calving occurs (Fig. 5.22a), the circulation is the same as that described in Chapter 4. As the ice is initially calved (Fig. 5.22b), there is very little change to the circulation pattern and strength.

As further calving occurs (Fig. 5.22c), the strength of both the cyclonic and anticyclonic circulations decrease. The cyclonic circulation does not extend as far north from the grounding line, whilst the anticyclonic circulation extends further from the northern boundary. When the ice shelf has collapsed (Fig. 5.22d) the cyclonic and anticyclonic circulations disappear.

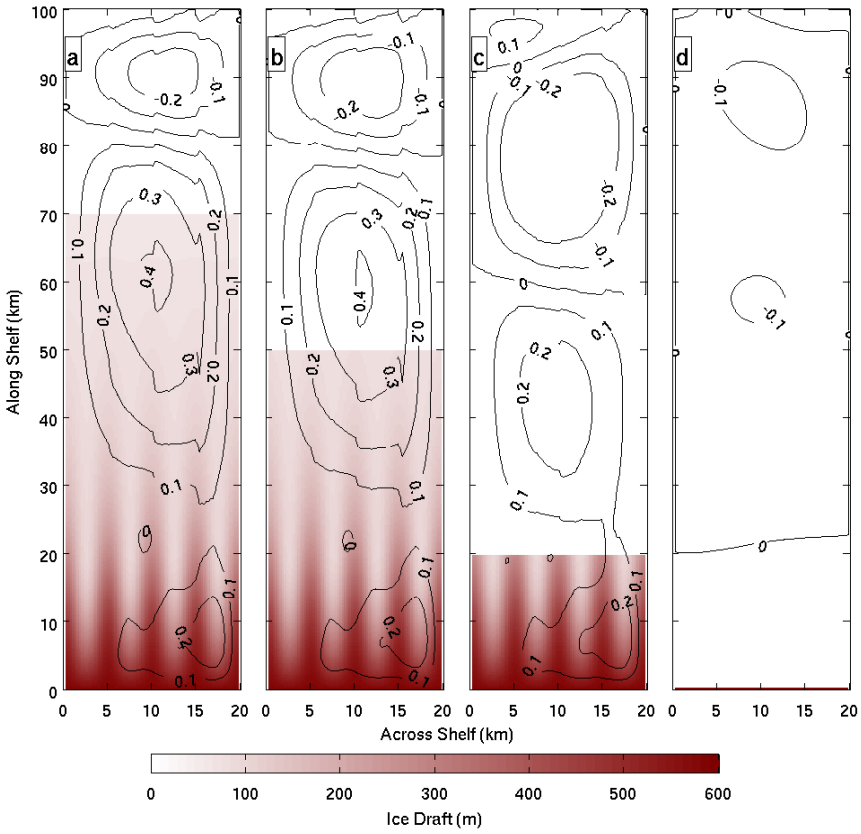

Figure 5.22: Barotropic stream function (contours) overlying ice draft (colored) for ice shelves of length a) 70 km, b) 50 km, c) 20 km and d) 0.5 km.

Figures 5.23 and 5.24 show sections of potential temperature and salinity anomalies along the centre of the domain respectively. The path of the meltwater layer can be seen as negative values in both plots, representing cooler and fresher water. In each calving event the meltwater plume detaches from the ice shelf at a depth of 100 m. As the ice shelf calves further, the size of the signal representing the meltwater layer decreases, suggesting that calving events reduce the volume of fresh meltwater. This signal is weakest for the total collapse scenario, where the melting is restricted to ice front melting only (see below), and the signal does not protrude to the same depths of the water column as it does for the other cases.

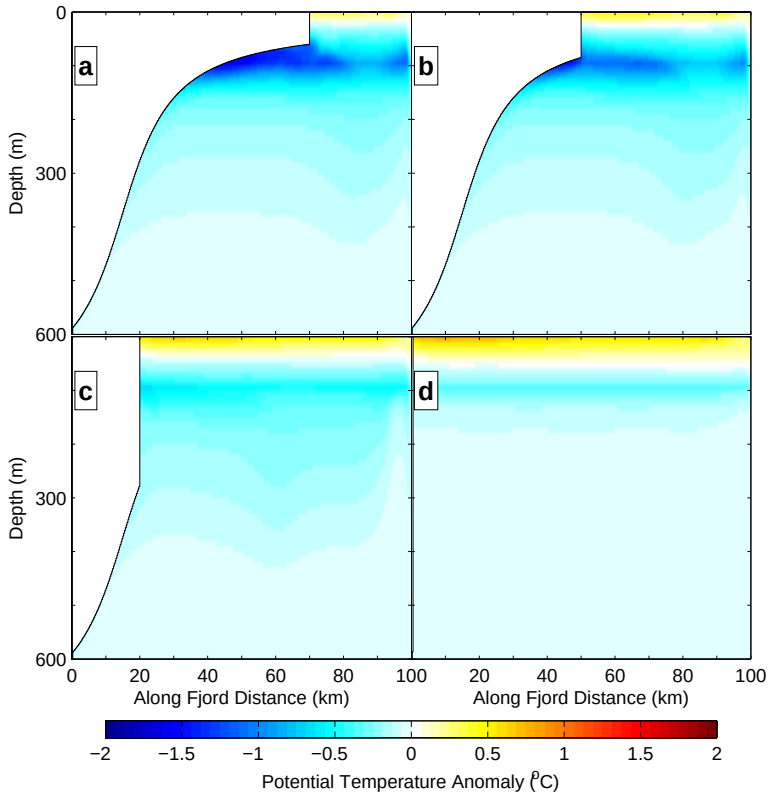

Figure 5.23: Potential temperature anomaly section along the central keel for ice shelves of length a) 70 km, b) 50 km, c) 20 km and d) 0.5 km.

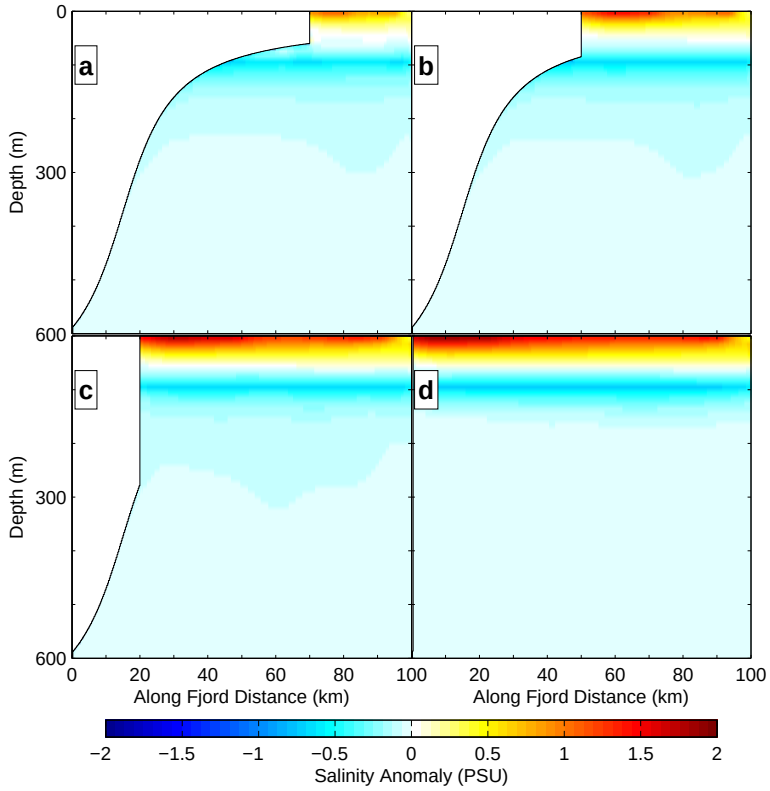

Figure 5.24: Salinity anomaly section along the central keel for ice shelves of length a) 70 km, b) 50 km, c) 20 km and d) 0.5 km.

5.4.2.2 Oceanic Melting

Oceanic melting covers both basal melting and melting on the vertical ice front. Figure 5.25 shows the basal melt rates and ocean surface flow pattern for differing calving scenarios. The pattern and magnitude of both the basal melting and ocean surface flow for the no calving case (Fig. 5.25a) is the same as that described in Chapter 4, with stronger melting on the steep initial section of the ice shelf and the sloping sides of the channels. The flow is constrained within the channels with a small level of transport between channels.

As the ice shelf is calved, the melt and flow pattern of the remaining ice shelf is similar to the corresponding area of the non-calved ice shelf. They are not affected by the removal of areas of weak or no melting near to the ice front. The areas of strong melting near to the grounding line remain consistent in all scenarios, apart

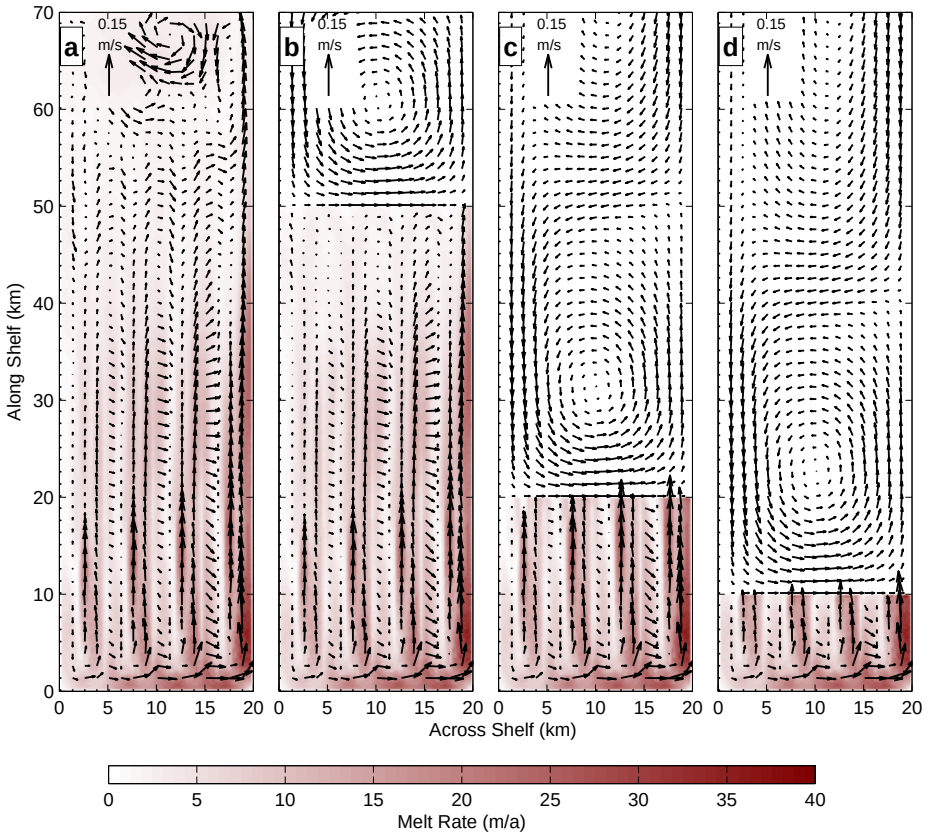

Figure 5.25: Basal melt rates (m/a) and sub-ice layer flow patterns (m/s) for ice shelves of length a) 70 km, b) 50 km, c) 20 km and d) 10 km.

from the full collapse case, when that area has been calved.

As the ice shelf calves, the draft of the ice front increases, meaning that it protrudes further into the warmer subsurface waters. Figures 5.26 and 5.27 show the mean melt rates, calculated using the 'icefront' package, for the ice front during different calving scenarios, (note the change in colour scale between the two figures). Before calving, the mean ice front melt rate is relatively low and remains so for the initial calving events (Fig. 5.26).

As further calving occurs (Fig. 5.27) the levels of ice front melting increase rapidly to a maximum for the ice shelf collapse scenario. The melt rates are slightly larger on the eastern edge of the ice front, corresponding with the location of the meltwater layer exit from the cavity. This is not seen in the full collapse scenario as

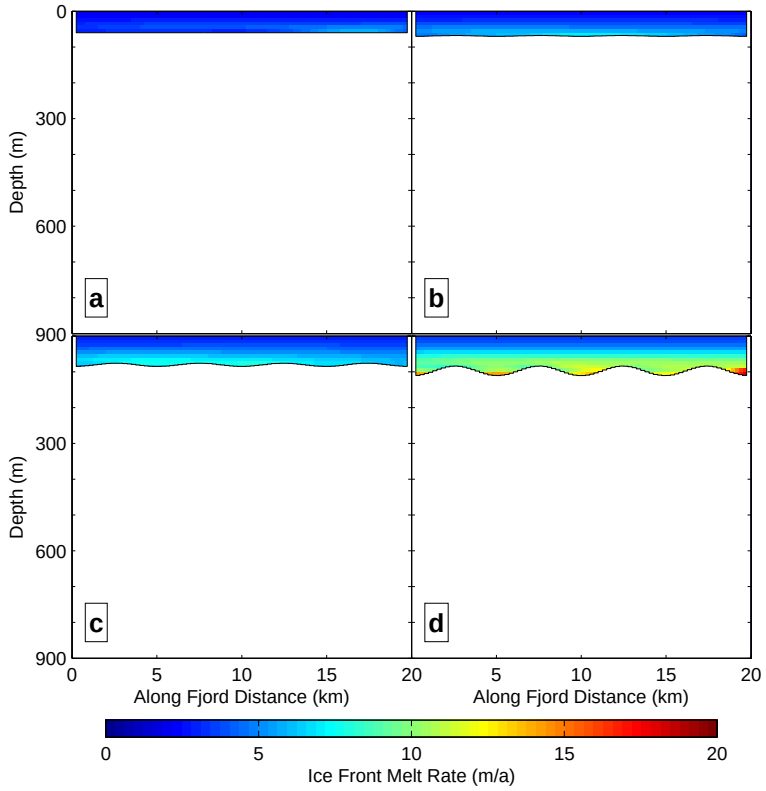

Figure 5.26: Ice front melt rates (m/a) for ice shelves of length a) 70 km, b) 60 km, c) 50 km and d) 40 km. Melt rates are plotted looking out of the fjord.

the meltwater layer does not form beneath the ice shelf. It should be noted, however, that the model cannot resolve the vertical velocity, due to the horizontal resolution being 250 m, with the modelled vertical velocity likely to be an underestimate. The vertical flow is expected to be finer, therefore melting rates and patterns on the vertical ice front need to be taken with a degree of caution.

The relationship between ice shelf length and mean basal melt rate is shown in Figure 5.28a. The mean basal melt rate for the entire ice shelf (blue) increases as calving occurs, to a maximum when the ice shelf is only 5 km long. After this point the mean basal melt rate decreases rapidly as the area of strong melting is removed. This increase is due to the removal of the weakly melting areas near to the ice front which were reducing the mean melt rate. This can be seen by looking at the mean basal melt rate of the first 20 km of the ice shelf (red). This remains relatively

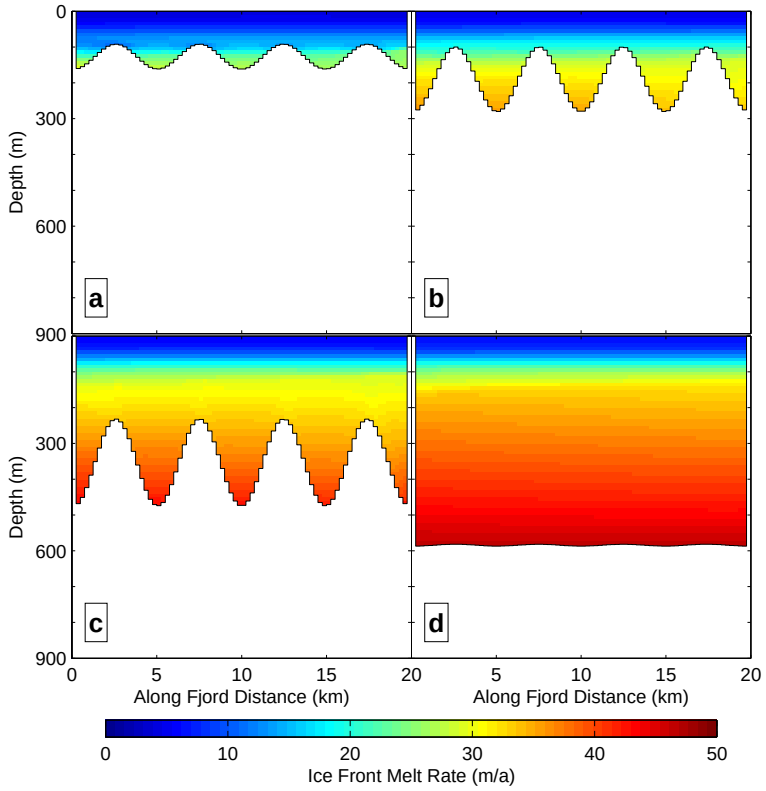

Figure 5.27: Ice front melt rates (m/a) for ice shelves of length a) 30 km, b) 20 km, c) 10 km and d) 0.5 km. Melt rates are plotted looking out of the fjord.

constant across calving scenarios, confirming it is the removal of the weakly melted areas that is causing the increase in mean basal melt rate.

There is a non-linear relationship between mean ice front melt rate and ice shelf length (fig. 5.28b) with the initial calving events having little effect on the mean ice front melt rate. After approximately 35 km of calving, the mean ice front melt rate increases much more rapidly. The relationship between ice shelf length and the total volume of ice melted through both basal and ice front melting (fig. 5.28c), shows that although both of the mean melt rates are increasing as the ice shelf calves, the total volume of ice melted is monotonically reducing, implying that the increase in melt rates does not compensate for the reduction in ice area.

One consequence of the increase in ice front melting is melt induced undercutting of the ice shelf at the ice front; melting removes more ice from the bottom of the ice

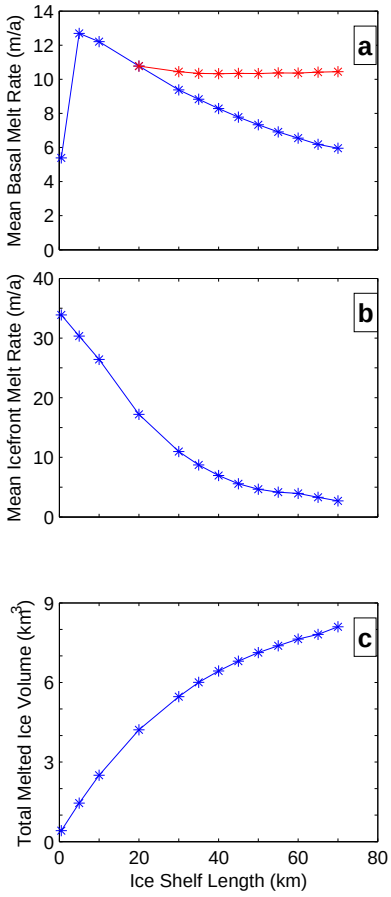

Figure 5.28: Relationship between length of ice shelf and a) basal melting for the whole ice shelf (blue) and first 20 km of the ice shelf (red), b) ice front melt rate and c) the total volume of ice melted per annum through both basal and ice front melting.

front than from the top. Figure 5.29 shows the inferred profile at the centre of the ice front for each calving scenario after one year of ice front melting. There is little undercutting until the calving events increase the draft of the ice shelf to greater than 100m. After this point the levels of undercutting increase until it reaches a maximum of approximately 47 m/y for the total collapse case. Again, these results must be taken with a degree of caution due to the inability to resolve the vertical flow by the ice front, however it is expected that melting on the ice front would be depth dependent, as observed in the model.

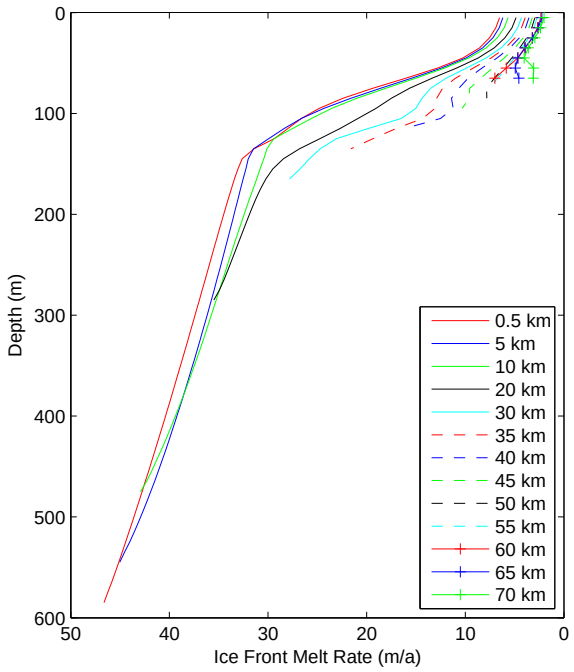

Figure 5.29: Profile of ice front melting, showing inferred melt-induced undercutting, taken at centre of middle keel.

5.4.3 Discussion

As the glacier calves, the draft at the ice front increases, meaning the ice face protrudes deeper into the water column. Therefore a greater proportion of the ice front is in contact with the warm modified Atlantic Water, leading to an increase in ice front melting. The rate at which melting at the ice front increases, is due to the rate at which the ice front deepens, which is controlled by the geometry of the ice shelf.

As the ice is relatively flat near the un-calved ice front of the glacier, and above the pycnocline, the draft at the ice front increases by only a small amount as calving events occur and doesn't penetrate the pycnocline into the warmer Atlantic waters below, causing only a relatively small increase in mean ice front melting as seen in Figure 5.28b. Further calving events move the ice front into the portion of the glacier where the draft increases rapidly, so the ice front draft also increases rapidly as calving events occur. This increase in draft means that the ice front comes into

contact with the warmer sub-surface waters, resulting in a rapid increase in mean melt rate. This implies that it is the area of the ice front in contact with the warmer sub-surface waters that controls the mean ice front melt rate.

As the calving events occur, basal melt rates and sub-ice layer flow patterns near the grounding line remain relatively constant, unaffected by events downstream of their location, with the mean melt rate of the first 20km consistent across all runs with an ice shelf longer than 20 km. At the same time the mean melt rate for the ice shelf is increasing as it calves. This is due to the calving events removing areas of low melt, with areas of higher melt remaining.

The factors affecting the mass balance of the post-calving ice shelf remain the same as those for the full ice shelf and are discussed in Section 1.2.2. The assumption that the surface ablation rate (per unit area) remains constance implies a small decrease in total surface ablation. Figure 5.28c shows that as calving events occur, the total volume, and hence mass, of ice lost to oceanic melting decreases. Under the assumption that the flux of ice across the grounding line remains constant, these factors indicate an increase in mass balance. An understanding of calving mechanisms is therefore needed to calculate whether calving rates will increase sufficiently to counteract this mass increase, or whether the ice shelf will re-advance.

O'Leary and Christoffersen (2013) found that undercutting of tidewater glaciers, due to melting at the ice front, leads to increased calving rates. Although this modelling study focused on tidewater glaciers, it is possible that a similar feedback mechanism could occur for ice shelves. Undercutting thins the ice at the terminus, resulting in a bending at the end of the ice shelf and an increase in surface stress. This increase leads to an increased likelihood of fracture and hence calving.

If we take a conservative estimate of the ice flow remaining constant at 1 km/a, despite the decrease in buttressing due to ice calving, along with a liberal estimate for undercutting of 50 m/a, then, for the ice front position to remain stable, the melt

induced undercutting would need to cause calving up to 20 times it's own magnitude upstream of the ice front to be solely responsible for ice-front retreat. This estimate is much greater than any estimate modelled by *O'Leary and Christoffersen* (2013), although the use of their estimates is subject to the caveats above.

Nick et al. (2012) used an ice-flow model to study the response of Petermann Glacier to large calving events. The modelled terminus velocity following the 2010 calving event agreed with observed data in showing only a minor speed-up when compared to pre-calving velocities. This insensitivity was attributed to the low along-flow resistive forces for the terminus region of the ice shelf due to it's limited attachment to the fjord walls and it's geometry being thin and wide. The model found that the glacier re-advanced to its pre-calving extent, with the advance speed being comparable to the glacier flow speed, indicating a suppression of calving during the re-advance.

A second calving event, reducing the ice shelf length by a further 20 km, caused an increase in both glacier velocity and flux across the grounding line. This increase in flow was attributed to the greater reduction in buttressing caused by the area of ice shelf removed being thicker than during the first calving event, and the lateral drag coefficient being larger. The increased influx was found to diminish as the ice shelf re-advanced and buttressing increased. Similarly to the first calving event, the ice shelf in this scenario re-advanced to the initial ice shelf length. In both cases no grounding line retreat occurred, leading the authors to surmise that calving events of this size are not sufficient to destabilise Petermann Glacier.

Although *Nick et al.* (2012) did not include ice front or basal melting in their flow model, their results indicate that the increased ice flux would outweigh any undercut-induced calving by the mechanism of *O'Leary and Christoffersen* (2013). The high levels of ice front melting seen in the above scenarios would decrease as the ice shelf advanced, leading to a further decrease in undercutting and hence calving.

5.5 Summary

The simulations within this chapter show that Petermann Glacier is susceptible to potential changes in conditions within Petermann Fjord.

The impact of changing the depth of the stratified layer, be it permanent or seasonal, is to change the depth at which the meltwater layer detaches from the ice shelf base. This, in turn, alters the area of the ice shelf in contact with this layer. As, to a good approximation, basal melting is reliant on the friction velocity between this meltwater layer and the ice base, if it were to detach at a greater depth, basal melting would occur over a smaller area of the ice shelf, hence reducing the mean melt rate and vice versa.

Model results suggest that should the warming of subsurface waters within the fjord, as seen by *Johnson et al.* (2011), to continue, the basal melt rates would increase. Significantly, melt rates near to the grounding line would increase, leading to a thinning of the ice shelf in this area. This could lead to am increase in ice shelf instability and increase the possibility of large calving events and even ice shelf collapse, in agreement with that seen at Jakobshavn Isbræ (*Holland et al.*, 2008a; *Weidick et al.*, 2004).

If the ice shelf were to retreat without a warming ocean signal, the model predicts that the increase in undercutting at the ice front, due to it penetrating further into the subsurface water, would not be sufficient to prevent the ice shelf from re-advancing to its previous position. The impact of calving with warming subsurface waters was not investigated, but it is possible that the increase in both undercutting induced calving and increased ocean melting would be sufficient to balance or even surpass the flux of ice across the grounding line.

Chapter 6

Ice-Ocean Interactions Beneath Petermann Glacier (real-world domain)

There are currently no realistic modelling estimates for basal melt rate or ocean circulation beneath Petermann Glacier's ice shelf. Current melt rate estimates have been calculated from satellite data (*Rignot and Steffen*, 2008) whilst knowledge of the circulation within the fjord has been inferred from hydrographic surveys in the fjord mouth and adjoining Hall Basin (*Johnson et al.*, 2011).

In this chapter the circulation beneath a realistic Petermann Glacier ice shelf geometry is modelled. The real bathymetry beneath the ice is unknown, so an investigation is undertaken into the impact of the different fjord bathymetries, introduced in Chapter 2, on both basal melt rates and fjord circulation. The impact of the two recent calving events is also investigated.

6.1 Model Specifics

To investigate the circulation beneath Petermann Glacier, the realistic ice topography is used with each of the three possible bathymetries created in Chapter 2. Calving events are implemented by removing ice from the ice front of the ice shelf, as in Section 5.4. Melting on the vertical ice front, introduced in section 3.3.3, is included within the model. A Cartesian grid with a resolution of 250 m in the horizontal and 10 m in the vertical is used, and partial cells with a minimum height of 0.5 m are used, as in Chapter 4. Note that the 250 m horizontal resolution means that the vertical flow at the ice front cannot be resolved properly.

As the mouth of Petermann Fjord is connected to Hall Basin in Nares Strait, open boundary conditions (Section 3.3.4) are used on all ocean boundaries. The salinity and potential temperature profiles used for initial conditions and at the boundaries, are either the same as those used in Chapter 4 or take the form of an unstratified water column with potential temperature and salinity homogenous at the deep water properties. The model was spun up with a 6-second time step until steady after one year. All results are shown as monthly averages from the last month of the model run.

To allow comparison with the idealised domain, we refer to the southern boundary as the boundary to which the grounding line is adjacent, the northern boundary as the fully open ocean boundary, and the eastern and western boundaries as the right and left hand side boundaries respectively when looking downstream of the grounding line. Note however that the domain has been very slightly rotated so that the model grid is more aligned with the orientation of the fjord. This means that the directions described above are not the true directions of these boundaries.

6.2 Bathymetry

6.2.1 Introduction

Due to the remote location of Petermann Fjord and the inherent difficulties in observing the cavity beneath an ice shelf, the majority of the fjord bathymetry is unknown. As discussed in Chapter 2, only the bathymetry of Hall Basin, the fjord mouth and the grounding line depths are known. These data reveal the presence of a sill at the fjord mouth, with a deep basin inshore of the sill. On the south-western side of the fjord, inshore of the sill is a shallower shelf.

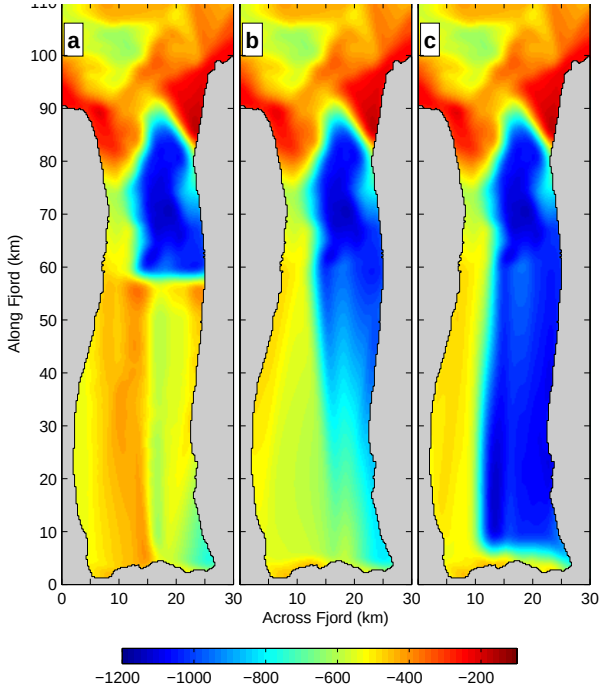

Figure 6.1: Realistic bathymetry scenarios with a) small basin, b) linear shallowing and c) large basin.

It is unknown how far inshore the deep basin or shallow shelf protrudes. Here we investigate three different possible bathymetries for Petermann Fjord, a deep basin protruding approximately 10km underneath the ice shelf, a linearly sloping sea bed from the ice front to the grounding line and a deep basin protruding to within a couple of kilometers of the grounding line (Fig. 6.1). In all cases the same realistic

ice-shelf topography was used (Fig. 6.2).

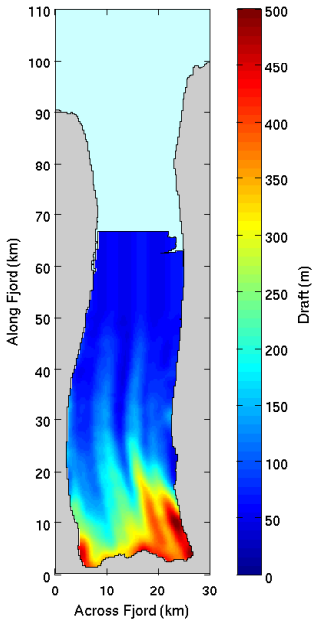

Figure 6.2: Ice shelf topography for the realistic Petermann Glacier domain.

6.2.2 Effect of Bathymetry

The melt rate and sub-ice layer velocities (velocities from the 10 m of the ocean column immediately beneath the ice) for the three different bathymetries are shown in Figure 6.3. It can be seen that the patterns in both melt rate and flow pattern are similar across all three scenarios, with the area-mean basal melt rates for the three scenarios being 5.71 m/a for the linearly sloping bathymetry, 5.46 m/a for the small basin and 5.78 m/a for the large basin bathymetry.

The barotropic stream functions for the three bathymetries are shown in Figure 6.4. It can be seen that in all three cases there is a cyclonic circulation within the fjord bringing warmer modified Atlantic Water into the cavity along the western boundary, with a return flow out of the fjord along the eastern boundary. The strength of these circulations is consistent across all three bathymetries, however the extent to which the circulation extends beneath the ice shelf varies. The circulation

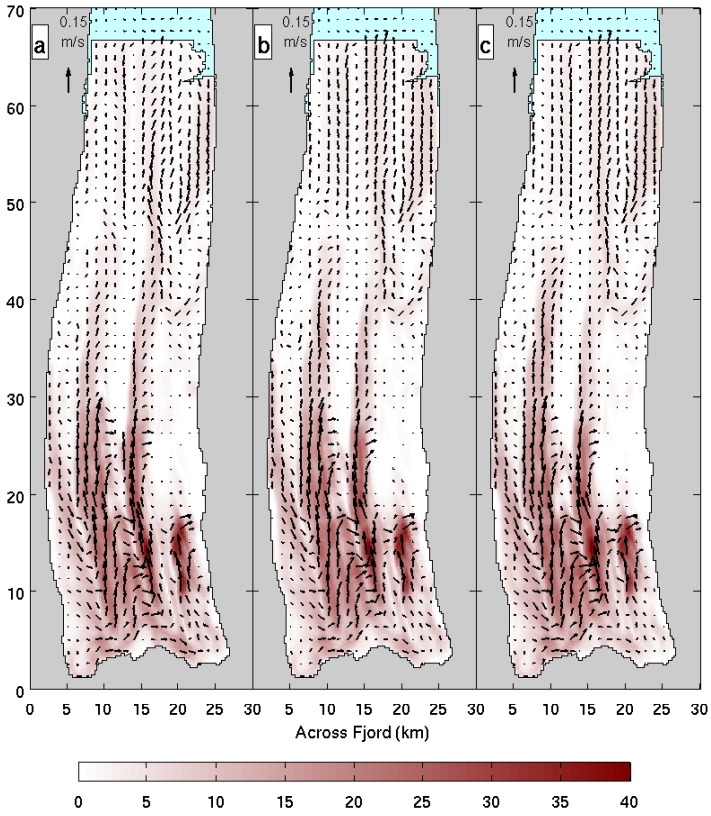

Figure 6.3: Melt rates (m/a) and sub-ice layer velocities (m/s) for the a) small-basin, b) linear-sloping and c) large-basin bathymetries.

extends furthest for the large basin case, and extends the least under the ice shelf for the small basin case, suggesting a bathymetric control on the circulation, with the shallowing of the sea bed preventing the deeper water from penetrating further into the cavity. In all three cases there is an anticyclonic circulation of similar strength and location in the open ocean section.

6.2.3 Discussion

Comparison of the three investigated bathymetries shows consistent basal melting, yet varying cavity circulation. This suggests that there is sufficient heat entering the cavity, irrespective of the chosen bathymetry. For this reason the linearly sloping bathymetry will be used for the remainder of this chapter. This bathymetry was

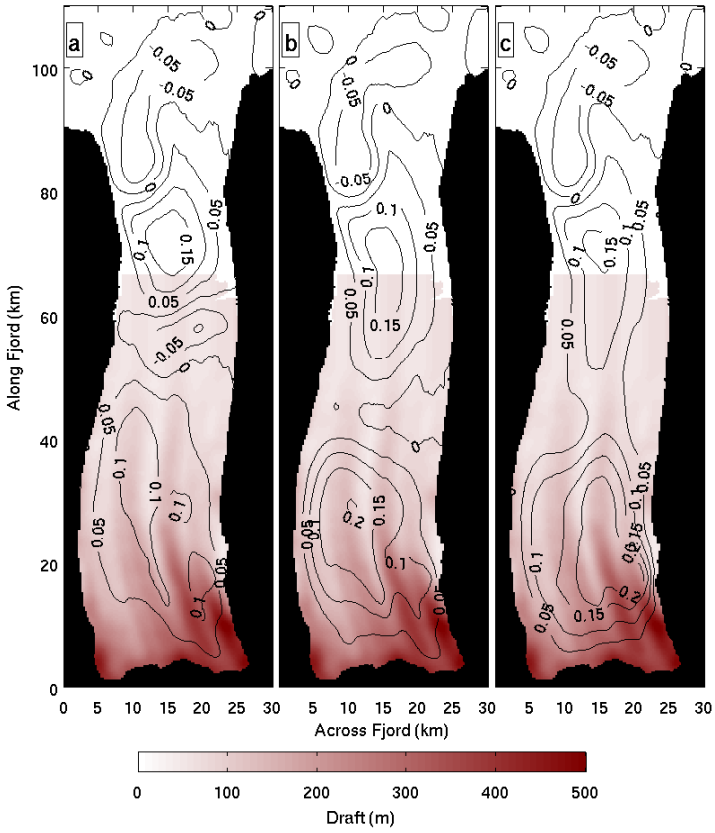

Figure 6.4: Barotropic stream function (contours) overlying ice draft (colored) for the a) small-basin, b) linear-sloping and c) large-basin bathymetries.

chosen simply because we do not know what happens between the open fjord section and the grounding line.

It is worth noting, however, that the three bathymetries chosen are only a small subset of the total possible bathymetries that could lie underneath Petermann Glacier. Neither of the bathymetries are particularly geophysically plausible, as mentioned in Chapter 2. They were chosen as, due to the inherent difficulties within collecting data from within ice shelf cavities, the features underneath the ice shelf are unknown, however further smoothing over this section may have allowed for the removal of some of the unlikely straight line features present.

It is also possible that there are unknown features which could have a large impact on both circulation and melt rates. For example there is a large seabed ridge beneath

Pine Island Glacier (*Jenkins et al.*, 2010a) and *De Rydt et al.* (2014) found that such ridges can restrict the flow of warm deep water into the cavity near the grounding line, reducing the level of basal melting and hence the resulting overturning circulation.

6.3 Comparison of real world model with idealised model and real world observations

The results from this model simulation are now compared to both the four-channel idealised model from Chapter 4, and also the current knowledge of Petermann Glacier Ice Shelf and the oceanography of Petermann Fjord. The four-channel idealised case is used because there are four pronounced channels beneath Petermann Glacier's real ice shelf (*Rignot and Steffen*, 2008).

6.3.1 Realistic vs. Idealised Models

6.3.1.1 Basal Melting

The basal melt rates and sub-ice layer velocities for the realistic and four-channel idealised domains are shown in Figure 6.5. The mean melt rates for the two domains are similar, (realistic = 5.71 m/a, idealised = 5.95 m/a), however direct comparison of these numbers alone is not sufficient as the topography of both the ice shelves and their channels differ; a comparison of melt patterns and ocean flow is also required.

As discussed in Chapter 4, under the idealised ice shelf, melt rates are highest in areas of strong sub-ice layer velocities. This is on the right hand slope of channels, and in the centre of the channels near the grounding line where the ice-base gradient is steeper. The flow beneath the ice shelf is constrained by the channels with a degree of slip-over between the channels. Figure 6.5b shows that the flow beneath the realistic ice shelf is also constrained within the channels, again with a degree of

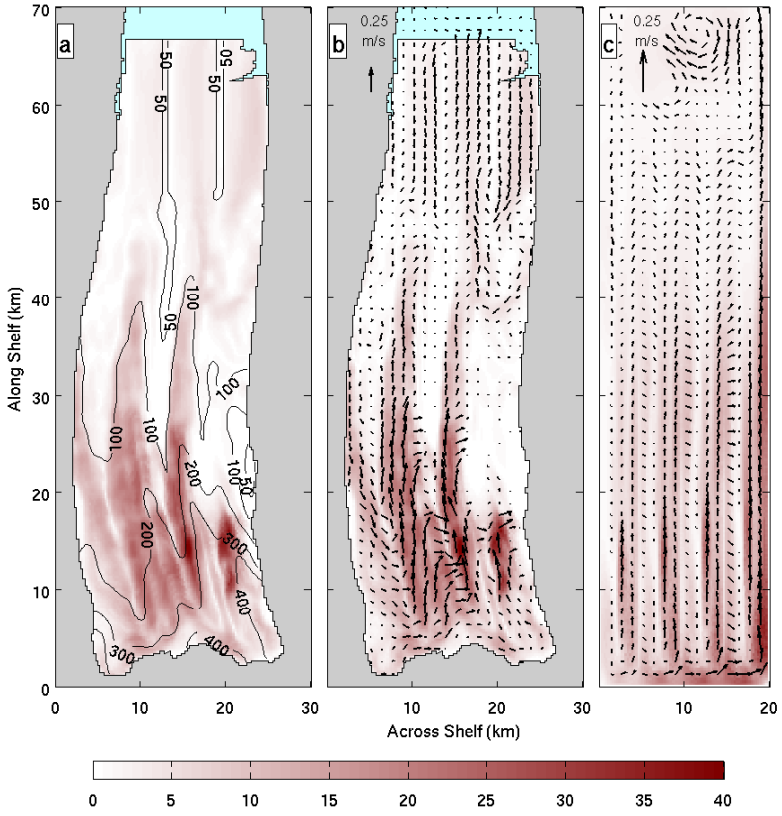

Figure 6.5: a) Melt rates (m/a) overlain by contours of ice draft, melt rates (m/a) and sub-ice layer velocities (m/s) for the b) realistic and c) idealised domains.

slip-over between the channels.

The highest melt rates are within the channels, again beneath the strongest flow rate. The weaker melt rates are between these channels, where the velocity of the sub ice layer is low, and near the ice front where the ice is shallower than the pycnocline. The meltwater layer detaches from the ice base at the pycnocline depth, flowing away from the ice shelf. The meltwater layer is replaced by the penetrating surface stratified layer which flows under the ice shelf near the fjord walls and exits the cavity in the middle of the ice shelf. This cooler, fresher surface stratified layer protects the ice shelf from the meltwater layer, preventing higher melt rates. There is a higher degree of inflow of surface stratified layer under the realistic ice shelf than under the idealised ice shelf.

One disparity between the two models is the eastern boundary current, and associated basal melting, seen in the idealised case, and the idealised model of *Gladish et al.* (2012), not forming underneath the ice shelf in the realistic model. This is most likely caused by detachment of the meltwater layer at the pycnocline approximately 20 km north of the grounding line. This is most likely caused by a discrepancy in the model draft at this location which can be seen as a shallow area in Figure 6.5a).

6.3.1.2 Oceanography

Figure 6.6 shows the barotropic stream functions for the realistic and idealised cases. In both cases there is a geostrophic circulation bringing warm modified Atlantic Water into the ice shelf cavity along the western boundary of the domain, whilst a return flow transports water out of the cavity along the eastern boundary.

A similar pattern of anticyclonic circulations underneath the ice shelf can be seen in both cases, with the circulation weaker underneath the realistic ice shelf. Despite the circulation being weaker, the mean melt rates are similar, suggesting that ocean heat flux into the cavity is not the limiting factor in determining the melt rate.

This reduction in circulation strength is likely caused by the reduction in volume of meltwater between the two simulations (both mean melt rate and size of ice shelf is smaller for the realistic ice shelf). There is also a weak cyclonic circulation present in the open ocean section of the real world domain, similar to that seen in the idealised domain, and is constrained to the central section of the domain, likely caused by the fjord walls extending approximately 20 km further from the grounding line than the ice shelf. The velocities on the open boundaries show a weak flow into the domain from the west and a weak flow out of the domain in the east.

The warm Atlantic Water brought into the cavity melts the ice base, freshening and cooling the water at the ice-ocean interface, creating a plume which rises against the ice shelf base. An inspection of the anomalies between final and initial conditions

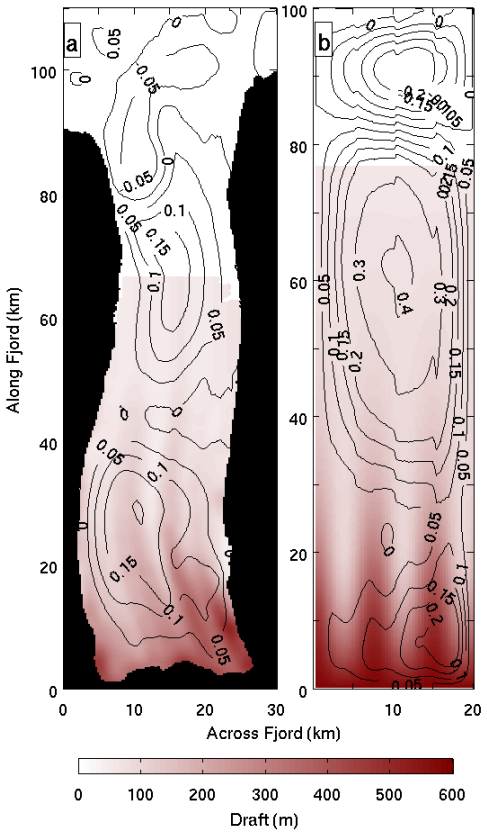

Figure 6.6: Barotropic stream function (contours) overlying ice draft (colored) for the a) realistic and b)idealised domains.

of both potential temperature and salinity along the centre of the domain for the idealised and realistic domains (Fig. 6.7) reveals a similar overturning circulation caused by the rising meltwater layer in both cases.

In both of the simulations, the meltwater layer can be seen as a cooler, fresher anomaly (darker blue in both anomalies) detaching from the ice base at the pycnocline depth of 100 m, and flowing towards the northern boundary. The potential temperature anomalies show that the meltwater layer is thicker and cooler underneath the idealised ice shelf, whilst the salinity anomalies indicate that the meltwater layer is also fresher underneath the idealised ice shelf. This is caused by the larger volume of cooler, fresh meltwater mixing with the water at the interface. The larger volume of fresh meltwater leads, in turn, to a larger buoyancy, causing faster melt-

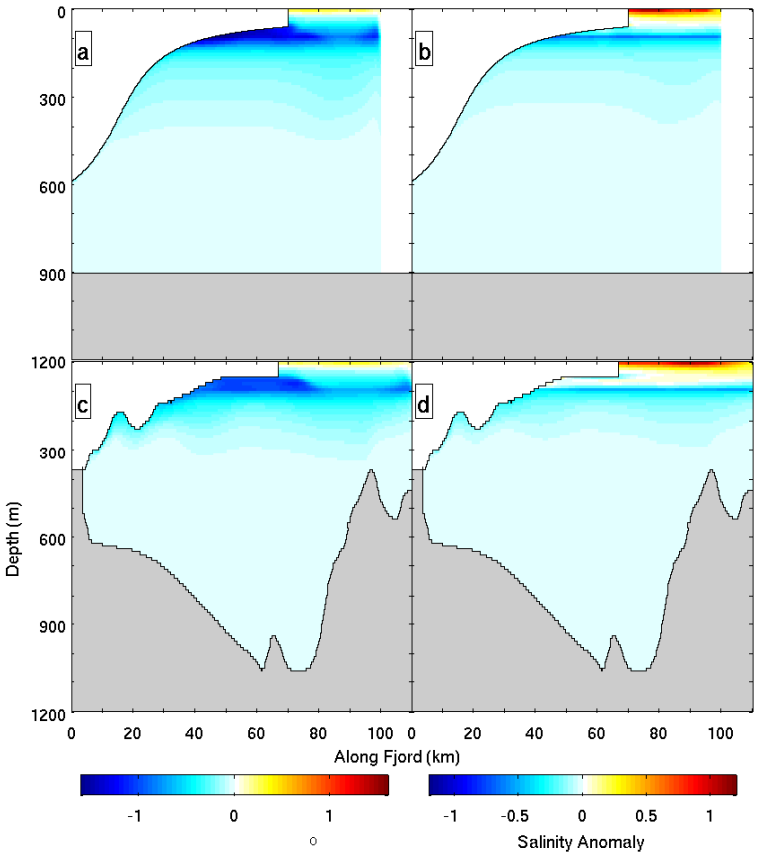

Figure 6.7: Anomaly profiles along the centre of the domain for a) potential temperature and b) salinity in the idealised domain, and c) potential temperature and d) salinity in the realistic domain.

water layer velocities (Fig. 6.5) and a faster barotropic circulation in the idealised domain (Fig. 6.6).

6.3.2 Realistic Model vs. Observations

6.3.2.1 Oceanography

Due to the difficulties of obtaining oceanographic measurements from beneath an ice shelf, we are reliant on the hydrographic survey reported by *Johnson et al.* (2011)

and the through-ice-shelf profile of *Rignot and Steffen* (2008) for a comparison of the fjord circulation. The across-fjord geostrophic velocity profile obtained near the ice front in 2009 shows a flow out of the fjord near the surface on the north-eastern side of the fjord, and a surface flow into the fjord on the south-western side. At depth there is a slow flow into the fjord (Fig. 6.8a).

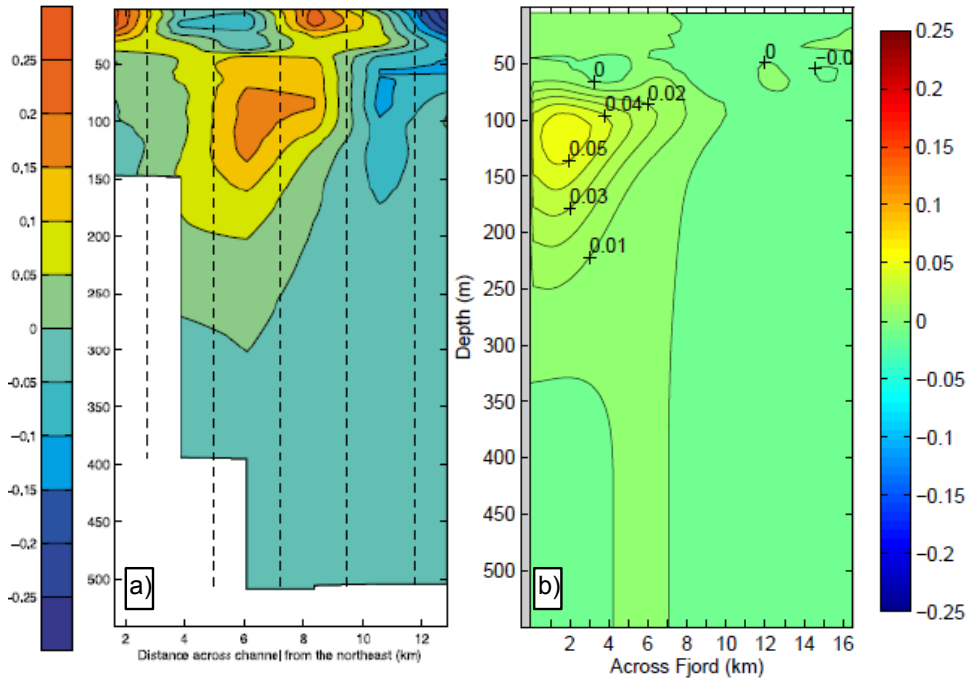

Figure 6.8: a) Across fjord geostrophic velocity profile (m/s) taken near the ice front, (Source: *Johnson et al.* (2011)). b) Across fjord modelled velocity profile (m/s) taken one kilometer after the ice front. Both profiles look into the fjord and a positive velocity denotes a flow out of the fjord. The eastern wall of the fjord is on the left of the profile and the western fjord wall on the right.

Figure 6.8b) show an across-fjord model velocity profile taken near the model ice front. Although it shares some common features with the observations of *Johnson et al.* (2011), it is strikingly different. There is a flow out of the domain on the eastern side of the domain focused at the pycnocline depth, whilst there is a very weak flow into the fjord on the western side of the domain. The magnitude of these

flows is, however, approximately five times smaller than those observed by *Johnson et al.* (2011), and there is far less structure in the model profile than seen in the observed profile.

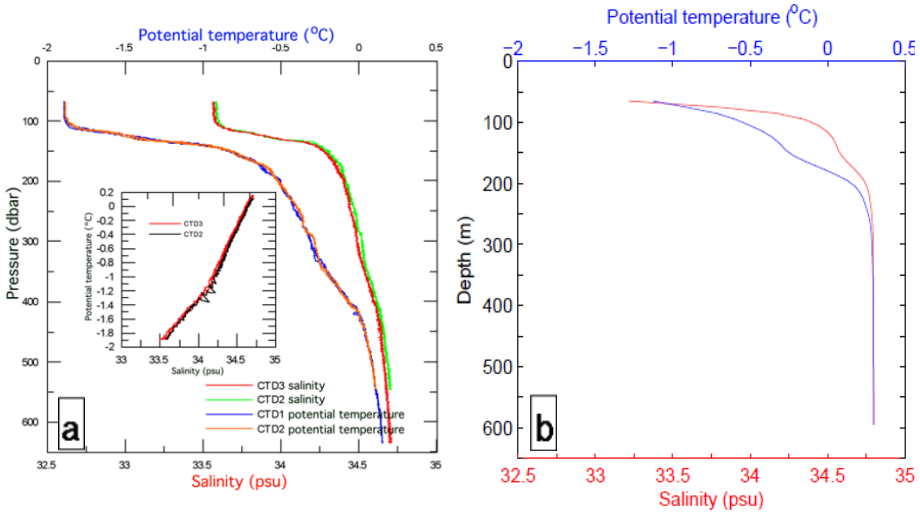

Figure 6.9: a) Beneath ice shelf potential temperature and salinity profiles collected by *Rignot and Steffen* (2008). b) Beneath ice shelf potential temperature and salinity profiles from the realistic model, taken at the approximate location of the *Rignot and Steffen* (2008) drill site.

Sub-ice shelf potential temperature and salinity profiles from the realistic model are plotted against depth to assess whether the water column features observed by *Rignot and Steffen* (2008) are present (Fig. 6.9). The mixed layer present in the *Rignot and Steffen* (2008) profiles are not present in the realistic model. The top of the water column in the model is slightly warmer and fresher than that observed by *Rignot and Steffen* (2008).

These differences all indicate that the main driver behind the differences between the observed and modelled circulations is an absence of sufficient mixing within the model. The choice of constant viscosity parameters rather than the implementation of a mixing closure scheme, such as the Pacanowski/Philander scheme (PP) has prevented mixing from occurring within the ocean. This would explain the lack of structure within the circulation profile, and also the lack of boundary layer in

the through ice profile. Had there been sufficient boundary layer mixing occurring underneath the ice shelf then it is likely that the boundary layer observed by *Rignot and Steffen* (2008) would be present in the model profile.

The choice of ocean boundary conditions may also be a cause of the significant differences. In Kennedy Channel there is a northward flow along it's Greenland boundary which enters Petermann Fjord on the western boundary with a velocity of approximately 0.2 m/s (seen in Fig. 6.8). Conservation of mass dictates that this needs to be counterbalanced by a transport out of the domain which is comparable if not larger due the flux of water into the fjord from ice shelf melting.

This flow into the domain is not included within the model, and therefore the potential for a lot more structure to the circulation is lost. At the same time the heat transport into the domain is also vastly reduced (approximately an order of 5) which, along with the lack of mixing across boundary layers, means that there is less heat reaching the base of the ice shelf within the model than the observations would indicate. The chosen boundary profiles for salinity and potential temperature are also highly idealised, a more realistic profile would allow for further structure to be introduced to the model ocean.

External drivers such as winds and tides, which are not included within the model, may also play an important role in both the structure of the ocean circulation and the resultant heat transfer into the cavity. The inclusion of tides may also result in near-inertial motions through interactions with the sill. These motions would provide further structure to the cavity, which along with enhanced mixing, may have resulted in a more realistic ocean circulation.

6.3.2.2 Basal Melting

There are some striking similarities and discrepancies between the modelled melt rates (Fig. 6.10a) and those calculated by *Rignot and Steffen* (2008) (Fig. 6.10b).

Both show pronounced areas of melting within the channel features and close to the grounding line, with the channelised melting extending to a similar distance downstream of the grounding line in both cases. There is a consistent pattern of decrease in melt rate as the ice shelf thins towards the ice front.

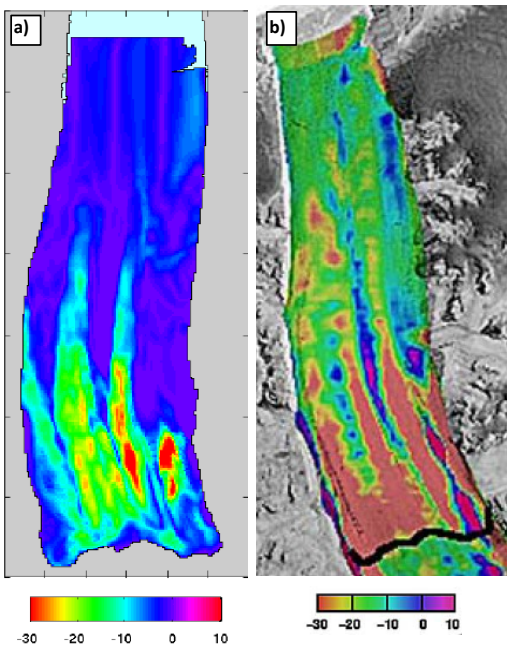

Figure 6.10: a) Modelled melt rates for the realistic Petermann domain with linear sloping bathymetry. b) Petermann Glacier steady state basal melt rates (m/y) calculated from divergence of ice flux. The black line represents the grounding line (Source: *Rignot and Steffen* (2008)).

The modelled melt rates near the grounding line are, however, approximately half of those calculated by *Rignot and Steffen* (2008) and the modelled melt rates near to the ice front are nearly an order of magnitude smaller than *Rignot and Steffen* (2008). In the model, the high melt rates do not extend far downstream on the eastern boundary due to the detachment of the boundary current as previously discussed. *Rignot and Steffen* (2008) have significant melt rates extending further downstream in this location.

Rignot and Steffen (2008) calculations resulted in areas of basal freezing beneath

Petermann Glacier which are not present in the model domain. Given the ample supply of heat into the fjord for the levels of melt rate reported by *Rignot and Steffen* (2008) as observed by *Johnson et al.* (2011), it is unlikely that these areas of freezing are realistic.

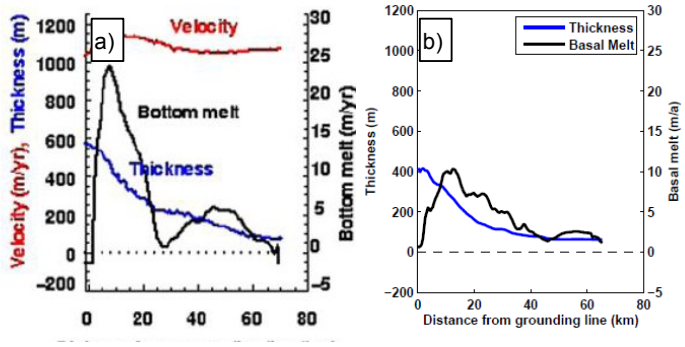

Figure 6.11: a) Petermann Glacier observed along shelf area averaged basal melt rate, and ice shelf thickness (Source: *Rignot and Steffen* (2008)). b) Petermann Glacier modelled along shelf area averaged basal melt rate and ice thickness.

The across-shelf averaged melt rates show this difference in melt rates. *Rignot and Steffen* (2008) found the melt rates to increase to approximately 25 m/a, 10 km downstream of the grounding line, whilst the model has a maximum mean melt rate of 10 m/a at the same location (Fig. 6.11). The secondary increase in mean melt rate, peaking at 45 km downstream from the grounding line reported by *Rignot and Steffen* (2008) was not found in the model, however the area of low melting between the primary and secondary increases is due to the unlikely areas of freezing seen upstream of this location in the *Rignot and Steffen* (2008) estimates.

One potential cause for the discrepancies seen this can be found by considering the across-shelf averaged ice thickness of the ice shelves. *Rignot and Steffen* (2008) found the ice shelf to be around 600 m at the grounding line, thinning to around 200 m at 20 km down stream of the grounding line and around 60 m at the ice front (Fig. 6.11a). In the model domain however, the ice shelf averages approximately 400 m at the grounding line, 150 m after 20 km and around 60 m at the ice front (Fig. 6.11b).

This means that the ice shelf in the model does not sit as deep in the water column, meaning less of the ice base is in the warmer water, leading to a decrease in thermal forcing for these areas and hence, lower melt rates. There are two possibilities for the difference in ice shelf thicknesses. Firstly the calibration used to create the model domain might not be accurate enough, resulting in too shallow a draft. Secondly the *Rignot and Steffen* (2008) draft may be too deep.

There is however a more plausible reason to the weaker melt rates seen in the model and this is linked to the discussion in the previous section. The circulation is much weaker, approximately a factor of 5, within the model than that observed by *Johnson et al.* (2011). This means that the heat transport into the cavity will be greatly reduced. A reduced transport of heat will, in turn, lead to reduced basal melt rates, similar to that seen in the model estimates. The reason for the weaker circulation is most likely caused by an absence of vertical mixing as discussed previously.

With the modelled circulation being only approximately 20% of that observed by *Johnson et al.* (2011), and the boundary conditions being roughly consistent between the model and observations, the modelled heat transport into the cavity will also be only 20% of the observed heat transport. However a comparison of mean melt rates find the model to have approximately 66% of the melting calculated by *Rignot and Steffen* (2008). This indicates that the realistic model is approximately 3.5 times too efficient modelling melting at the base of ice shelves.

6.3.3 Discussion

There is a level of agreement between melting in the realistic model and melting in the idealised domain. The channels focus melting and ocean surface layer flow on their right hand slopes, as seen in idealised cases with small numbers of channels in Chapter 4. There is also spatial agreement between the realistic model and the

calculated melt rates of *Rignot and Steffen* (2008), however there is a discrepancy between the size of both the maximum melt rates and the mean melt rates.

The circulation pattern is consistent between the idealised and realistic models, with a strong eastern boundary current forming underneath the ice shelf and the presence of an anticyclonic circulation north of the ice face. There is not a good level of consistency between the realistic model and the observations of *Johnson et al.* (2011), with the observed circulation being approximately 5 times stronger. The stronger observed circulation results in a larger heat flux into the cavity, explaining the higher melt rates calculated by *Rignot and Steffen* (2008).

There are several possible explanations for the difference in ocean circulation, including the exclusion of external drivers such as wind and tides, chosen boundary conditions not providing the flow into the fjord as observed by *Johnson et al.* (2011), and the chosen salinity and potential temperature profiles for water entering the domain may have been too idealised. However the most likely cause of the differences is the lack of vertical mixing within the model.

Further mixing, using a vertical mixing scheme such as the Pacanowski/Philander scheme, would improve the ocean structure within the ice shelf cavity, as well as provide boundary layer mixing to help form the boundary layer observed by *Rignot and Steffen* (2008) in their through-ice profile.

6.4 Effect of ice shelf calving

As previously discussed, recent calving events at Petermann Glacier have caused the ice front to retreat further than previously recorded (*Falkner et al.*; *Johannessen et al.*, 2011; *Münchow et al.*, 2014). Whether this is previously unrecorded natural variability or the beginning of an irreversible retreat and collapse of the ice shelf is unknown. To investigate how the calving events in 2010 and 2012 may have changed fjord circulation and basal melting, the model ice shelf was 'calved' such that the

ice front is at the approximate location of Petermann Glacier following these calving events (denoted by orange lines in Fig. 6.12). The impact of potential further calving events are investigated by 'calving' the ice shelf further (denoted by yellow lines in Fig. 6.12).

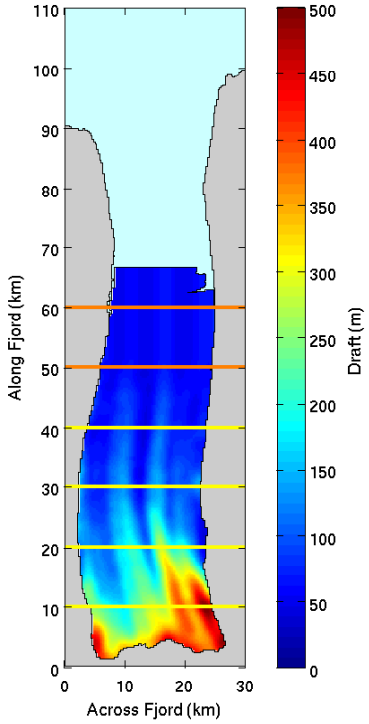

Figure 6.12: Ice shelf topography with approximate locations of 2010 and 2012 calving denoted by orange lines and the locations of further hypothetical calving events denoted by yellow lines.

6.4.1 Stratified water column

Figure 6.13 shows the basal melting and sub-ice layer velocities for the full ice shelf, the 2012 calving event and the calving events which retreat the ice front to the 20 km location. It can be seen that in agreement with the findings in Chapter 5, as the ice front is retreated, basal melting patterns and amplitudes upstream of the new ice front are unaffected, leading to an increase in mean basal melt rate, whilst the total volume of ice melted decreases.

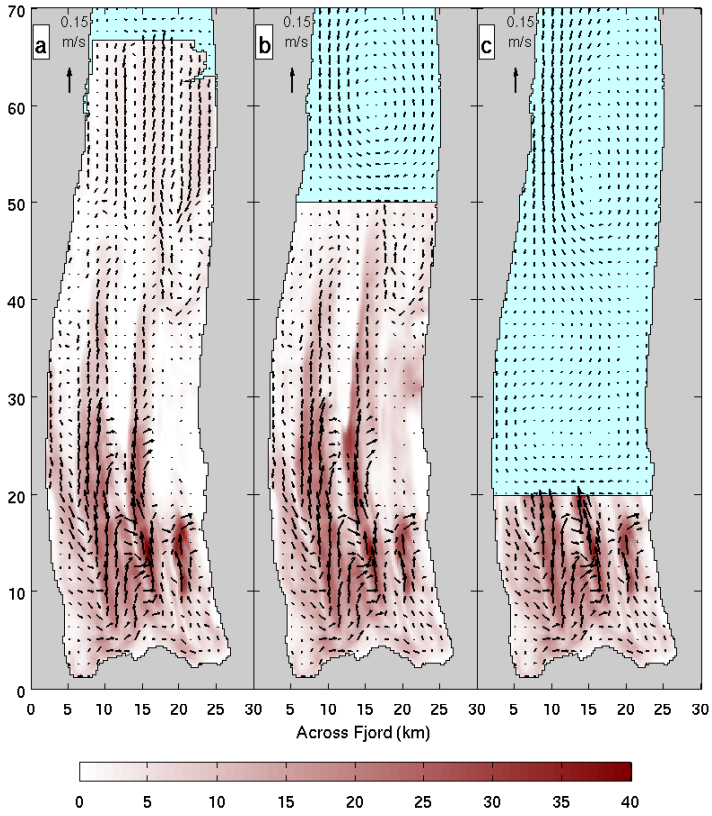

Figure 6.13: Basal melting (m/a) and sub-ice layer velocities (m/s) for the a) full ice shelf, b) 2012 calving event and c) collapse back to the 20 km location.

For the initial calving, the area of ice shelf removed has a shallow draft and is sitting in cooler, fresher water. This means that we are removing areas of little melt, resulting in only a small decrease in the total volume of ice melted. As further calving occurs, deeper drafts with higher melt rates are removed, resulting in a larger decrease in total volume of ice melted.

The reduction in the total volume of ice melted leads to a decrease in freshwater mixed into the meltwater layer, hence reducing the buoyancy and meltwater layer speed. This leads to a decrease in the barotropic circulation (Fig. 6.14). For the initial calving, where the ice is thin and the reduction in ice volume melted is small, the approximate location and extent of the cyclonic and anticyclonic circulations remains constant, with a reduction in strength the main difference.

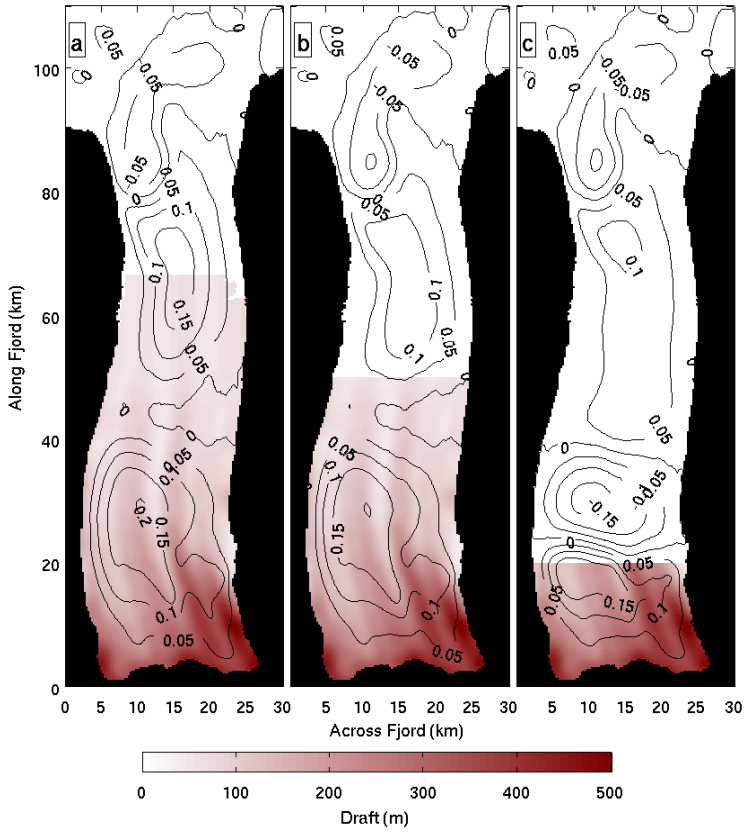

Figure 6.14: Barotropic stream function (contours) overlying ice draft (colored) for the a) full ice shelf, b) 2012 calving event and c) collapse back to the 20 km location.

As further calving occurs, removing deeper ice, both the ice front deepens, and the volume of ice melted decreases at a greater rate. In these cases an anticyclonic circulation is set up just downstream of the ice front (Fig. 6.14c). This is caused by the conservation of potential vorticity causing a westward flow after the large step in ice draft, as explained in Chapter 4.

The reduction in total ice volume can be seen in the potential temperature anomaly profiles (Fig. 6.15). As the ice shelf is calved, the anomaly becomes smaller and the plume becomes narrower as it detaches from the ice base and flows along the pycnocline.

Figure 6.16 shows the relationship between ice shelf length and (a) mean basal melt rate, (b) mean ice front melt and (c) total volume of ice melted. It can be

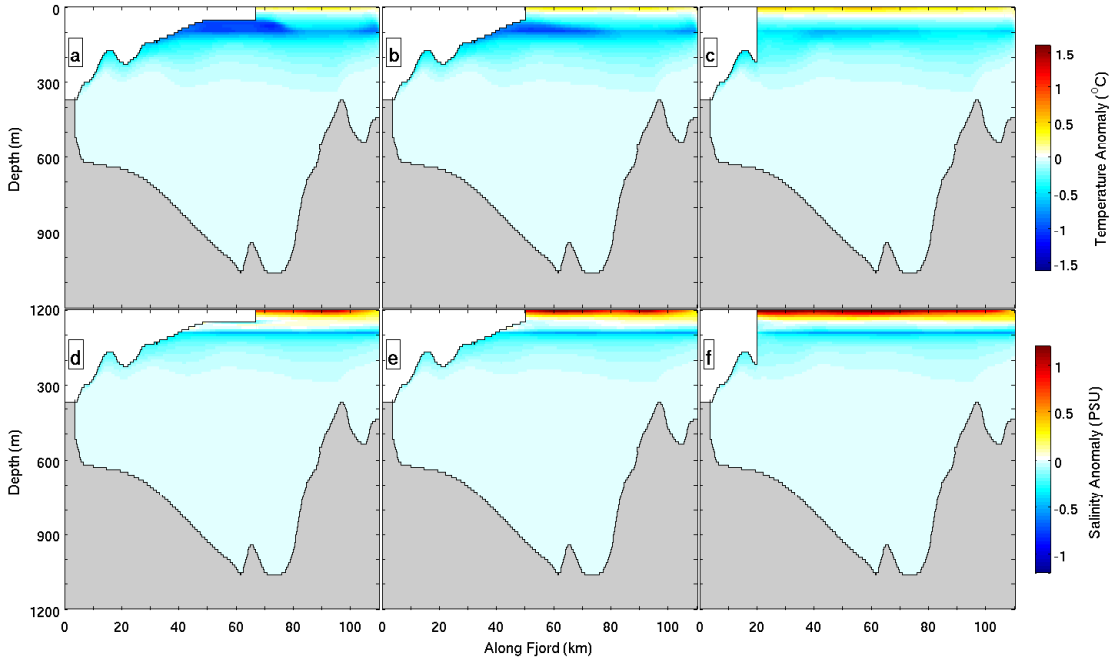

Figure 6.15: Potential temperature anomaly profiles along the centre of the domain for the a) full ice shelf, b) 2012 calving event and c) collapse back to the 20 km location and salinity anomaly profiles along the centre of the domain for the d) full ice shelf, e) 2012 calving event and f) collapse back to the 20 km location.

seen that as the ice shelf decreases in length, the mean basal melt rate increases, until the ice shelf reaches a length of 20 km, after which it begins to decrease. This is due to the initial calving events removing areas of low melt rate, however at 20 km the areas with large melt rates are removed, leading to a decrease in melt rate. The mean melt rate of the first 20 km of ice shelf remains constant, indicating that calving events do not have an impact on melt rates upstream of the calving location. This relationship is in agreement with the results in Chapter 5.

The mean melt rate on the ice front is found to increase as the ice shelf retreats. This is due to the ice front becoming deeper with each calving event, meaning ice front begins to sit in the warmer water beneath the pycnocline, leading to an increase

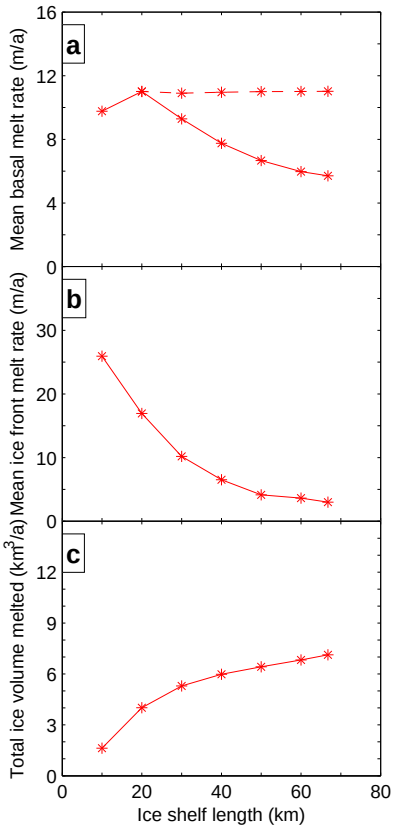

Figure 6.16: Relationship between ice shelf length and a) mean basal melt rate (solid line - whole ice shelf, dashed line - first 20 km), b) mean ice front melt and c) total volume of ice melted.

in melt rates. The initial calving events have a smaller effect as the ice front is still shallow enough to sit wholly within the cooler surface water.

The total ice volume melted takes into account melting on both the ice front and ice base. The total volume is monotonically decreasing as the ice is calved, with a smaller decrease for initial calving events, as mentioned above. The relationship shows that, although the melt rates are greater on the ice front than on the base, the volume of ice melted on the ice front is not enough to counteract the loss of ice melted from the ice base.

6.4.2 Unstratified water column

The increase seen above in mean basal melt rate as the ice shelf retreated was attributed to the removal of ice shelf sitting in cooler water, hence increasing the mean thermal forcing ($T - T_b$). However it could also be attributed to an increase in mean basal gradient with the removal of the flatter section of the ice shelf. To investigate whether it was correct to attribute the change in mean melt rate to thermal forcing, the calving simulations were run again, however this time with unstratified restoring conditions. That is the model is now restored on all ocean boundaries to a water column with a constant potential temperature of 0.3 °C. Note that the spun-up ocean is not unstratified, it is the restoring conditions which are unstratified. It takes approximately 2 weeks for water from the boundary to reach the interior of the domain, meaning that the one year spin up time is sufficient to test this hypothesis.

Figure 6.17 shows the melt rates and sub-ice layer velocities for the unstratified restoring. It can be seen that patterns of both melt and sub-ice layer flow are similar to the stratified restoring cases (Fig. 6.13), however the melt rates are larger, and sub-ice layer flow faster, for the unstratified restoring cases. The mean melt rates for the ice shelf are larger than for the stratified water column (11.98 m/a vs. 5.39 m/a), due to the larger thermal forcing felt by the ice shelf and the corresponding increase in mixed layer speed due to the increase in melt water. Close to the grounding line there is the same pattern of melt rates, since, for all cases, the deeper ice is sat within warmer water. The unstratified water column removes the insulating effect of the stratified layer, resulting in larger melt rates near the ice front. Therefore initial calving events do not result in the increase in mean melt rate previously seen. Further calving continues to remove areas with high melt rates, resulting in a relatively constant mean melt rate.

The barotropic stream functions for the unstratified restring cases (Fig. 6.18)

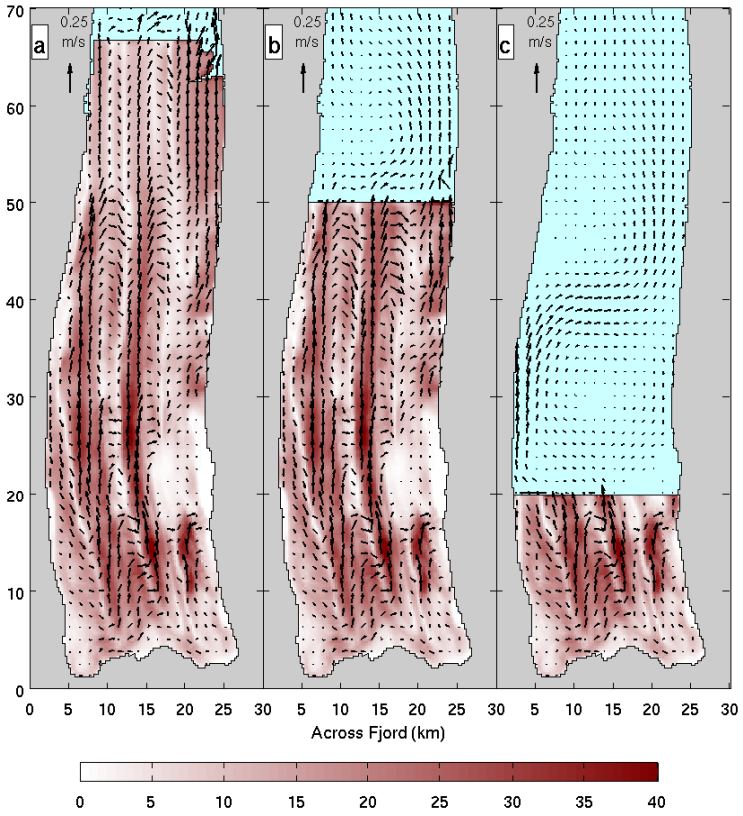

Figure 6.17: Basal melting (m/a)and sub-ice layer velocities (m/s) for the a) full ice shelf, b) 2012 calving event and c) collapse back to the 20 km location, with an unstratified water column.

show stronger cyclonic circulation within the ice shelf cavity and the fjord, along with a stronger anticyclonic circulation in the open ocean section of the fjord than seen in the stratified restoring cases (Fig. 6.14). This increased strength of circulation is caused by a larger level of basal melting, releasing a larger volume of freshwater into the meltwater layer, increasing the buoyancy flux, leading to faster flow.

The initial calving reduces the strength of the circulation slightly, however the lateral extent of the circulation remains constant. This implies a slight decrease in overall ice volume melted, similar to the stratified case. Further calving (Fig. 6.18c) results in the formation of an anticyclonic circulation within the fjord, similar to Figure 6.14c, due to the steep increase in water column thickness as water flows out

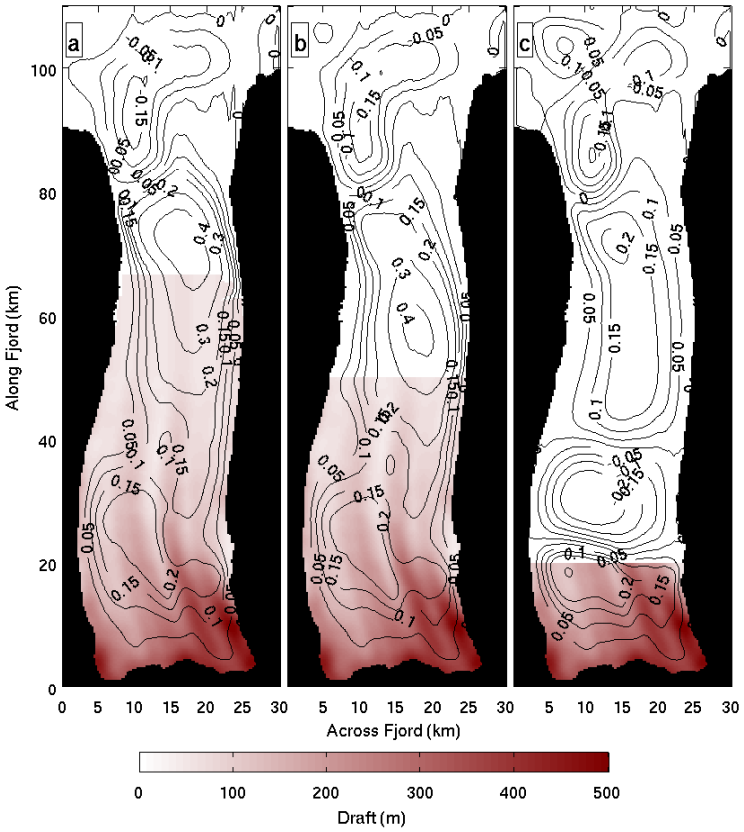

Figure 6.18: Barotropic stream function (contours) overlying ice draft (colored) for the a) full ice shelf, b) 2012 calving event and c) collapse back to the 20 km location, with an unstratified water column.

from under the ice.

The difference in overturning circulation can be seen by comparing the potential temperature and salinity anomalies (Fig. 6.19) with those for the stratified water column restoring (Fig. 6.15). It can be seen that without the presence of a restored pycnocline, the meltwater layer follows the ice base to the ice front, after which it reaches the surface rather then flowing along the pycnocline. The anomaly is larger for the initial unstratified cases compared to their respective unstratified cases, due to the increase in total melted volume. For the later cases where the ice draft is deep, meaning the basal melt rates are similar for both the stratified and unstratified cases, the strength of the anomalies is comparable.

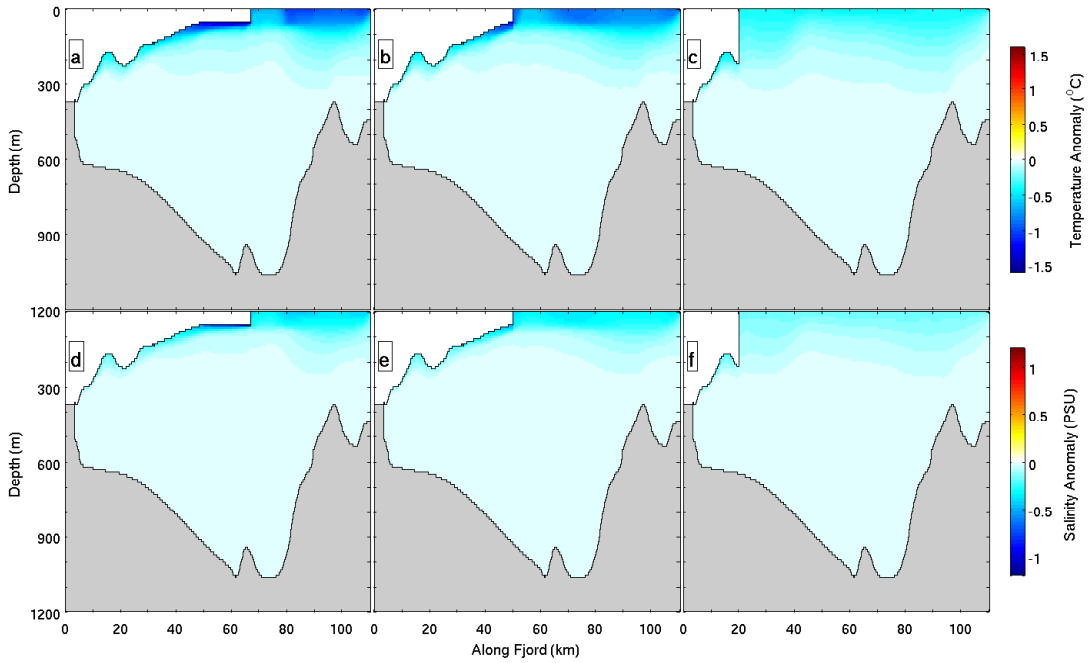

Figure 6.19: Potential temperature anomaly profiles along the centre of the domain for the a) full ice shelf, b) 2012 calving event and c) collapse back to the 20 km location and salinity anomaly profiles along the centre of the domain for the d) full ice shelf, e) 2012 calving event and f) collapse back to the 20 km location.

Figure 6.20 shows the relationship between ice shelf length and (a) mean basal melt rate, (b) mean ice front melt and (c) total volume of ice melted, for the stratified (red) and unstratified water columns.

The whole ice shelf mean melt rate is less sensitive to calving events under unstratified conditions when compared to stratified conditions. This is due to the removal of the cooler insulating layer present under stratified conditions. The sensitivity of the mean melt rate of the first 20 km, not affected by the insulating layer, is in close agreement for both conditions. The levels of melt are greater or the unstratified conditions due to the reasons already given.

The sensitivity of mean ice front melt rate to calving is consistent between both

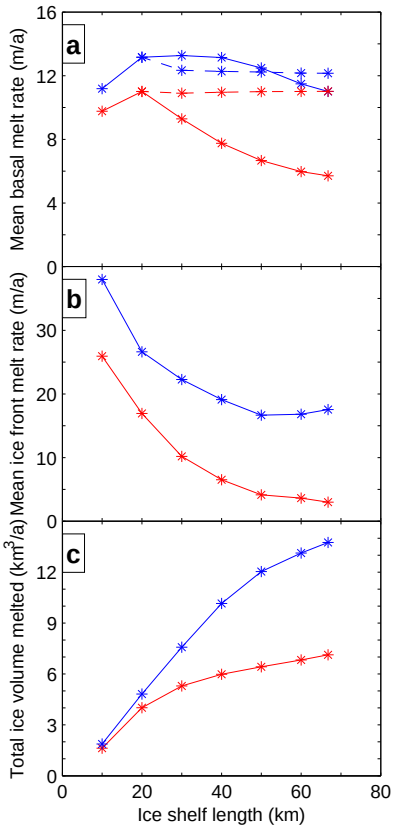

Figure 6.20: Relationship between ice shelf length and a) mean basal melt rate (solid line - whole ice shelf, dashed line - first 20 km), b) mean ice front melt and c) total volume of ice melted, for a stratified water column (red) and an unstratified water column (blue).

conditions. However under both conditions the total volume of ice melted decreases with calving (Fig. 6.20c), indicating that the increase in ice front melting is insufficient to counterbalance the loss of basal ice melt volume due to calving.

As the sensitivity of mean basal melt rate changes between the two conditions, whilst the ice base gradient remains constant across comparable simulations,it can therefore be concluded that the increase in mean basal melt rate with calving, seen under stratified conditions, is due to the influence of the cooler insulating layer that intrudes under the shallower ice front of the ice shelf.

6.4.3 Ice front undercutting

As we have seen above, as the ice shelf retreats, levels of ice front melting increase, with larger levels of ice front melting occurring in the unstratified water case. *O'Leary and Christoffersen* (2013) have shown that for tidewater glaciers, undercutting caused by ice front melt can lead to calving, up to ten times the length of the undercut upstream of the ice front. It is possible that a similar mechanism could happen for ice shelves. In Section 5.4 it was shown that as the idealised ice shelf retreated, an increase in ice front undercutting was found, leading to potential further calving events.

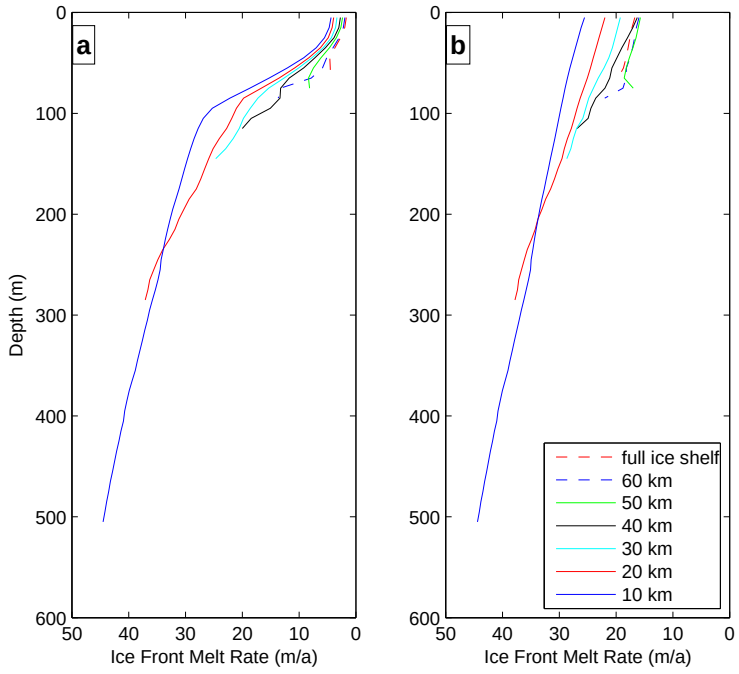

Figure 6.21: Ice front melt induced undercutting for all calving simulation for a) stratified water column and b) unstratified water column.

Figure 6.21 shows the across-shelf mean ice-front melt rates, with the difference between the surface and base melt rates representing the total undercutting. It can be seen that there is undercutting occurring in both the stratified and unstratified

water columns, with the degree of undercutting increasing as the ice shelf retreats, similar to that seen in Section 5.4.

The melt rates near the surface for the unstratified cases are larger than for the stratified cases, whilst the melt rates near the ice front base are similar in both situations. This results in a larger undercutting when the water column is stratified. This suggests that although the mean ice front melt rates are lower for the stratified water column cases, they have the potential to have larger undercutting induced calving events than for the warmer unstratified cases.

6.4.4 Discussion

Initial calving events remove areas of thinner ice with a low basal melt. This leads to an increase in mean basal melt rate. This initial increase in mean basal melt rate is caused by the cooler intruding surface layer which insulates the thinner ice near the ice front. When calving continues and the ice shelf draft becomes deeper than the pycnocline depth, the mean thermal forcing of the ice shelf is increased, leading to an increase in mean melt rates. The basal mean melt rate of the first 20 km of the ice shelf remains constant, indicating that calving events do not have an impact on ice-ocean interactions upstream of the calving location in this model.

However, although the mean basal melt rate is increasing, the area of ice shelf over which this melting occurs is decreasing at a faster rate, resulting in a decrease in total volume of ice melted by basal melting. At the same time the mean ice front melt rate is increasing, but not by enough to counterbalance the decrease in basal melting, meaning the total volume of ice lost via ocean-induced melting decreases as the ice shelf retreats.

The model suggests that the calving events of 2010 and 2012 have had little effect on the pattern of basal melt rates, or on the total volume of ice melted by the ocean. As the undercutting is minimal for these cases, it also suggests there would

be minimal level of further undercutting-induced calving events.

As our model is stable, i.e. it's draft and extent do not evolve in time in response to basal melting, and does not include a coupled ice sheet model, it is not possible to infer the impact of calving on the flow across the grounding line. However, if we assume that it remains constant, or possibly increases slightly due to a decrease in back stress, and that the level of surface melting stay constant, the reduction seen in total ice volume melted would suggest that it is possible for the ice shelf to thicken and potentially re-advance. It should be noted however that in calving the ice shelf, more of the fjord becomes open water, which could allow for further changes in the water column profile due to enhanced wind mixing. It could also allow a larger ice mélange in front of the ice shelf, which could potentially increase back stress on the ice shelf.

The potential for further calving caused by ice front undercutting increases with ice shelf retreat, with the undercutting more pronounced for the stratified water column. This suggests that calving of ice shelves floating in a water column with a large stratification are at greater risk of further calving, compared to those floating in a warmer, less stratified, water column.

Chapter 7

Conclusions

Ice shelves play an important role in the mass balance of an ice sheet, by providing a link between the ocean and ice. Melting at the base of an ice shelf can play a vital role in its mass balance and stability. Topographic channel features have been found on the base of ice shelves, and have been found to alter melting, however the mechanism behind this alteration is unknown. Here MITgcm has been used to investigate the impact of topographic channels on ice-ocean interactions beneath an idealised and realistic ice shelf.

I find that the inclusion of channels alters the flow of the sub-ice layer beneath the ice shelf, changing the focus and intensity of the melt. In agreement with the findings of *Gladish et al.* (2012), the overall mean melt rate decreases as the number of channels increases. Further to this I find that, for a small number of larger channels, this sensitivity of mean melt rate to channel number is high, but for a greater number of smaller channels this sensitivity drops. This change in sensitivity is linked to a change in flow regime beneath the ice shelf.

When there are no basal channels present, a geostrophically balanced flow is set up beneath the ice shelf. There is an intensified eastern boundary current with the highest melt rates occurring beneath this flow. The initial introduction of large channels modifies the formation of the boundary current, inducing a circulation

within each channel. This circulation consists of a southward flow on the western slope of the channel and a northward flow on the eastern slope. There is little flow in the channel crests. There is some transfer over the keels between the channels in an eastward direction, which leads to slightly faster flows in the more easterly channels.

Due to the velocity dependence of melting the highest melt rates occur beneath the strongest flow. This means that for a small number of large channels, the melt rate has been redistributed from against the eastern boundary to along the eastern slope of each channel. The high sensitivity found for these cases is caused by the addition of "no flow" regions. These are regions of the ice shelf where there is little or no flow and are situated beneath crests and keels where the isopycnals are flat. As further channels are added, so are more "no flow" regions, whilst the geostrophic flow on the channel slopes remains the same. This leads to a decrease in mean sub-ice layer flow and therefore basal melting.

As further channels are added and the channels narrow, there becomes a point where the sheared geostrophic circulation within the channel is no longer viable. At this point it is replaced by an overturning circulation with a northward flow in the channel crests and no flow over the channel keels. This in turn alters the location of melting to within channel crests. This is much less sensitive to the channel width due to the increase in "no flow" area being smaller, reducing the mean basal melt rate sensitivity to number of channels.

Although the presence of basal channels increases the mechanical instability of an ice shelf (*Rignot and Steffen*, 2008; *Vaughan et al.*, 2012), the addition of channels is found to decrease an ice-shelf's susceptibility to basal melting. This occurs for two reasons, firstly, the melting is more evenly distributed over the ice shelf and, secondly, the mean melt rate decreases. This stabilising effect is a possible explanation as to why basal channels are observed in warm-water ice shelves in Greenland and Antarctica. If the channels stabilise ice shelves, ice shelves with channels are more

likely to persist, and a 'survivor bias' makes them more likely to be observed.

These findings suggest that there is a fine balance between the increase in mechanical instability and the decrease in susceptibility to basal melting. Without the presence of these channels then the high melt rates beneath the boundary current would have melted through the ice shelf causing it to collapse. Should conditions change such that basal melting were to increase, then the combination of increased melting and mechanical instability may cause the ice shelf to collapse.

To assess the susceptibility of Petermann Glacier to potential future changes in Petermann Fjord a suite of idealised simulations was completed. These focused on changing the stratified surface layer, a warming of the subsurface waters and large calving events.

The stratified layer was found to provide a protruding insulative layer beneath the shallower regions of the ice shelf. The meltwater layer follows the base of the ice shelf until it reaches the pycnocline, at which point it detaches from, and flows away from, the ice shelf. As melt rates are dependent on the velocity of the flow beneath the ice shelf, when the meltwater layer detaches, this flow is removed from the ice base and basal melting significantly reduces.

The impact of changing the depth of this stratified layer, be it permanent or seasonal, is to change the depth at which the meltwater layer detaches from the ice shelf, altering the area of the ice shelf in contact with this layer. Were the stratification layer to deepen, a larger proportion of the ice shelf near to its terminus will be insulated from the meltwater layer, and hence basal melting. This could lead to a thickening of the ice shelf near the ice front, reducing the mechanical instability with the potential for ice shelf growth. Conversely if the stratification layer were to shallow, basal melting will occur closer to the ice front, causing it to thin and further decrease it's mechanical stability.

Should the warming signal observed by *Johnson et al.* (2011) continue and reach

the levels of warming observed at Jakobshavn Isbræ (*Holland et al.*, 2008a), then the model predicts that the levels of basal melting will increase in a near linear fashion. This is contrary to the findings of *Johnson et al.* (2011) who concluded there is currently excess heat supplied to the cavity for the estimated levels of basal melting. Significantly, melt rates near to the grounding line would increase, leading to a thinning of the ice shelf in this area. This could lead to am increase in ice shelf instability and increase the possibility of large calving events, such as those seen in 2010 and 2012, and even ice shelf collapse and the acceleration of the grounded ice section of Petermann Glacier. This would be similar to the observations at Jakobshavn Isbræ (*Holland et al.*, 2008a; *Weidick et al.*, 2004).

This has a potentially significant impact on the northern section of Greenland Ice Sheet. Should the warming signal both continue to propagate around the northern coastline of Greenland and intensify, then the remaining ice shelves in this region may collapse. This would in turn cause an acceleration of this regions outlet glaciers, causing an increase in the mass loss of the ice sheet.

The impact of large calving events on Petermann Glacier was modelled, and it was found that as the ice shelf retreated, the mean basal melt rate increased. This was caused by the removal of areas of the ice shelf which have a shallower draft and were hence insulated from the meltwater layer. However the ice shelf decreased at a larger rate than the mean basal melt rate increased, leading to a reduction in ice volume lost by basal melting. Under the assumption that the flux across the grounding line were to remain constant (it is more likely it will increase due to the reduction in buttressing), then there would be an increase in ice shelf mass balance leading to a potential re-advancement towards the initial ice front position. The model simulations however only consider ice shelf retreat without a warming signal. Were the two to occur simultaneously, akin to the conditions at Jakobshavn Isbræ, it is possible that the increased basal melting might balance or surpass the flux of

ice across the grounding line, causing further collapse and glacier acceleration.

One consequence of ice shelf retreat is a deepening of the draft at the ice front. This results in the ice front coming into contact with the deeper warmer waters, leading to large melt rates on the ice front and melting induced undercutting. The volume of ice melted from the ice front is smaller than the decrease in volume melted by basal melting, leading to an overall reduction in ice volume melted as the ice shelf retreats. Melting-induced undercutting causes a flexing of the ice front as it tries to readjust to hydrostatic equilibrium. This flexing causes an increase in surface stress near the ice front, promoting ice fractures and hence further calving.

O'Leary and Christoffersen (2013) found that the degree of further calving is dependent on the size of the undercutting of the ice front. However to be solely responsible for further ice shelf retreat, the melt induced undercutting would have to cause calving up to 20 times it's own magnitude upstream from the ice front. This estimate is much greater than any estimate modelled by *O'Leary and Christoffersen* (2013), and implies that a combination of ice shelf retreat and increased subsurface warming would be required to prevent ice shelf re-advancement.

The study shows that although channels have a stabilising effect on ice shelves, they do not protect them from future changes in ocean warming, changes in water column stratification or large calving events.

When considering the impact of changes to oceanic forcing on Greenland Ice Sheet as a whole, it is necessary to consider both ice shelves and tidewater glaciers. A warming ocean would have a detrimental effect on both types of outlet glacier. Ice shelves would undergo greater basal melting with the potential for ice shelf thinning and retreat. Whilst tidewater glacier will undergo greater melting on the base of their vertical ice fronts, causing greater melt-induced undercutting and hence further calving. Both cases would result in glacier acceleration, increasing the export of ice away from the ice sheet and hence resulting in a negative mass balance.

The impact of changes to the stratification depth are a little more complicated. Should the stratification depth increase in the fjords around Greenland, ice shelves would become more stable due to a decrease in basal melting. However the differential between melting at the surface and bottom at the terminus of a tidewater glacier would increase. This in turn would lead to an increase in undercutting and, following the work of *O'Leary and Christoffersen* (2013), an increase in calving upstream of the terminus.

Conversely a decrease in stratification depth would cause ice shelves to thin and potentially retreat, whilst the differential in melt rates on the vertical face of a tidewater glacier would decrease, resulting in a reduction in calving. As calving can occur upstream of the terminus up to a factor of four times the undercutting depth, a decrease in calving can be substantially greater than an increase in ice front melting. Therefore the impact of stratification depth on the mass balance of Greenland Ice Sheet would take careful consideration and each marine terminating outlet glacier would need to be considered individually.

Modelling of a realistic Petermann Glacier domain in MITgcm provided a level of agreement with the idealised model in terms of channelised flow, basal melt location and ocean circulation. This agreement helps substantiate the findings of the idealised model and allows for their findings to be interpreted onto real world situations.

However large discrepancies became apparent when comparing the realistic model to the observations of *Johnson et al.* (2011) and *Rignot and Steffen* (2008). The structure of the modelled circulation within the fjord was vastly different to that observed by *Johnson et al.* (2011) and the modelled circulation was a approximately five times slower than the observations.

This was most likely caused by the lack of mixing present in the ocean, due to constant ocean parameters being chosen rather than a vertical mixing closure scheme. Other potential causes include unrealistic boundary conditions and the exclusion of

external drivers such as tides and wind.

This reduction in circulation resulted in a smaller transport of heat into the cavity, leading to the smaller melt rates modelled when compared to those of *Rignot and Steffen* (2008). A comparison in the reduction of heat transport and mean melt rate suggests that the model is approximately 3.5 times too efficient at basal melting.

Further studies to improve the realistic model, so that comparisons with observations are more meaningful and predictions made with the model are more robust, require the consideration of several factors.

Firstly a vertical mixing scheme, such as the Pacanowski/Philander scheme, needs to be implemented to ensure there is sufficient vertical mixing within the water column to capture all of the relevant processes.

The boundary conditions, both in terms of flow into the domain and prescribed salinity/potential temperature profiles need careful consideration. These have the potential to alter both the structure and magnitude of the circulation within the domain to become more aligned with observations. External drivers such as tides and winds would also enhance the realistic model by providing further sources of missing mixing.

To fully test the impact of the physical processes described here requires a coupled model with an evolving ice sheet. Nevertheless the principle conclusions contained within this thesis are believed to be robust.

Bibliography

Aagaard, K., and E. C. Carmack (1989), The role of sea ice and other freshwater in the Arctic circulation, *Journal of Geophysical Research*, *94*, 14,485–14,498. 1.4.2

Adcroft, A., C. Hill, and J. Marshall (1997), Representation of Topography by Shaved Cells in a Height Coordinate Ocean Model, *Monthly weather review*, *125*(9), 2293–2315, doi:10.1175/1520-0493(1997)125¡2293:ROTBSC¿2.0.CO;2. 3.3.2

Bamber, J. L., and R. L. Layberry (2001), A new ice thickness and bed data set for the Greenland ice sheet. 1. Measurement, data reduction and errors, *Journal of Geophysical Research*, *106*, 33,773–33,780. 1.4.1

Bamber, J. L., J. A. Griggs, R. T. W. L. Hurkmans, J. A. Dowdeswell, S. P. Gogineni, I. Howat, J. Mouginot, J. Paden, S. Palmer, E. Rignot, and D. Steinhage (2013), A new bed elevation dataset for Greenland, *The Cryosphere*, *7*, 499–510, doi:10.5194/tc-7-499-2013. 1.2

Benn, D. I., C. R. Warren, and R. H. Mottram (2007), Calving processes and the dynamics of calving glaciers, *Earth-Science Reviews*, *82*, 143–179, doi:10.1016/j.earscirev.2007.02.002. 1.2.3

Bersch, M., I. Yashayaev, and K. P. Koltermann (2007), Recent changes of the thermohaline circulation in the subpolar North Atlantic, *Ocean Dynamics*, *57*(3), 223–235, doi:10.1007/s10236-007-0104-7. 1.2.4

Bjørk, A. A., K. H. Kjær, N. J. Korsgaard, S. A. Khan, K. K. Kjeldsen, C. S. Andresen, J. E. Box, N. K. Larsen, and S. Funder (2012), An aerial view of 80 years of climate-related glacier fluctuations in southeast Greenland, *Nature Geoscience*, *5*(6), 427–432, doi:10.1038/ngeo1481. 1.2.4

Box, J., L. Yang, D. Bromwich, and L. Bai (2009), Greenland Ice Sheet Surface Air Temperature Variability: 1840-2007*, *Journal of Climate*, *22*(14), 4029–4049, doi:10.1175/2009JCLI2816.1. 1.2.3

Box, J. E., and D. T. Decker (2011), Greenland marine-terminating glacier area changes: 20002010, *Annals of Glaciology*, *52*(59), 91–98, doi:10.3189/172756411799096312. (document), 1.4.5

Box, J. E., X. Fettweis, J. C. Stroeve, M. Tedesco, D. K. Hall, and K. Steffen (2012), Greenland ice sheet albedo feedback: thermodynamics and atmospheric drivers, *The Cryosphere*, *6*, 821–839, doi:10.5194/tc-6-821-2012. 1.2.4

Brunt, K. M., E. A. Okal, and D. R. MacAyeal (2011), Antarctic ice-shelf calving triggered by the Honshu (Japan) earthquake and tsunami, March 2011, *Journal of Glaciology*, *57*(205), 785–788, doi:10.3189/002214311798043681. 1.2.3

Chen, J. L., C. R. Wilson, and B. D. Tapley (2011), Interannual variability of Greenland ice losses from satellite gravimetry, *Journal of Geophysical Research*, *116*, B07,406, doi:10.1029/2010JB007789. 1.2.4

Christoffersen, P., R. I. Mugford, K. J. Heywood, I. Joughin, J. A. Dowdeswell, J. P. M. Syvitski, A. Luckman, and T. J. Benham (2011), Warming of waters in an East Greenland fjord prior to glacier retreat: mechanisms and connection to large-scale atmospheric conditions, *The Cryosphere*, *5*(3), 701–714, doi:10.5194/tc-5-701-2011. (document), 5.3.1

Copland, L., D. R. Mueller, and L. Weir (2007), Rapid loss of the Ayles Ice Shelf, Ellesmere Island, Canada, *Geophysical Research Letters*, *34*(21), 1–6, doi:10.1029/2007GL031809. 1.2.4

CReSIS (2014), Centre for Remote Sensing of Ice Sheets, accessed 25 Feb 2014, *www.cresis.kdu.edu*. 2.1.2

De Rydt, J., P. R. Holland, P. Dutrieux, and A. Jenkins (2014), Geometric and oceanographic controls on melting beneath Pine Island Glacier, *Journal of Geophysical Research Oceans*, *119*, 2420–2438, doi:10.1002/2013JC009513. 6.2.3

Dutrieux, P., D. G. Vaughan, H. F. J. Corr, A. Jenkins, P. R. Holland, I. Joughin, and A. Fleming (2013), Pine Island Glacier ice shelf melt distributed at kilometre scales, *The Cryosphere*, *7*, 1543–1555, doi:10.5194/tc-7-1543-2013. (document), 1.2.3, 1.3.2, 4, 4.3

Ekholm, S. (1996), A full coverage, high-resolution, topographic model of Greenland computed from a variety of digital elevation data, *Journal of Geophysical Research*, *101*(B10), 21,961, doi:10.1029/96JB01912. 2.1.3

Falkner, K., H. Melling, A. Münchow, J. Box, T. Wohlleben, H. L. Johnson, P. Gudmandsen, R. Samelson, L. Copland, K. Steffen, E. Rignot, and A. K. Higgins (). (document), 1.2.1, 1.4.1, 1.4.1, 1.4.5, 5, 5.4.1, 6.4

Fettweis, X., M. Tedesco, M. van den Broeke, and J. Ettema (2011), Melting trends over the Greenland ice sheet (19582009) from spaceborne microwave data and regional climate models, *The Cryosphere*, *5*, 359–375, doi:10.5194/tc-5-359-2011. 1.2.4

Gade, H. G. (1979), Melting of Ice in Sea Water: A Primative Model with Application to the Antarctic Ice Shelf and Icebergs, *Journal of Physical Oceanography*, *9*(1), 189–198. 1.3.1

Giles, K., S. Laxon, and A. Ridout (2008), Circumpolar thinning of Arctic sea ice following the 2007 record ice extent minimum, *Geophysical Research Letters*, *35*(22), 2006–2009, doi:10.1029/2008GL035710. 1.2.4

Gladish, C., D. Holland, P. Holland, and S. Price (2012), Ice-shelf basal channels in a coupled ice/ocean model, *Journal of Glaciology*, *58*(212), 1227–1244, doi:10.3189/2012JoG12J003. (document), 1.3.2, 4, 4.3, 6.3.1.1, 7

Gogineni, S., D. Tammana, D. Braaten, C. Leuschen, T. Akins, J. Legarsky, P. Kanagaratnam, J. Stiles, and K. Jezek (2001), Coherent radar ice thickness measurements over the Greenland ice sheet, *Journal of Geophysical Research*, *106*, 33,761–33,772. 1.4.3

Griggs, J. A., and J. L. Bamber (2011), Antarctic ice-shelf thickness from satellite radar altimetry, *Journal of Glaciology*, *57*(203), 485–498. 2.3

Hanna, E., J. Cappelen, X. Fettweis, P. Huybrechts, A. Luckman, and M. H. Ribergaard (2009), Hydrologic response of the Greenland ice sheet : the role of oceanographic warming, *Hydrological Processes*, *23*, 7–30, doi:10.1002/hyp.7090. 5.3.1

Harig, C., and F. J. Simons (2012), Mapping Greenland's mass loss in space and time., *Proceedings of the National Academy of Sciences of the U.S.A*, *109*, 19,934–19,937, doi:10.1073/pnas.1206785109. 1.2.4

Hellmer, H. H., and D. J. Olbers (1989), A two-dimensional model for the thermohaline circulation under an ice shelf, *Antarctic Science*, *1*(04), 325–336. 3.2, 3.2

Higgins, A. (1991), North Greenland glacier velocities and calf ice production, *Polarforschung*, *60*(1), 1–23. (document), 1.2.1, 1.4.1, 1.4.3, 1.4.5

Hirano, A., R. Welch, and B. Lang (2003), Mapping from ASTER stereo image data: DEM validation and accuracy assessment., *ISPRS Journal of Photogrammetry and Remote Sensing*, *57*, 39–52. 2.1.1

Holland, D., and A. Jenkins (1999), Modeling thermodynamic ice-ocean interactions at the base of an ice shelf, *Journal of Physical Oceanography*, *29*(8), 1787–1800. 1.2.3, 3.2, 3.2, 3.2, 4.2.2, 5.1.3, 5.3.2.1

Holland, D. M., R. H. Thomas, B. De Young, M. H. Ribergaard, and B. Lyberth (2008a), Acceleration of Jakobshavn Isbrætriggered by warm subsurface ocean waters, *Nature Geoscience*, *1*(10), 659–664, doi:10.1038/ngeo316. (document), 1.2.1, 1.2.3, 1.2.4, 1.2.4, 5.3.1, 5.3.3, 5.5, 7

Holland, P., and D. Feltham (2006), The effects of rotation and ice shelf topography on frazil-laden ice shelf water plumes, *Journal of physical oceanography*, *36*(12), 2312–2327. 3.1, 3.1

Holland, P., A. Jenkins, and D. M. Holland (2010), Ice and ocean processes in the Bellingshausen Sea, Antarctica, *Journal of Geophysical Research*, *115*(C5), 1–16, doi:10.1029/2008JC005219. 1.2.4

Holland, P. R., A. Jenkins, and D. M. Holland (2008b), The response of ice shelf basal melting to variations in ocean temperature., *Journal of Climate*, *21*(11), 2558–2572, doi:10.1175/2007JCLI1909.1. (document), 1.2.4, 3.3.3, 4.2.2, 4.2.2, 5.1.3, 5.3.1, 5.3.2.1

Howat, I. M., I. Joughin, and T. A. Scambos (2007), Rapid changes in ice discharge from Greenland outlet glaciers., *Science*, *315*, 1559–1561, doi:10.1126/science.1138478. 1.2.4

Howat, I. M., B. E. Smith, I. Joughin, and T. A. Scambos (2008), Rates of southeast Greenland ice volume loss from combined ICESat and ASTER observations, *Geophysical Research Letters*, *35*(17), L17,505, doi:10.1029/2008GL034496. (document), 5.3.1

ICGEM (2014), International Centre for Global Earth Models (ICGEM), accessed 25 Feb 2014, *http://icgem.gfz-potsdam.de/ICGEM/*. 2.2.1

Jakobsson, M., L. Mayer, B. Coakley, J. A. Dowdeswell, S. Forbes, B. Fridman, H. Hodnesdal, R. Noormets, R. Pedersen, M. Rebesco, H. W. Schenke, Y. Zarayskaya, D. Accettella, A. Armstrong, R. M. Anderson, P. Bienhoff, A. Camerlenghi, I. Church, M. Edwards, J. V. Gardner, J. K. Hall, B. Hell, O. Hestvik, Y. Kristoffersen, C. Marcussen, R. Mohammad, D. Mosher, S. V. Nghiem, M. T. Pedrosa, P. G. Travaglini, and P. Weatherall (2012), The International Bathymetric Chart of the Arctic Ocean (IBCAO) Version 3.0, *Geophysical Research Letters*, *39*(12), doi:10.1029/2012GL052219. 2.4.2.2

Jenkins, A. (1991), A one-dimensional model of ice shelf-ocean interaction, *Journal of Geophysical Research*, *96*(Cll), 671–677, doi:10.1029/91JC01842. 3.2

Jenkins, A. (1999), The Impact of Melting Ice on Ocean Waters, *Journal of Physical Oceanography*, *29*, 2370–2381. 1.3.1

Jenkins, A., P. Dutrieux, S. S. Jacobs, S. D. McPhail, J. R. Perrett, A. T. Webb, and D. White (2010a), Observations beneath Pine Island Glacier in West Antarctica and implications for its retreat, *Nature Geoscience*, *3*(7), 468–472, doi:10.1038/ngeo890. 6.2.3

Jenkins, A., K. W. Nicholls, and H. F. J. Corr (2010b), Observation and Parameterization of Ablation at the Base of Ronne Ice Shelf, Antarctica, *Journal of Physical Oceanography*, *40*(10), 2298–2312, doi:10.1175/2010JPO4317.1. 3.3.3

Johannessen, O. M., M. Babiker, and M. W. Miles (2011), Petermann Glacier, North Greenland: massive calving in 2010 and the past half century, *The Cryosphere Discussions*, *5*(1), 169–181, doi:10.5194/tcd-5-169-2011. (document), 1.4.5, 5, 5.4.1, 6.4

Johnson, H. L., A. Münchow, K. K. Falkner, and H. Melling (2011), Ocean circulation and properties in Petermann Fjord, Greenland, *Journal of Geophysical Research*, *116*(C1), doi:10.1029/2010JC006519. (document), 1.2.1, 1.4.1, 1.4.1, 1.4.2, 1.7, 1.4.2, 1.4.3, 2.4.2.2, 4.1, 4.2.1, 5.2.1, 5.2.1, 5.2.3, 5.3.1, 5.3.3, 5.5, 6, 6.3.2.1, 6.8, 6.3.2.1, 6.3.2.2, 6.3.2.2, 6.3.3, 7

Jungclaus, J. H., and J. O. Backhaus (1994), Application of a transient reduced gravity model to the Denmark Strait overflow, *Journal of Geophysical Research*, *99*, 12,375–12,396. 3.1

Kargel, J. S., A. P. Ahlstrøm, R. B. Alley, J. L. Bamber, T. J. Benham, J. E. Box, C. Chen, P. Christoffersen, M. Citterio, J. G. Cogley, H. Jiskoot, G. J. Leonard, P. Morin, T. Scambos, T. Sheldon, and I. Willis (2012), Greenland's shrinking ice cover: fast times but not that fast, *The Cryosphere*, *6*, 533–537, doi:10.5194/tcd-5-3207-2011. 1.2

Khan, S. A., J. Wahr, M. Bevis, I. Velicogna, and E. Kendrick (2010), Spread of ice mass loss into northwest Greenland observed by GRACE and GPS, *Geophysical Research Letters*, *37*, L06,501, doi:10.1029/2010GL042460. 1.2.4

Koch, L. (1928), Contributions to the glaciology of NOrth Greenland, *Medd. Grønland*, *65*, 181–464. (document), 1.2.1, 1.4.1

Koch, L. (1940), Survey of North Greenland, *Medd. Grønland*, *130*. 1.4.1

Landsat (2010), NASA Landsat Program, Landsat ETM+ scene L72043001_0012001072107, *USGS, Sioux Falls*, *07/21/2001*. 2.1.1

Le Brocq, A. M., N. Ross, J. A. Griggs, R. G. Bingham, H. F. J. Corr, F. Ferraccioli, A. Jenkins, T. A. Jordan, A. J. Payne, D. M. Rippin, and M. J. Siegert (2013), Evidence from ice shelves for channelized meltwater flow beneath the Antarctic Ice Sheet, *Nature Geoscience*, *6*(11), 945–948, doi:10.1038/ngeo1977. 1.3.2

Losch, M. (2008), Modeling ice shelf cavities in a z coordinate ocean general circulation model, *Journal of Geophysical Research*, *113*(C8), doi:10.1029/2007JC004368. 3.3.1, 3.3.2, 3.3.2, 3.3.3, 4.2.1

MacAyeal, D. R., E. A. Okal, R. C. Aster, J. N. Bassis, K. M. Brunt, L. M. Cathles, R. Drucker, H. A. Fricker, Y.-J. Kim, S. Martin, M. H. Okal, O. V. Sergienko, M. P. Sponsler, and J. E. Thom (2006), Transoceanic wave propagation links iceberg calving margins of Antarctica with storms in tropics and Northern Hemisphere, *Geophysical Research Letters*, *33*, L17,502, doi:10.1029/2006GL027235. 1.2.3

Mankoff, K., S. Jacobs, S. Tulaczyk, and S. Stammerjohn (2012), The role of Pine Island Glacier ice shelf basal channels in deep-water upwelling, polynyas and ocean circulation in Pine Island Bay, Antarctica, *Annals of Glaciology*, *53*(60), 123–128, doi:10.3189/2012AoG60A062. (document), 1.3.2, 4

Marshall, J., A. Adcroft, C. Hill, L. Perelman, and C. Heisey (1997a), A finite-volume, incompressible Navier Stokes model for studies of the ocean on parallel computers, *Journal of Geophysical Research*, *102*(C3), 5753, doi:10.1029/96JC02775. 3.3

Marshall, J., C. Hill, L. Perelman, and A. Adcroft (1997b), Hydrostatic, quasi-hydrostatic, and nonhydrostatic ocean modeling, *Journal of Geophysical Research*, *102*, 5733–5752, doi:10.1029/96JC02776. 3.3

McPhee, M. G., G. A. Maykut, and J. H. Morison (1987), Dynamics and thermodynamics of the ice/upper ocean system in the marginal ice zone of the Greenland Sea, *Journal of Geophysical Research*, *92*, 7017–7031. 3.2

Melling, H., T. A. Agnew, K. K. Falkner, D. A. Greenberg, C. M. Lee, A. Münchow, B. Petrie, S. J. Prinsenberg, R. M. Samelson, and R. A. Woodgate (2008), Freshwater fluxes vis Pacific and Arctic outflow across the Canadian polar shelf, in *Arctic-Subarctic Ocean Flux*, edited by R. R. Dickson, J. Meincke, and P. Rhines, pp. 193–261, Springer, Berlin. 1.4.2

Michelsen, D. (2013), Greenland in Figures 2013, *Tech. rep.*, Statistics Greenland. 1.2

Millgate, T., P. R. Holland, A. Jenkins, and H. L. Johnson (2013), The effect of basal channels on oceanic ice-shelf melting, *Journal of Geophysical Research Oceans*, *118*, doi:10.1002/2013JC009402. 5, 4.3

MITgcm (2014), M.I.T General Circulation Model News and Information, accessed 24 Feb 2014, *http://mitgcm.org/*. 3.3

Moon, T., I. Joughin, B. Smith, and I. Howat (2012), 21st-century evolution of Greenland outlet glacier velocities., *Science (New York, N.Y.)*, *336*, 576–8, doi:10.1126/science.1219985. (document), 1.2.1, 1.2.4

Motyka, R. J., L. Hunter, K. A. Echelmeyer, and C. Connor (2003), Submarine melting at the terminus of a temperate tidewater glacier, LeConte Glacier, Alaska, U.S.A., *Annals of Glaciology*, *36*, 57–65, doi:10.3189/172756403781816374. 1.2.3

Motyka, R. J., M. Truffer, M. Fahnestock, J. Mortensen, S. R. Rysgaard, and I. Howat (2011), Submarine melting of the 1985 Jakobshavn Isbræfloating tongue and the triggering of the current retreat, *Journal of Geophysical Research*, *116*, doi:10.1029/2009JF001632. (document), 1.3.2

Münchow, A., and H. Melling (2008), Ocean current observations from Nares Strait to the west of Greenland: Interannual to tidal variability and forcing, *Journal of Marine Research*, *66*, 801–833. 1.4.2, 1.4.2

Münchow, A. M., L. Padman, and H. A. Fricker (2014), Interannual Changes of the Floating Ice Shelf of Petermann Gletscher , North Greenland from 2000 to 2012, *Journal Of Glaciology*, *60*(221), 489–499, doi:10.3189/2014JoG13J135. (document), 1.2.1, 1.4.5, 1.10, 5.4.1, 6.4

Murray, T., K. Scharrer, T. D. James, S. R. Dye, E. Hanna, A. D. Booth, N. Selmes, A. Luckman, A. L. C. Hughes, S. Cook, and P. Huybrechts (2010), Ocean regulation hypothesis for glacier dynamics in southeast Greenland and implications for ice sheet mass changes, *Journal of Geophysical Research*, *115*, F03,026, doi:10.1029/2009JF001522. 1.2.3, 5.3.1

Nick, F., A. Luckman, A. Vieli, C. Van Der Veen, D. Van As, R. Van De Wal, F. Pattyn, A. Hubbard, and D. Floricioiu (2012), The response of Petermann Glacier, Greenland, to large calving events, and its future stability in the context of atmospheric and oceanic warming, *Journal of Glaciology*, *58*(208), 229–239, doi:10.3189/2012JoG11J242. 1.2.3, 5.4.1, 5.4.3

Nick, F. M., A. Vieli, I. M. Howat, and I. Joughin (2009), Large-scale changes in Greenland outlet glacier dynamics triggered at the terminus, *Nature Geoscience*, *2*(2), 110–114, doi:10.1038/NGEO394. 3.3.3

Nick, F. M., A. Vieli, M. L. Andersen, I. Joughin, A. Payne, T. L. Edwards, F. Pattyn, and R. S. W. van de Wal (2013), Future sea-level rise from Greenlands main outlet glaciers in a warming climate, *Nature*, *497*(7448), 235–238, doi:10.1038/nature12068. 1.2.3

O'Leary, M., and P. Christoffersen (2013), Calving on tidewater glaciers amplified by submarine frontal melting, *The Cryosphere*, *7*(1), 119–128, doi:10.5194/tc-7-119-2013. (document), 1.2.3, 3.3.3, 5.4.1, 5.4.3, 6.4.3, 7

Parkinson, C. L., and D. J. Cavalieri (2008), Arctic sea ice variability and trends, 19792006, *Journal of Geophysical Research*, *113*(C7), C07,003, doi:10.1029/2007JC004558. 1.2.4

Payne, A. J. (2004), Recent dramatic thinning of largest West Antarctic ice stream triggered by oceans, *Geophysical Research Letters*, *31*, L23,401, doi:10.1029/2004GL021284. 1.2.3

Payne, A. J., P. R. Holland, A. P. Shepherd, I. C. Rutt, A. Jenkins, and I. Joughin (2007), Numerical modeling of ocean-ice interactions under Pine Island Bay's ice shelf, *Journal of Geophysical Research*, *112*(C10), doi:10.1029/2006JC003733. (document), 1.3.2, 4

Pritchard, H. D., R. J. Arthern, D. G. Vaughan, and L. A. Edwards (2009), Extensive dynamic thinning on the margins of the Greenland and Antarctic ice sheets., *Nature*, *461*(7266), 971–5, doi:10.1038/nature08471. 1.2.4

Pritchard, H. D., S. R. M. Ligtenberg, H. A. Fricker, D. G. Vaughan, M. R. van den Broeke, and L. Padman (2012), Antarctic ice-sheet loss driven by basal melting of ice shelves., *Nature*, *484*(7395), 502–5, doi:10.1038/nature10968. 1.2.3

Rabe, B., A. Münchow, H. L. Johnson, and H. Melling (2010), Nares Strait hydrography and salinity field from a 3-year moored array, *Journal of Geophysical Research*, *115*(C7), C07,010, doi:10.1029/2009JC005966. 1.4.2

Rignot, E. (1998), Hinge-line migration of Petermann Gletscher, north Greenland, detected using satellite radar interferometry, *Journal of Glaciology*, *44*(148), 469–476. (document), 2.1.3

Rignot, E., and S. S. Jacobs (2002), Rapid bottom melting widespread near Antarctic Ice Sheet grounding lines., *Science (New York, N.Y.)*, *296*(5575), 2020–3, doi:10.1126/science.1070942. 1.2.3

Rignot, E., and K. Steffen (2008), Channelized bottom melting and stability of floating ice shelves, *Geophysical Research Letters*, *35*(2), doi:10.1029/2007GL031765. (document), 1.3.2, 1.4.2, 1.4.3, 1.8, 1.4.3, 1.4.4, 1.9, 1.10, 2.4.1, 3.3.1, 4.3, 5.2.1, 5.7, 5.2.2.3, 5.2.2.3, 5.2.3, 6, 6.3, 6.3.2.1, 6.9, 6.3.2.1, 6.3.2.2, 6.10, 6.3.2.2, 6.11, 6.3.2.2, 6.3.3, 7

Rignot, E., S. Gogineni, I. Joughin, and W. Krabill (2001), Contribution to the glaciology of nothern Greenland from satellite radar interferometry, *Journal of Geophysical Research*, *106*, 34,007–34,019. (document), 1.4.1

Rignot, E., M. Koppes, and I. Velicogna (2010), Rapid submarine melting of the calving faces of West Greenland glaciers, *Nature Geoscience*, *3*(3), 187–191, doi:10.1038/ngeo765. 1.2.3, 5.3.1

Rignot, E., I. Fenty, D. Menemenlis, and Y. Xu (2012), Spreading of warm ocean waters around Greenland as a possible cause for glacier acceleration, *Annals of Glaciology*, *53*(60), 257–266, doi:10.3189/2012AoG60A136. (document), 1.2.1, 5.3.1

Rignot, E. J., S. P. Gogineni, W. B. Krabill, and S. Ekholm (1997), North and Northeast Greenland Ice Discharge from Satellite Radar Interferometry, *Science*, *276*(5314), 934–937, doi:10.1126/science.276.5314.934. (document), 1.4.1, 1.4.1

Sasgen, I., M. van den Broeke, J. L. Bamber, E. Rignot, L. S. Sørensen, B. Wouters, Z. Martinec, I. Velicogna, and S. B. Simonsen (2012), Timing and origin of recent regional ice-mass loss in Greenland, *Earth and Planetary Science Letters*, *333-334*, 293–303, doi:10.1016/j.epsl.2012.03.033. 1.2.4

Scambos, T. A., C. Hulbe, M. Fahnestock, and J. Bohlander (2000), The link between climate warming and break-up of ice shelves in the Antarctic Peninsula, *Journal of Glaciology*, *46*(154), 516–530. 1.2.3

Selmes, N., T. Murray, and T. D. James (2011), Fast draining lakes on the Greenland Ice Sheet, *Geophysical Research Letters*, *38*, L15,501, doi:10.1029/2011GL047872. 1.2.3

Sergienko, O. V. (2013), Basal channels on ice shelves, *Journal of Geophysical Research: Earth Surface*, *118*, doi:10.1002/jgrf.20105. 1.3.2

Serreze, M. C., and R. G. Barry (2011), Processes and impacts of Arctic amplification: A research synthesis, *Global and Planetary Change*, *77*(1-2), 85–96, doi:10.1016/j.gloplacha.2011.03.004. 1.2.4

Serreze, M. C., M. M. Holland, and J. Stroeve (2007), Perspectives on the Arctic's shrinking sea-ice cover., *Science (New York, N.Y.)*, *315*(5818), 1533–6, doi:10.1126/science.1139426. (document), 1.2.4, 1.2.4, 5.1.1

Steele, M., D. Thomas, D. Rothrock, and S. Martin (1996), A simple model study of the Arctic Ocean freshwater balance, 1979-1985, *Journal of Geophysical Research*, *101*, 20,833–20,848. 1.4.2

Steffen, K., and J. Box (2001), Surface climatology of the Greenland ice sheet- Greenland Climate Network 1995-1999, *Journal of Geophysical Research.*, *106*(D24). 1.4.3

Straneo, F., and P. Heimbach (2013), North Atlantic warming and the retreat of Greenland's outlet glaciers., *Nature*, *504*(7478), 36–43, doi:10.1038/nature12854. 1.2.4, 1.4

Straneo, F., G. S. Hamilton, D. A. Sutherland, L. A. Stearns, F. Davidson, M. O. Hammill, G. B. Stenson, and A. Rosing-Asvid (2010), Rapid circulation of warm subtropical waters in a major glacial fjord in East Greenland, *Nature Geoscience*, *3*, 182–186, doi:10.1038/ngeo764. (document), 1.2.1, 5.3.1

Straneo, F., R. G. Curry, D. A. Sutherland, G. S. Hamilton, C. Cenedese, K. Vå ge, and L. a. Stearns (2011), Impact of fjord dynamics and glacial runoff on the circulation near Helheim Glacier, *Nature Geoscience*, *4*(5), 322–327, doi:10.1038/ngeo1109. 1.2.3

Straneo, F., D. A. Sutherland, D. Holland, C. Gladish, G. S. Hamilton, H. L. Johnson, E. Rignot, Y. Xu, and M. Koppes (2012), Characteristics of ocean waters reaching Greenland's glaciers, *Annals of Glaciology*, *53*(60), 202–210, doi:10.3189/2012AoG60A059. (document), 1.2.1

Tedesco, M., X. Fettweis, M. R. van den Broeke, R. S. W. van de Wal, C. J. P. P. Smeets, W. J. van de Berg, M. C. Serreze, and J. E. Box (2011), The role of

albedo and accumulation in the 2010 melting record in Greenland, *Environmental Research Letters*, *6*, 014,005, doi:10.1088/1748-9326/6/1/014005. 1.2.3, 1.2.4

Tedesco, M., X. Fettweis, T. Mote, J. Wahr, P. Alexander, J. E. Box, and B. Wouters (2013), Evidence and analysis of 2012 Greenland records from spaceborne observations, a regional climate model and reanalysis data, *The Cryosphere*, *7*, 615–630, doi:10.5194/tc-7-615-2013. 1.2.4

van den Broeke, M., J. Bamber, J. Ettema, E. Rignot, E. Schrama, W. J. van de Berg, E. van Meijgaard, I. Velicogna, and B. Wouters (2009), Partitioning recent Greenland mass loss., *Science*, *326*, 984–986, doi:10.1126/science.1178176. 1.2.4

Vaughan, D. G., H. F. J. Corr, R. A. Bindschadler, P. Dutrieux, G. H. Gudmundsson, A. Jenkins, T. Newman, P. Vornberger, and D. J. Wingham (2012), Subglacial melt channels and fracture in the floating part of Pine Island Glacier, Antarctica, *Journal of Geophysical Research*, *117*, doi:10.1029/2012JF002360. (document), 1.3.2, 4.3, 7

Vaughan, D. G., J. Comiso, I. Allison, J. Carrasco, G. Kaser, R. Kwok, P. Mote, T. Murray, F. Paul, J. Ren, E. Rignot, K. Solomina, K. Steffen, and T. Zhang (2013), Observations: Cryosphere. IN: Climate Change 2013: The Physical Science Basis. Contribution of Working Group 1 to the Fifth Assessment Report of the Intergovernmental Panel on Climate Change [Stocker, T.F., D. Qin, G.-K. Plattner, M. Tignor, S.K. Allen, J.Boschung, A. Nauels, Y. Xia, V. Bex and P.M. Midgley (eds.)], *Cambridge University Press, Cambridge, United Kingdom and New York, NY, USA*. 1.1, 1.2.4, 1.3

Weidick, A., N. Mikkelsen, C. Mayer, and S. Podlech (2004), Jakobshavn Isbræ, West Greenland : the 2002 2003 collapse and nomination for the UNESCO World Heritage List, *Geological Survey of Denmark and Greenland Bulletin*, *4*(2003), 85–88. 1.2.1, 1.2.4, 5.3.1, 5.3.3, 5.5, 7

Xu, Y., E. Rignot, D. Menemenlis, and M. Koppes (2012), Numerical experiments on subaqueous melting of Greenland tidewater glaciers in response to ocean warming and enhanced subglacial discharge, *Annals of Glaciology*, *53*(60), 229–234, doi:10.3189/2012AoG60A139. (document), 1.2.4, 3.3.3, 5.3.1, 5.4.1

Zwally, H. J., W. Abdalati, T. Herring, K. Larson, J. Saba, and K. Steffen (2002), Surface melt-induced acceleration of Greenland ice-sheet flow., *Science (New York, N.Y.)*, *297*(5579), 218–22, doi:10.1126/science.1072708. 1.2.3